DEVELOPMENT AND EXPERIMENTAL INVESTIGATIONS INTO MULTI-JET ROTARY NANOFINISHING PROCESS

Thesis

Submitted for the partial fulfillment of the Degree

of

Doctor of Philosophy

By

Shubham Choudhary
(Registration No.: 951808003)

Under the guidance of

Dr. Ravinder Kumar Duvedi
Associate Professor
Mechanical Engineering Department,
Thapar Institute of Engineering & Technology (Deemed to be University),
Patiala

Dr. Jaswinder Singh Saini
Associate Professor
Mechanical Engineering Department,
Thapar Institute of Engineering & Technology (Deemed to be University),
Patiala

THAPAR INSTITUTE
OF ENGINEERING & TECHNOLOGY
(Deemed to be University)

Patiala-147004, Punjab (India)
www.thapar.edu

September 2023

Dedicated

to

my

Father and Mother

"Mr. Subhash Singh Malik & Mrs. Brijesh Devi"

Certificate

I, Shubham Choudhary hereby certify that the work presented in this thesis report entitled "**DEVELOPMENT AND EXPERIMENTAL INVESTIGATIONS INTO MULTI-JET ROTARY NANOFINISHING PROCESS**" in fulfilment of requirement for the award of degree of **Doctor of Philosophy** submitted in Mechanical Engineering Department, Thapar Institute of Engineering & Technology (Deemed to be University), Patiala, is an authentic record of my own work carried out under the supervision of **Dr. Ravinder Kumar Duvedi** (Associate Professor, Mechanical Engineering Department, Thapar Institute of Engineering & Technology, Patiala) and **Dr. Jaswinder Singh Saini** (Associate Professor, Mechanical Engineering Department, Thapar Institute of Engineering & Technology, Patiala) from July 2018 to June 2023. The matter presented in this thesis has not been submitted either in part or full to any University or Institute for the award of any other degree.

Shubham Choudhary

Registration No.: 951808003 Date: June 30, 2023

It is certified that the above statement made by the student is correct to the best of our knowledge and belief.

Dr. Ravinder Kumar Duvedi
Associate Professor
Mechanical Engineering Department,
Thapar Institute of Engineering &
Technology (Deemed to be University),
Patiala-147004, Punjab
India

Dr. Jaswinder Singh Saini
Associate Professor
Mechanical Engineering Department,
Thapar Institute of Engineering &
Technology (Deemed to be University),
Patiala-147004, Punjab
India

Acknowledgments

I would like to thank most sincerely my supervisors, Dr. Ravinder Kumar Duvedi, Associate Professor, Mechanical Engineering Department and Dr. Jaswinder Singh Saini, Associate Professor, Mechanical Engineering Department, Thapar Institute of Engineering & Technology (Deemed to be University), for providing me such a valuable research opportunity and for their countless guidance, knowledge, and motivation during the course of my research. I learned a lot from them over the course of this Ph.D. work. Their goal-oriented style of work, passion towards research, work ethics, has been very inspiring for me. Their daily practice of following up on recent scientific literature is something that I also tried to adopt and greatly benefitted. I really appreciate their unconditional support and encouragement towards doing high-caliber research. It has been a great honor to work under their guidance.

I am extremely thankful to Prof. Padmakumar Nair, Director, Thapar Institute of Engineering & Technology (Deemed to be University), Prof. N. Tejo Prakash, Dean of Research & Sponsored Projects, Thapar Institute of Engineering & Technology (Deemed to be University) and Dr. T. K. Bera, Head, Mechanical Engineering Department, Thapar Institute of Engineering & Technology (Deemed to be University) for extending the opportunity to undertake this doctoral research.

I would like to profoundly thank my doctoral committee members, Dr. Vivek Jain and Dr. Dr. Hiralal Bhowmick, Mechanical Engineering Department and Prof. Raj Kumar Gupta, Chemical Engineering Department, Thapar Institute of Engineering & Technology (Deemed to be University) for their immense help and guiding me towards the right direction. I am grateful to Professor and Head Dr. Kulvir Singh, School of Physics & Materials Science, Thapar Institute of Engineering & Technology (Deemed to be University) for his expert advice in various stages of my research work and also during publications of my research papers. My heartful thanks to the staff members of the Mechanical Engineering Department and Chemical Engineering Department, Thapar Institute of Engineering & Technology (Deemed to be University) for their valuable contribution, spiritual and moral support.

I am really thankful to Mr. Manoj Kumar, Mr. Rishavdeep Mehra and Narinder Kumar for valuable contribution and helping me to fabricate experimental test rig, CNC programming and mechanical testing.

My special thanks to Dr. Pallavi Pant, former research fellow, The University of Alabama, who motivated me for doing Ph.D. and assisting me in a very dedicated way offered undivided attention and valuable advice.

My endless thanks go to my research colleagues, Mr. Shitanshu Arya, Mr. Deepak Sharma, Dr. Kunal Arora, Dr. Atul Babar, Dr. Harmanpreet Singh, Dr. Mohit Kumar, Dr. Sikander Hans, Dr. Pankaj Kumar, Mr. Sandeep Nain, Dr. Dinesh Kumar and Dr. Umesh Vishwakarma, for their valuable contribution, spiritual and moral support at various stages of my work.

My deepest gratitude goes to my beloved parents, Mr. Subhash Singh Malik, Mrs. Brijesh Devi, my brother, Mr. Deepak Malik and my wife Mrs. Anchal Chaudhary who have always supported me on every stage of my life. My last word is reserved for my lucky daughter's Shivanshi Choudhary and Era Choudhary for their immense blessings, happiness, and positive soul.

Finally, I wish to thank the 'LORD SHIVA' God for his sufficiency.

Shubham Choudhary

Abstract

Metallic dies and moulds play a crucial role in manufacturing industries, particularly in industries that produce a large number of identical parts or products. Metallic dies and moulds in manufacturing industries are designed to produce high-precision parts and products that are consistent in quality and dimension. This is especially important in industries where even small deviations in dimensions or specifications can cause product failure or other issues. Increased efficiency using metallic dies and moulds in manufacturing can help to increase efficiency and productivity. The use of automated systems and machines that are designed to work with dies and moulds can speed up the production process and reduce the need for manual labor. The use of metallic dies and moulds can be cost-effective for manufacturing industries in the long run. While the initial investment in the tooling can be high, the cost per part or product can be significantly reduced as a result of the increased efficiency and precision. Most of the automated techniques used for surface polishing of open dies and moulds are still the slowest one with the polishing time in certain cases constitute the significant percentage of overall die manufacturing time. The advances in die polishing technologies have helped to minimize these problems to certain extent and have enabled achievement of better surface finishing. But these processes still have scope for improvements to make them more efficient in the present context of demand for higher manufacturing productivity and the stringent requirement of product quality.

Many researchers have proposed various non-conventional post processing techniques such as chemical polishing (CP) and electropolishing (EP), to improve the surface quality. Some have even used integrated techniques combining with electrical polishing (EP), mechanical polishing (MP) and ultrasonic methods, or use of abrasive jet polishing (AJP) and magnetorheological finishing process (MRF) to improve the surface quality. Compared with these non-conventional polishing processes, FJP process is better suited for polishing of dies and moulds, because of better material removal rate, ability to generate small tool influence function (TIF), no heat generation during polishing and better tool life. The fluid jet polishing (FJP) is an ultra-precision and non-contact type polishing process for generating high quality surface finish in metallics dies and moulds manufactured from ductile materials like Monel-400 and AISI H13 die steel. This work presents a study on FJP polishing of Monel-400 and AISI H13 die steel material using a custom designed 3D printed nozzle and Silicon Carbide (SiC) abrasive slurry. The study presents a simultaneous effect of pressure, stand-off distance, polishing time, feed rate and spindle rotation on the surface finish using

water based abrasive slurry mixed with water soluble cutting oil. The Central Composite Design (CCD) method was used to develop the experimental plan. ANOVA analysis was performed to develop a regression model and find the contribution of each parameter on the percentage change in surface roughness.

The study presents an effect of pressure, stand-off distance and polishing time on Monel-400 workpiece material. The validation of the developed regression equation was done by polishing the plate of Monel-400 using the optimized parameters: pressure of $9.6bar$, stand-off distance of $32.2mm$ and polishing time of $170sec$. The optimized FJP parameters successfully generated the surface roughness of $90nm$ in one of the experimental tests. The predicted results were in close agreement with the experimental results. Further improving the polishing efficiency, the optimal feed rate of $20mm/min$ was used to polish $40mm \times 50mm$ Monel-400 plate, the surface roughness was reduced from $300nm$ to $80nm$ in 10 multiple passes showing the reduction in peaks and valleys with surface improvement of 73.33 %. The result shows that the FJP process also tends to improve the life span of Monel-400 die steel workpieces. The study also presents an effect of pressure, stand-off distance and polishing time on AISI H13 die steel workpiece material. The regression model developed for the FJP process was validated by polishing the plate specimen of AISI H13 having $500nm$ average initial surface roughness with the optimized parameters; pressure of $11.1bar$, stand-off distance of $32mm$ and polishing time of $174.6sec$. The optimized FJP parameters were able to generate the surface roughness of $240nm$ in one of the confirmation tests. In addition, the optimal feed rate of $20mm/min$ was used to polish $30mm \times 30mm$ steel plate made of AISI H13, the surface roughness was reduced from $500nm$ to $130nm$ in $99.2min$ showing the reduction in peaks and valleys with surface improvement of 74% which results in enhanced polishing efficiency.

Further, the work was extended to presents a simultaneous effect of feed rate and spindle rotation on AISI H13 workpiece material. The regression model developed for the FJP process was validated by polishing the AISI H13 workpiece with $390nm$ average initial surface roughness with the optimized process parameters; feed rate of $20mm/min$ and spindle rotation of $60rpm$. The optimized FJP parameters were able to generate the surface roughness of $240nm$. To further enhance the polishing efficiency, the optimum process parameters were used to polish AISI H13 die steel workpiece, the surface roughness was reduced from $390nm$ to $110nm$ in $15min$ with 12 number of passes which shows the reduction in peaks and valleys with surface improvement of 71.79%.

Table of Contents

List of Figures

List of Tables

List of Symbols

P	Pressure
D	Stand-off distance
T	Polishing time
F	Feed rates
R	Spindle rotation
$\% \Delta R_a$	Percentage change in surface roughness
R_a	Surface roughness
α	Impact angle/ Inclination angle
wt.%	Weight percentage
L	Travel path
sec	Seconds
Min	Minutes

List of Abbreviations

FJP	Fluid jet polishing
SJP	Single jet polishing
MJP	Multi-jet polishing
MRF	Magneto-rheological finishing
CIP's	Carbon-iron particles
CVD	Chemical vapour desposited
CMP	Chemical mechanical polishing
FAP	Fixed abrasive pad
AE	Acoustic emission
RSM	Response surface methodology
CCD	Central composite design
BBD	Box-behnken design
DOE	Design of experiment
ANOVA	Analysis of variance
TIF	Tool influence function
SLM	Selective laser melting
CFD	Computational fluid dynamics
SST	Shear-stress transport
DPM	Discete phase modelling
SiC	Silicon carbide
PRV	Pressure regulating valve
PS	Pressor sensor
PG	Pressure gauge

Chapter 1
Introduction

The quality of die and moulds surfaces plays an important role in the product quality as well as the productivity of the manufacturing industries. The quality, cost and manufacturing lead times of dies and moulds directly affect the manufacturing productivity and hence the economics of manufacturing sector. The productivity in dies and moulds manufacturing depends on factors such as ability to machine them to the specified dimensional accuracy and the required surface finish. It is desirable to design and manufacture die and moulds parts such that they are free from surface defects, cracks and have better service life.

The dies used in manufacturing have complex geometries and curved sculptured shapes as can be seen in the components like optical lenses, security cameras, vehicle head lights etc. The dies used to produce such components need to have surface roughness in the range of microns and nanometer scale. Thus, surface polishing is one of the critical processes in die manufacturing which consumes around 30% to 50% more time as compared to the machining processes [1]. Manual polishing of dies and moulds is an inaccurate, noisy and a hazardous operation. At the same time, the modern die materials are quite hard and it is desirable to use the automated polishing procedures for die manufacturing. Automation of polishing processes can reduce the lead times for dies and moulds manufacturing and enable the manufacturer to achieve the better surface quality with enhanced production efficiency.

Most of the automated techniques used for surface polishing of open dies and moulds are still the slowest one and the polishing time in certain cases constitute the significant percentage of overall die manufacturing time. The advances in die polishing technologies have helped to minimize such problems to certain extent and have enabled achievement of better surface finishing, but these processes still have scope for improvements to make them more efficient in the present context of demand for higher manufacturing productivity and the stringent requirement of product quality. The surface polishing/finishing processes are also called nano-polishing processes or ultra-finishing processes owing to their ability to generate the surface finish in the range of sub-microns or nano-meter level. The classification of nano-finishing processes is shown in Figure 1.1. The unique characteristics of some of the prominently used nano-finishing techniques are explained in the next section.

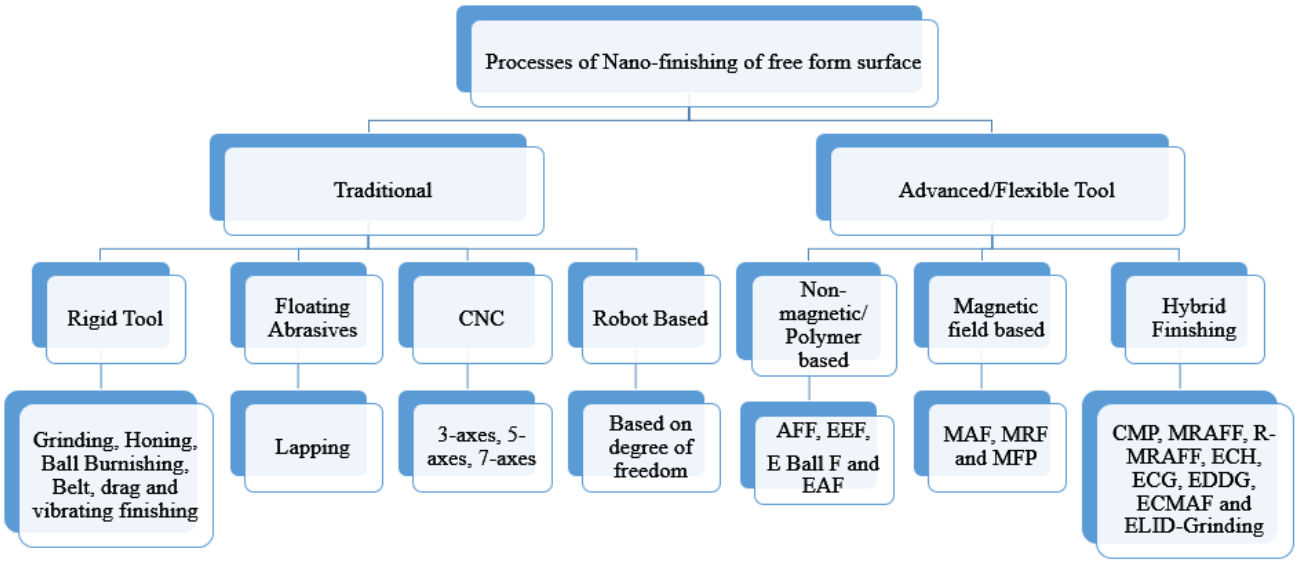

Figure 1.1: Classification of nano-finishing process for free form surfaces [2].

1.2 Nano-finishing methods

The most common nano-finishing methods employed in the industry for surface polishing are as listed below:

(i) Fluid Jet polishing

(ii) Ultrasonic cavitation assisted fluid jet polishing

(iii) Magnetorheological finishings

1.2.1 Fluid jet polishing

The concept of fluid jet polishing (FJP) was given by Fahnle et al. [3] for polishing optical lens. FJP is a versatile polishing process in which the pre-mixture of abrasive particles and water is pumped to low a pressure in the range of $0.2MPa$ to $2MPa$ and passed through a narrow orifice or a converging nozzle before it impinges on the workpiece surface [4]. FJP is an unconventional polishing process which is being widely used to develop uniform surface integrity with high precision accuracy. Various industries like automotive, die manufacturing, aerospace, marine etc. requires high quality surface finish and FJP is capable for polishing complex shapes/contours without generating heat zones. It is also capable of polishing hard and difficult to cut, ductile and brittle materials. In comparison to other polishing processes, it has various advantages such as no heat generation during polishing, no tool wear, unique adaptive behavior for polishing various free form surfaces and stability in material removal rate [5]. The schematic diagram of FJP process is shown in Figure 1.2.

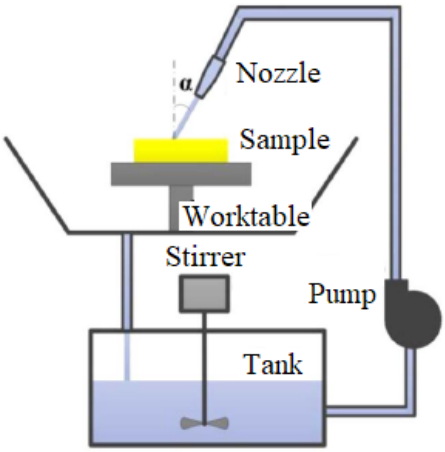

Figure 1.2: Schematic diagram of fluid jet polishing (FJP) [5].

1.2.2 Ultrasonic cavitation assisted fluid jet polishing

The working principle of ultrasonic assisted FJP technique is shown in Figure 1.3. The slurry enters the side attachment of nozzle cavity where premixed homogenous slurry passes through laser drilled sapphire insert at the outlet, thereafter it directly strikes to the target surface [6]. At the top of the attachment, an ultrasonic transducer is fixed to support plate which generates vibrations and produces acoustic waves (microbubbles) at the nozzle outlet. These microbubbles are responsible for the enhanced material removal from the work piece compared to FJP process.

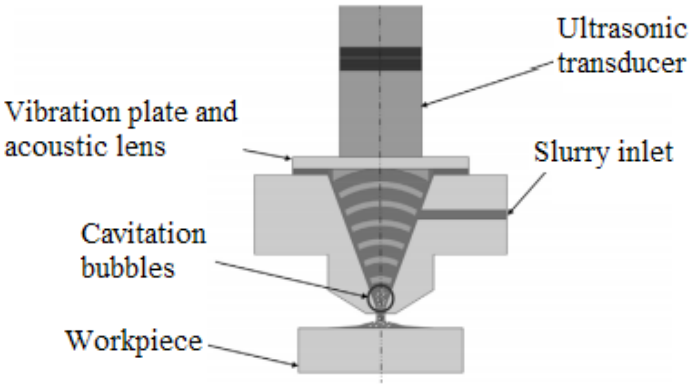

Figure 1.3: Ultrasonic cavitation assisted fluid jet polishing process [6].

1.2.3 Magnetorheological finishing

This process uses magnetorheological fluid (MRF) which is also commonly known as smart fluid. This process is guided by external magnetic field [7]. The MRF fluid contains ferromagnetic particles called carbon-iron particles (CIPs), non-magnetic abrasive particles, carrier medium and some additives. Once the dipolar interaction between carbon-iron particles (CIPs) exceeds their thermal energy, the particles aggregate into chains of dipoles aligned in the field direction. The principal of magnetorheological finishing is shown in Figure 1.4.

In the MRF process, the fluid strength (static yield shear stress) increases non-linearly with the increase in the applied magnetic field because the particles are ferromagnetic in nature and magnetization in different parts of the particles occur non-uniformly. This finishing process is capable of generating the surface finish of the order of $10nm$ to $100nm$. The MRF process is used for finishing optical glasses, glass ceramics, plastics and some non-magnetic metals.

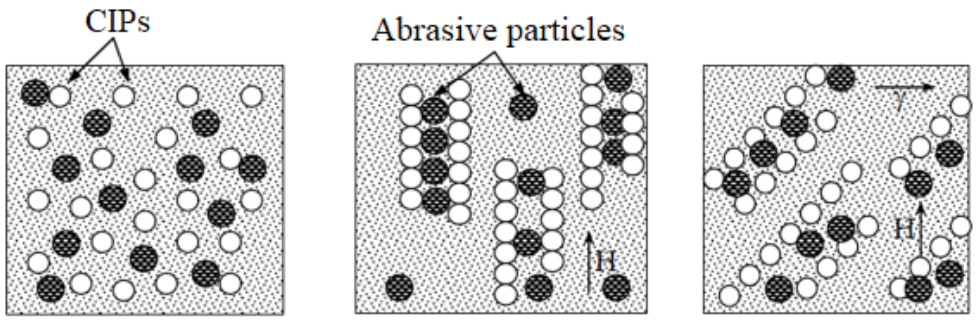

Figure 1.4: Principal of magnetorheological finishing. Dispersion of MR fluid when (a) no magnetic field is applied (b) with field strength applied (in the direction shown by H) (c) with the application of both shear strain and magnetic field [7].

1.3 Processes used for polishing metallic dies and molds

The most common methods employed in the industry for surface polishing are as listed below:

(i) Manual Polishing
(ii) Buffing
(iii) Electro-Polishing
(iv) Vibratory Polishing
(v) Laser Polishing

The process of polishing metallic dies and molds involves removing any imperfections or surface irregularities to achieve a smooth, mirror surface finish. Some common methods for polishing metallic dies and molds are as follows:

Manual Polishing: This is a traditional method of polishing in which a skilled operator uses various hand tools such as sandpaper, files, and polishing pads to remove any roughness and achieve a smooth surface finish. It is suitable for small molds or dies and requires skill and patience.

Buffing: Buffing involves the use of a buffing machine that spins a buffing wheel, which is coated with an abrasive polishing compound. The mold or die is then held against the buffing wheel to remove any imperfections and achieve a smooth surface finish.

Electro-Polishing: This method uses an electrical current and a chemical solution to remove any surface roughness. The mold or die is immersed in an electrolyte solution, and an electrical current is passed through it. This process removes any high spots or roughness and creates a smooth, shiny surface finish.

Vibratory Polishing: This process uses a vibratory tumbler filled with a polishing media, which vibrates at high speed to remove any surface roughness. The mold or die is then placed in the tumbler, and the media vibrates against the surface, removing any unwanted peaks and valleys.

Laser Polishing: Laser polishing is a relatively new method that uses a laser to melt the surface of the mold or die. This method is suitable for complex shapes and can achieve a high level of precision.

Regardless of the method used, it's important to clean the mold or die thoroughly before polishing to remove any dirt, grime, or other contaminants. This ensures that the polishing process is effective and achieves the desired surface finish. The following polishing methods and their industrial applications are shown in Table 1.1.

Table 1.1: Polishing methods and their industrial applications.

S. No.	Polishing methods	Ra (nm)	Industrial applications
1	Laser polishing	100 to 500	automotive and aerospace industries
2	Electrolytic polishing	50 to 100	medical industry, surgical instruments and implants.
3	Chemical mechanical polishing (CMP)	10 to 50	semiconductor industry (production of integrated circuits)
4	Diamond polishing	less than 10	optical components, such as lenses and mirrors

1.4 Comparison of the surface polishing methods

As discussed in the previous section, the fluid jet polishing (FJP) process is the primary surface finishing process [3], which has been enhanced for its ability for material removal by

the use of ultrasonic cavitation assisted fluid jet polishing [6]. The third main process, namely, magnetorheological finishing makes use of magnetic field to enhance the material removal rate, but it does not use the high-pressure fluid as used in the other two discussed processes. Though, FJP is limited by its low material removal rate and its limitation of using excessive polishing time for medium to large sized die surfaces. To reduce the polishing time in FJP process the researchers have tried several inventive methods like the use of multi-jet nozzles, higher pressure of the fluid medium, use of different slurry concentrations, change in impact inclination of pressurized fluid jet and different stand-off distances of non-contact nozzle from the workpiece surface. Additionally, it has been found that the stagnation effect or central uncut material on the substrate surface can be minimized by using the rotary fluid jet. This has been found to be advantageous as it improves the process efficiency of FJP process.

1.5 Material Removal Mechanism in FJP Process

In FJP process, the abrasive particles are accelerated by the drag force of carrier medium (water and/or lubricating oil) to impact on the workpiece surface which leads to material removal. The mechanism of material removal and the quality of the surface finish obtained in FJP is primarily dependent on the particle impingement energy and the resultant particle velocity at the point of strike on the substrate surface. The kinetic energy of the striking abrasive particles depends mainly on the jet pressure, average abrasive particle size and the stand-off distance [4].

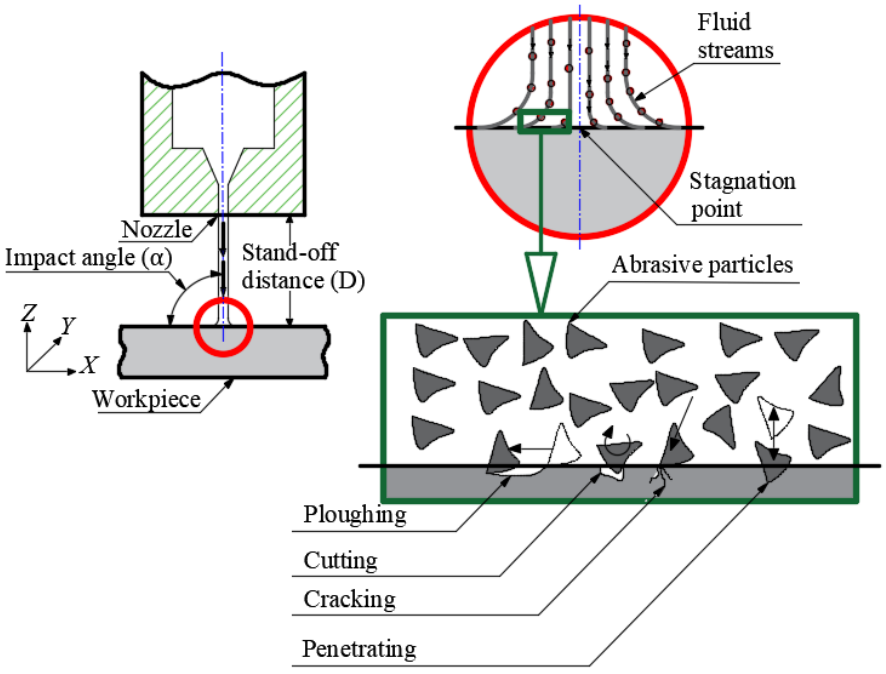

Figure 1.5: Material removal mechanism of FJP process.

The slurry particles impinging the surface of a ductile material at an impact angle (α) may lead to the different types of material removal mechanisms. The material removal from the substrate surface can be caused by the penetration of the slurry particles, cracking of substrate surface caused by the kinetic energy of slurry particles, and/or the cutting and ploughing action of the slurry particles moving over the substrate surface. The Figure 1.5 shows the aforesaid three material removal mechanisms in FJP process.

The velocity of fluid jet in FJP process is considered to be equally distributed inside the nozzle but there is a considerable velocity difference as the fluid jet leaves the nozzle. This is attributed to the boundary layer formed by the environmental drag. The entire region of the fluid jet flowing out of the nozzle can be divided into three regions/domain as shown in Figure 1.6 [8]:

Potential Core Region: The flow within this region are in irrotational motion where velocity components are highly stream-lined and the slurry particle flowing in this region carries sufficient amount of kinetic energy for accomplishing the cutting action or material removal from the workpiece surface.

Main Region: Within this segment, the jet axial velocity and dynamic pressure reduce gradually, and turbulence characteristics are highly dominating.

Diffused Droplet Region: In this region slurry jet and environment medium (air) are thoroughly mixed together because of which the outer region of the fluid jet loses its cohesive strength/bond. This leads to the formation of water droplets inside the slurry domain.

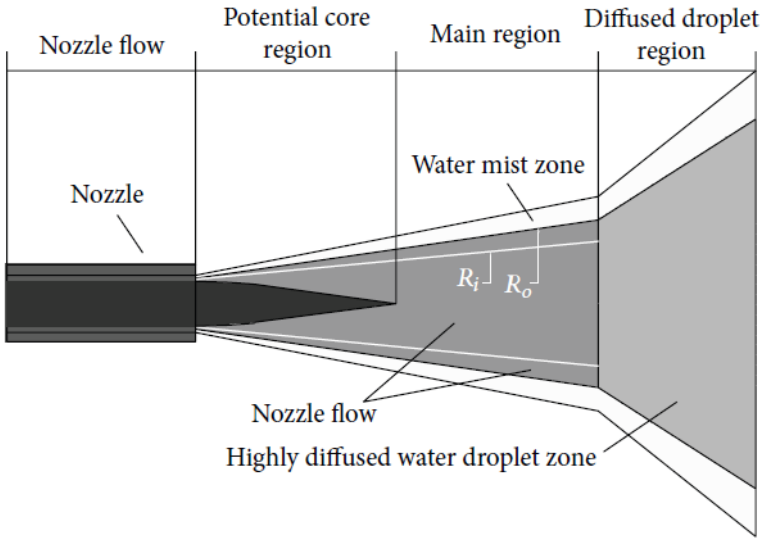

Figure 1.6 Fluid jet distribution of FJP process [8].

As shown in Figure 1.6, the slurry particles contained in the potential core region have highest energy and this core region is applied for cutting action. The diffused droplet region is applied for dust-laying applications and aspirating. The jet in the main region zone is applied mainly for the surface cleaning and surface finish operations. The smaller abrasive particles are preferred particularly in the FJP process to achieve nano-scale surface finish. The low pressure range of the fluid jet in FJP process causes the fluid jet to have low kinetic energy. This enables the smaller average sized abrasive particles in the slurry to cause only the ploughing and cutting type of material removal in FJP process [4].

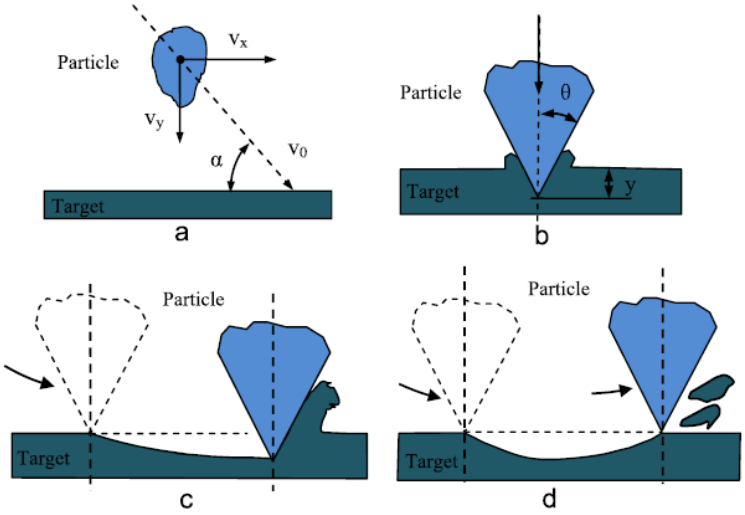

Figure 1.7: (a) The horizontal velocity component V_x and the vertical velocity component V_y of an abrasive particle in the slurry jet in FJP Process, (b) deformation wear caused by a vertically impinging abrasive particle, (c) cutting action caused when the horizontal velocity V_x component is not sufficient to shear a targeted volume, and (d) cutting action of the abrasive particle when the V_x component of velocity is sufficient to shear a targeted volume [9].

The Figure 1.7 shows the horizontal velocity component V_x and the vertical velocity component V_y of an abrasive particle moving in the slurry jet in a typical FJP Process. The vertical velocity component V_y is responsible for the vertical penetration of the abrasive particles on the substrate surface, while the shearing/ chipping out of the material from the substrate surface is caused by virtue of the kinetic energy of the abrasive particle due to the horizontal velocity component V_x. The transition of the horizontal velocity component V_x is almost from zero to the maximum from the core of the striking fluid jet (at the stagnation point as shown in Figure 1.6) to the outermost part of the striking jet (see the highlighted fluid streams in the outer zone of the striking jet in Figure 1.6). By adopting certain mechanism to alter the horizontal velocity component V_x for a given vertical velocity component V_y, one can alter the profile of the tool influence function as well as the rate of material removal in FJP polishing.

1.6 Background

To maximize the surface finish obtained in FJP process, a better understanding about the interaction of jet pressure, stand-off distance and polishing time is required. In a FJP study on polishing of die steel, Wang et al. [10] studied the effect of varying the stand-off distance from $2.0mm$ to $35.0mm$ for a constant jet pressure of $8.0bar$. It was observed that the stand-off distance plays an important role and influences the vertical as well as horizontal components of the particle velocity in the shear zone which in turn affects the shape of the tool influence function (TIF) zone.

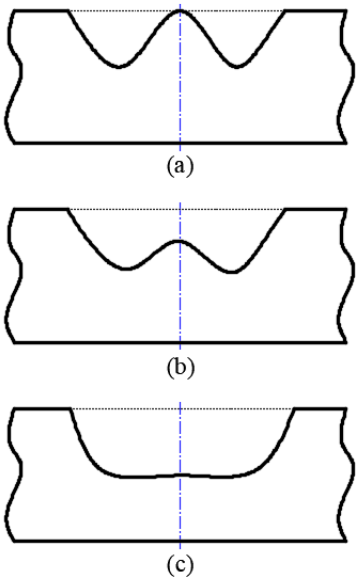

Figure 1.8: A typical tool influence function (TIF) cross-section profile for FJP process, (a) W-shaped TIF cross-section formation at low stand-off distance, (b) the central valley of W-shaped TIF cross-section supressed at intermediate value of stand-off distance and (c) U-shaped TIF cross-section profile formation at higher range of stand-off distance.

The smaller stand-off distance at higher pressure ranges tends to generate a 'W-shaped' sectional profile as shown in Figure 1.8(a). This is because of the reason that a negligible material removal takes place at the central zone owing to that fact that the abrasive particles possess high fluid pressure and almost zero velocity at the stagnation point on the substrate surface. The location of the stagnation point is shown in central region of the fluid jet and workpiece interface in Figure 1.5 and Figure 1.8(a). For an intermediate range of stand-off distance, the height of the central peak of 'W-shaped' sectional profile supresses as shown in Figure 1.8 (b). With further increase in stand-off distance, the shape of the sectional profile transform to 'U-shape', as shown in Figure 1.8 (c). The 'U-shaped' section have a relatively

better surface finish in its central region as compared to the 'W' section because the velocity of abrasive particle relatively decreases with increasing stand-off distance.

Additionally, the concept of sliding-grinding mechanism presented by Tsai et al. [11] shows that the compound mixture of water and water-based machining oil in FJP process assists in achieving better surface finish compared to when only water is used as the abrasive carrying media. Moreover, the higher value of stand-off distance in FJP process, if used along with the slurry jet that contains water soluble machining oil can result in stable and symmetrical TIF profile on the polished surface.

1.7 Uniqueness of the research work

- Developed customized Fluid jet polishing (FJP) test rig using coolant inducer assembly with customized metal 3D printed single and multi-nozzle polishing tool having $1mm$ nozzle diameter.
- Studied the combined interaction of the FJP parameters: pressure, standoff distance, polishing time, feed rates and spindle rotation at higher stand-off distances ($24mm$ to $36mm$) for polishing of NiCu alloy (Monel-400) and AISI H13 die steel.
- Design of experiments studies in this work are conducted using the Response Surface Methodology (RSM) to determine the optimized FJP process parameter values at stabilized pressure of the fluid jet with maximum pressure variation of $\pm 0.1bar$.
- The optimized FJP parameters was used for multi-pass polishing of the plane workpiece samples of NiCu alloy (Monel-400) and AISI H13 die steel using *non-rotary* and *rotary* nozzle jet to determine the relative performance of the two methods.

In this context, in the present work we focused on the improvement of the process efficiencies for surface polishing of the dies manufactured from NiCu alloy (Monel-400) and AISI H13 die steel using fluid jet polishing process. The applications of such a technology relative to the non-rotary FJP process used for polishing of Monel-400 and AISI H13 die steel are explained in different chapters to demonstrate that the results obtained for polishing Monel-400 and AISI H13 steel has improved in terms of quality when particularly starting from a grinded surface as well as that FJP method allows for a better TIF width which enhances the FJP polishing efficiency by 73.33% in Monel-400, 74% in case of AISI H13 with non-rotary and 71.79% with rotary nozzle jet as discussed in details in the Chapter 4, 5 and 6.

Chapter 2
Literature Review

The dies and moulds have a significant importance in the production systems globally. All medium volume to mass produced parts are mostly formed/moulded using manufacturing processes that extensively use dies and moulds. The surface quality of dies and moulds plays an important role in the product quality as well as the productivity of the manufacturing industries. The quality, cost and manufacturing lead time of dies and moulds directly affect the manufacturing productivity and hence the economics of manufacturing sector. The productivity in dies and moulds manufacturing depends on factors such as ability to machine them to the specified dimensional accuracy and the required surface finish.

It is observed from the literature reviewed that there are several important aspects on which the manufacturing of die and mould depend. Some of the prime aspects in die manufacturing include material used, roughing, finishing and precision machining operations used and the ultra-precision finishing operations which are governed by the tolerances required on the finished dies and moulds. This chapter presents the various aspects of manufacturing of die and mould with a focus on the technologies developed in the area of surface finishing operations and the process parameters used for achieving the operational efficiencies of the surface finishing operations as available from the existing literature.

2.1 Die and workpiece materials

The precision dies are used to fabricate components having good mechanical properties like toughness, hardness, and sufficient resistance to withstand high temperature fatigue cycles, corrosion and abrasion. Monel 400 and AISI H13 die steel material are preferred material for precision dies [5,12] and are used extensively in the manufacturing of optical lenses used in remote sensing, broadcasting, medical & defence and automotive, die manufacturing, aerospace, marine products. The surface finishing operation on the dies and mould used for precision engineering applications are quite time consuming and to achieve best returns on the invested cost one need to have a considerable understanding of the die materials as well as the process for which the dies are to be further used.

Ahn *et al*. [1] developed a sensor integrated approach for analysing the on-site polishing status for automobile headlight lamp die machined from SKD11 material using abrasive flow finishing process. The reported method reduced the roughness of the pre-machined die surface to $0.025\mu m$.

Zhu *et al*. [13] investigated abrasive water jet method for enhancing the micro material removal rate for polishing of silicate glass, Al_2O_3, and Si_3N_4 with B_4C abrasive particles using the waterjet pressure of $15MPa$ and the flow rate of $120mg/min$.

Beaucamp *et al*. [14] developed a method using a 7-axis CNC setup equipped with fluid jet and bonnet polishing tools for surface finishing of electroless nickel (ENi) and tungsten carbide (WC) dies. Using the developed method, a surface roughness of around $1.0nm$ was achieved with the form correction value of less than $31nm$ (peak to valley). In their further work, Beaucamp and Namba [15] worked on the super-finishing process for making dies from electroless nickel plated and diamond turned Sapphire insert material which are used for manufacturing x-ray telescope optical lens. The electroless nickel plating generates nearly $100nm$ peak-valley roughness and to reduce it, a novel super-finishing method was evolved which was a combination of fluid jet polishing and bonnet polishing. A two staged process was used for polishing of a circular sample plate of $50mm$ diameter of the said material with abrasive particle of $0.2\mu m$ grain size and the surface roughness value of $0.3nm$ rms was achieved.

Yunata *et al*. [16] developed a plasma polishing technique for chemical vapour deposited (CVD)-diamond coated tungsten carbide (WC) dies used for different material like stainless sheets, aluminium sheets and cold rolled sheets. The plasma gas was used for polishing process to achieve minimum surface roughness up to $0.3\mu m$. The results found that the uniformity of surface profile and faster finishing rate was achieved in CVD diamond surface. Choi and Jeong [17] used hydrophilic fixed adhesive pad (FAP) to achieve nanometer surface roughness of $15.1nm$ in D2 die steel and compared the result using thermo-curable FAP polishing. It is reported that the results of hydrophilic FAP polishing was better due to self-conditioning mechanism and were free from swelling and glazing phenomenon.

2.2 Nano finishing polishing processes

This section discusses the literature related to the nano finishing processes used in dies and moulds.

According to Beaucamp [4], the particle size affect the rate of material removal in FJP process. The material removal rate in FJP process increases exponentially as a function of inlet pressure and abrasive particle size, whereas the surface roughness increases linearly with these two parameters. The recommended smallest abrasive particle size in FJP is limited to average diameter of $0.1\mu m$, because the abrasive particles below this range do not possess sufficient kinetic energy to shear the substrate surface. As the particle size increases, the more material removal will take place because at higher slurry jet pressure the particles get more energized and strike the workpiece surface with higher kinetic energy which results into more material removal from the substrate surface.

FJP process can achieve nanometer level surface roughness in small and complex optical geometries with negligible tool wear. Beaucamp *et al*. [6] further developed a technique to enhance material removal rate up to 380% using microbubbles generated using a mechanical transducer. The workpiece material used during experimentation were BK7 glass and electroless nickel whereas, Al_2O_3 of $0.6\mu m$ and $0.8\mu m$ grit sizes were used as abrasive.

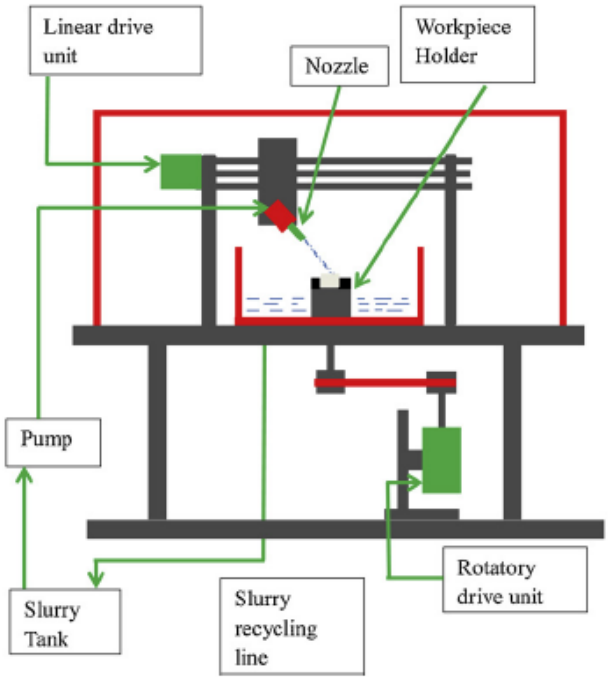

Figure 2.1: Layout diagram of abrasive slurry process [18].

Anbarasu et al. [18] developed a multi-staged low pressure abrasive slurry jet polishing technique for Aluminium Oxide (Al_2O_3) and Cerium Oxide (CeO_2) abrasive particles. To study the effect of multistage polishing process for achieving smooth surface roughness, experiments were performed with the help of abrasive slurry experimental test rig as shown in Figure 2.1. The experimental set up consist of pump with dampener (to minimize fluctuation in the flow field), linear drives (axis motion), one rotatory drive unit for workpiece rotation and stainless-steel nozzle of $2mm$ diameter. For polishing workpiece surface, the abrasive slurry was injected though nozzle outlet and impinges into the substrate surface of the workpiece. To polish entire workpiece surface, nozzle travel with low feed rate and constant workpiece rotation. Thereafter, the slurry was collected back to the container and was reused continuously. The authors observed that the Al_2O_3 abrasive of $0.5\mu m$ average particle size offered better surface finish when compared to the Cerium Oxide (CeO_2) abrasive particles of the same size in finishing pass.

Cheung *et al*. [19] designed multi-jet nozzle tool with a pressure control system to study the polishing of the curvature adaptive surfaces as shown in Figure 2.2. The system used an array of pressure control valves controlled by pressure-based sensors and controlling units. Each of the nozzle-jets operate individually to maintain the stable material removal on to the workpiece surface. The authors studied the effect of jet distance between workpiece and nozzle using CFD simulations. Two nozzles of $0.5mm$ diameter were used and four different jet distance were designed according to the simulation outcomes. Their results showed that the curvature adaptive multi-jet polishing was effective for improving polishing of complex geometries.

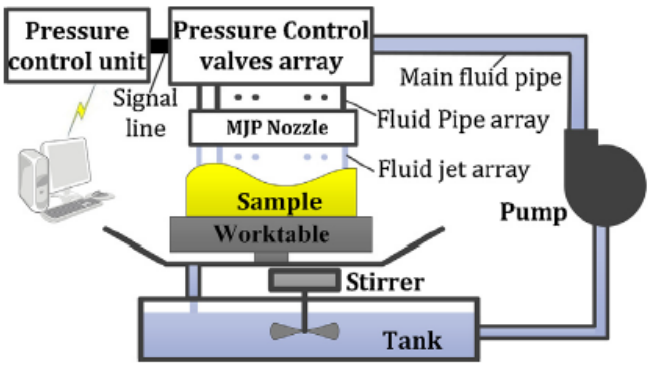

Figure 2.2: Schematic diagram of Curvature adaptive FJP process [19].

Wang et al. [5] developed a novel multi-jet polishing (MJP) tool to polish the large sized components with highly efficient metal removal rate. The schematic diagram of the MJP

experimental set up is shown in Figure 2.3. The FJP process can be extended in both single jet polishing process (SJP) and multi-jet polishing process (MJP) by varying types of nozzles. The MJP tool is integrated with fixture of number of single-orifice nozzles. Three kinds of polishing tools were used for increasing polishing efficiency, which were line distributed 5-jet tool, circular distributed 5-jet tool and square array distributed 9-jet tool respectively. The MJP tool was fabricated by stainless steel material with $1mm$ nozzle diameter. The authors reported that the circular distributed 5-jet polishing tool had more material removal rate and better quality of polished surface compared to two other tool designs for polishing large scale lens array surfaces.

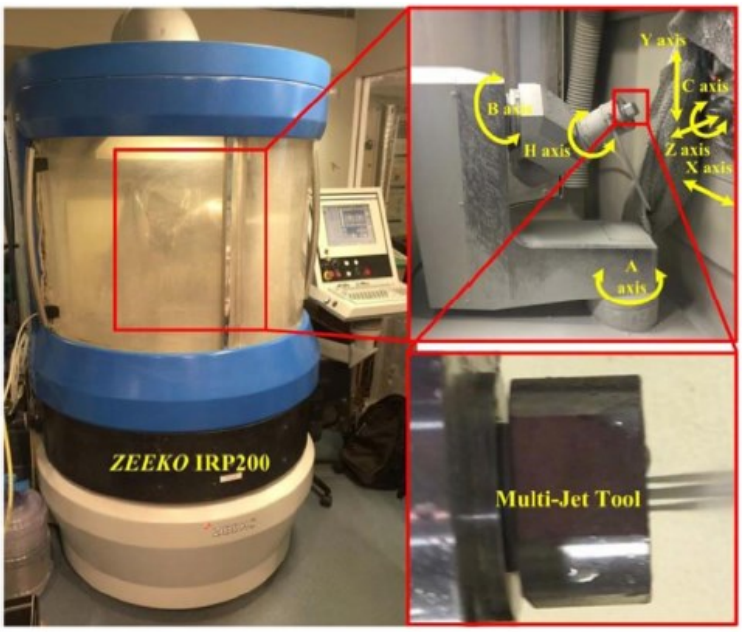

Figure 2.3: Experimetal test rig of FJP process [5].

Shiou et al. [20] used a custom designed rotary multi-jet polishing tool to study the effect of jet impinging angle and the number of jets to achieve better process efficiency and surface finish for polishing the Zerodur optical glass. The innovatory rotational multi-jet polishing tool was integrated with a machining center. The tool attachments consisted of shank coupled with rotating shaft, two thrust bearing which were used to normalize the pressure induced by the fluid jet.

2.2.1 Other nano finishing processes

The increased demand of high precision lenses in the advanced cameras used in biomedical field, broadcasting, security system, and remote sensing applications need very high quality

surface finish. For achieving such a higher quality surface finish, Satake *et al*. [21] proposed a new vibration assisted polishing technique which used polishing pads containing TiO_2 particles. The technique was tested on synthetic quartz glass sample of $100mm$ diameter with a polishing pressure of about $195kPa$ and Cerium Oxide of grain size $1.0\mu m$ as the slurry. The surface finish of $0.3\mu m$ was obtained with an improved material removal rate.

Nagdeve *et al*. [22] reported the state of art on nanofinishing of freeform surfaces. It was reported that the traditional finishing processes like honing, ball burnishing, lapping, grinding, vibrating finishing and CNC controlled techniques were helpful for removing materials from irregular surfaces but were unsuccessful to achieve nanometer level surface finish. Whereas, the non-traditional finishing technique using combined effect of abrasive particles and magnetic field could achieve nanometer surface roughness.

Mohammad *et al.* [23] discussed the hybrid electrochemical mechanical polishing technique (ECMP). In this technique, the milled surface was polished through mechanical action (bonded abrasive or ECG) followed by electrochemical action. Electrochemical process removed about 90% of material while mechanical abrasion removed higher peak to valley irregularities. The main advantage of this process was the increased tool life which was reported to be enhanced by 10 times compared to conventional ECMP process.

Kim and Noh [24] developed magnetic polishing tool for achieving surface finish of the magnitude of $0.09\mu m$ of curved surface die. The polishing was conducted in two stages. In first stage, abrasive wheel was used to remove rough surface irregularities followed by fine polishing using magnetic brush to get mirror-like surface finish. Polishing pressure was also examined by varying distance between the workpiece and polishing tool.

Submerged multi-fluid jet polishing process is a unique technique, reported by Beaucamp [4] in which polishing tool or nozzle is kept below the waterline of the tank and workpiece was immersed within a tank of circulating slurry as shown in Figure 2.4. The surface generation or experimental data shows that the material removal footprints had Gaussian like appearance instead of W-shaped in common FJP process. The material removal rate was lower than the standard FJP process, however surface roughness was around 50% lower than the standard process.

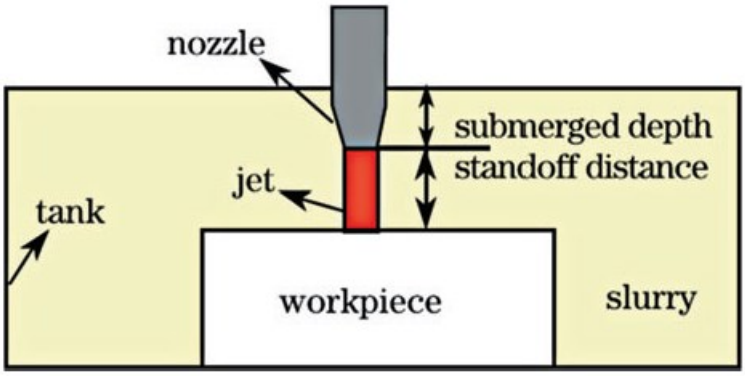

Figure 2.4: Principal of submerged MFJP process [4].

Singh *et al*. [25] reported the use of magnetorheological ball end finishing process for polishing of 3D complex geometries to finish ferromagnetic and non-ferromagnetic materials. The achieved surface roughness values for EN31 and copper workpiece were in the range of $70nm$ and $102nm$, respectively. While the method reported by Sarkar and Jain [26] used for finishing of external morphology of knee joint through abrasive flow finishing was able to achieve the surface roughness value of $42.9nm$ to $62.5nm$ with 76.56% reduction in polishing time compared to the ball end type tool. Further, Paswan et al. [27] developed a rotational magnetorheological honing (R-MRH) process for polishing internal cylindrical objects for various industrial applications and achieved 83.83% improvement in surface roughness in 40 minutes processing time.

Srivastava et al. [28] developed a novel hybrid finishing process which was a combination of two unconventional polishing methods i.e., chemical-mechanical polishing (CMP) and magneto-rheological finishing (MRF) for polishing monocrystalline silicon wafers. The experimental design was carried out using Central Composite Design (CCD) methodology and ANOVA was used to determine and analyse the contribution of significant factors affecting the surface roughness.

Wu *et al*. [29] discussed a new polishing method for free form surfaces machined using a ball end milling cutter. To eliminate the cusps generated by ball end machining, an elastic ball type tool was used for polishing free form surface of the die and mould. The automatic tool changer exchanged polishing tool after machining process and it generated better surface finished for the machined free form surface.

2.3 Process parameters and polishing tool used in fluid jet polishing process

There are some important process parameters in nanofinishing processes which play prime role in the quality of the generated surface. During mechanical grinding and polishing of moulds and dies, force variation in the direction normal to the surface have significant effect on the surface roughness. The force variation occurs due to several factors which include uneven / non-uniform workpiece surface, sudden change in direction of the polishing path, vibrations in the system and other variations arising from the environmental conditions. The following paragraph presents the literature for various process parameters that affect the quality of process output in nanofinishing using fluid jet polishing technique, which include fluid pressure, stand-off distance, polishing time, impact angle, type of abrasive particles, abrasive particle shape and size, type and quantity of machining oil in abrasive slurry, slurry concentration ratio, nozzle shape, toolpath pattern, transverse speed of the nozzle, nozzle material, hardness and other mechanical properties of the substrate material.

Table 2.1: Parameters used in FJP study by Booij [30], Hui [31] and Cao [32].

Name of Parameter	Range, Type or the Value of FJP Process Parameters			Units
	Booij	**Hui**	**Cao**	
Type of abrasive	Al_2O_3	SiC	Al_2O_3	µm
Concentration of abrasives	5	5	1:12	wt.%
Slurry medium	Water + Glycerin	Water	Water	
Workpiece material	BK7	BK9	BK7	
Type of nozzle	cylindrical	cylindrical	cylindrical	
Nozzle diameter	1.36	2.5	1.1	mm
Working pressure	5	Random	8, 10 and 12	bars
Impingement angle	45	90, 60, 45 and 30	90	degree
Stand-off distance	10	Random	10	mm
Processing time	30	5	3	min.

Various authors conducted experimental studies on FJP Polishing of ductile and brittle material. Booij [30] conducted experiments to verify the feasibility of the developed experimental FJP set up and the effect of process parameters to achieve maximum depth profile on BK7 optical glass workpiece material. Further, Hui [31] conducted experiments to investigate the effects of type of slurry and impingement angle in FJP polishing of BK9 workpiece material. It was found from the experimental results that under $20bar$ fluid pressure, material removal was negligible with pure water as compared to polishing using the slurry with SiC particles. In an additional work, Cao [32] used particle erosion model to evaluate the 3D erosion profile which was compared using the experimental data. During experimentation, Zeeko IRP200 ultra-precision freeform polishing machine was used. 2D and 3D simulation were performed to achieve material removal profile or TIF under $8bar$ fluid

pressure. It is reported that the material removal profile was purely axisymmetric and 2D erosion profile seems to be W-shaped which reflects almost zero material removal at the central working area. Table 2.1 shows the summery of the of different parameters used in the experimental investigations of FJP process by Booij [30], Hui [31] and Cao [32].

Fang et al. [33] investigated the effect of working pressure, incidence angle, the properties of the workpiece material and abrasive particles on the surface roughness. It was found that the surface finish had a linear relationship with the incidence angle and working pressure. The authors achieved a surface roughness value of around $12nm$ for an optical quality surface. Furthermore, Ho et al. [34] reported that though material removal rate can be enhanced by increasing the fluid pressure and slurry concentration ratio up to a certain level, while the excessive increase in the fluid pressure leads to the deterioration of the target surface/workpiece. Also, the higher slurry concentration ratio leads to increase in the slurry viscosity, which in turn makes the FJP process unstable. The authors recommended the values of the pressure and the slurry ratios to be $8bar$ and $6.7\mu m$ respectively for FJP polishing of Nickel copper material.

Wang et al. [10] studied the effect of stand-off distance on the surface generation mechanism and material removal characteristics. It was found from the experimental results that the suitable range of stand-off distance to polish ductile and brittle material were $25mm$ to $35mm$ and 8 mm respectively, with $1.1mm$ nozzle diameter.
Liu *et al*. [35] studied the effect of forces generated between tool and work piece during surface polishing and designed a new tool holder system with larger degree of compliance to minimize the effect of variation of generated forces. The usefulness of the designed tool on the polishing of SKD61 tool steel material with 600 mesh diamond abrasive was studied. The authors reported that the surface roughness and polishing force could be minimized by slower feed rate, higher spindle rotation, lesser abrasive grain size and higher stiffness of the spring.

Later, Ahn *et al*. [1] developed an intelligent polishing method for achieving high quality surface using acoustic emission (AE) sensor for monitoring and controlling the toolpath, tool wear rate and drastic changes in surface roughness. The developed process was enabled to determine the small variation in parameters such as fluid pressure, feed rate and abrasive mesh sizes which are generally not monitored and regulated online in other polishing methods.

Conventionally used FJP methods are unsuitable for polishing freeform, conformal and steep concave optics because of non-uniform flow jet throughout the nozzle which results in unstable removal function. To minimize jet instability effect, Tricard *et al*. [36] addressed magnetically stabilized jet of magnetorheological fluid. The authors reported that the technique was able to achieve better results for polishing complex geometries.

Sooraj and Radhakrishnan [37] developed an experimental setup for finishing internal tubular components like bush, sleeves and hollow specimens, that consisted of piston cylinder arrangement having elastic abrasive particles of $23\mu m$ grain size. The process parameters used in the study were cutting velocity, abrasive grain size, and axial pressure. The operating pressure and cutting velocity during the experiments were taken as $0.38MPa$ and $12m/min$, respectively which enabled the authors to achieve surface roughness values between $20nm$ - $30nm$.

2.3.1 Polishing tool

The selection of tool material is an important factor affecting the process efficiency and reliability. Many researchers have reported use of different tool materials and tool shapes to achieve nanofinishing surface finish. Generally, the laser machined inserts developed from diamond, ruby and sapphire are used to developed the precision nozzles from diameters ranging from $0.1mm$ to $1.5mm$ for use in FJP and abrasive fluid jet machining. The nozzles developed from diamond has maximum life while it is also the costliest material compared to ruby and the sapphire. These standard nozzle inserts are difficult to customize for experimental studies because of the cost and natural availability of the martials and also more so because of the type of manufacturing operations used to develop the nozzle inserts from these materials.

The selective laser melting (SLM) 3D metal printing process is one of the famous process that can be used for fabrication of unique tool shapes for various manufacturing applications including surface polishing. The properties of the metal used in SLM process as well as the selection of process parameters greatly influence the properties of the final 3D printed product. The preferred tool material for the polishing process should be corrosion resistant, abrasive resistant, and should have good mechanical and physical properties which must be retained in the tool fabricated using SLM process. In this regard, titanium alloy (Ti6Al4V)

which is also known as Ti64 is best suited as it is a preferred material for fabrication of high strength and corrosion resistant customized components for various applications in defence, aerospace and medical fields. The stainless steel is another good option for development of customized tools using metal 3D printing technology.

Shipley *et al*. [38] reviewed the use of Ti64 material in 3D printing process. Leauders *et al*. [39] established relationship between microstructure-defect-porosity under cyclic loading of Ti6Al4V fabricated component using SLM. The results showed that the occurrence of unfavourable microstructure due to initially formed α-martensite phase, micron sized pores mainly affects fatigue strength and residual stresses which were responsible for fatigue crack propagation. In another attempt, Gao *et al*. [40] fabricated Ti6Al4V samples using SLM process to determine the microstructures and optimize the mechanical properties with the application of heat treatment using annealing. The authors successfully developed a process to improve the yield strength, ultimate tensile strength, and elongation of Ti6Al4V to $1015MPa$, $1083MPa$ and 7.9%, respectively. Also, it is found that when the box shaped Ti6Al4V structure was stretched along the direction perpendicular to the crystal growth, the yield strength, ultimate tensile strength, and elongation were found to be $1019MPa$, $1068MPa$ and 8.7%, respectively. Similarly, in a separate study, Ali *et al*. [41] suggested that the alternate scanning strategy of 90˚ for 3D printing results in lower residual stress in the as-built state of Ti6Al4V. The authors reported that the rescanning strategy was not promising technique because 150% energy density reduces only 33.6% residual stress but had adverse effect on mechanical properties of the final 3D printed component.

2.4 CFD simulation for material removal profile in FJP Process

The concept of FJP was initially investigated by Fähnle et al. [3] and Booij [30] experimentally. Afterwards, several authors developed theoretical models and described the behaviour of material removal profile in vertical impinging mode using CFD approach. However, these models were not relatively accurate and precise and need to be further investigated to improve the process efficiency.

In this regard, Li et al. [42] used the k- ε turbulent model to visualize the fluid pattern when it eject from the nozzle outlet and concluded that k- ε turbulent model is not best suited for transition zone (between laminar-to- turbulent) in FJP. In their study, Beaucamp et al. [43]

adopted the shear-stress transport (SST) k- ω model instead to describe the slurry/air interface in the modeling of FJP, and the model was then successfully used to optimize surface texture performance down to 1 nm arithmetic roughness (Ra) on electroless nickel plated optical dies. Cao and Cheung [44] developed a CFD model for ductile-mode erosion to estimate the volume removed by a single abrasive particle in FJP. Experimental and simulation results were found to be nearly equal. A marginal variation noted in the simulated and the measured resulted was attributed to the marginal variation in actual working pressure, the surface inclination of the workpiece and the abrasion of the nozzle.

Qi et al. [45] developed a 2D model using CFD simulation to investigate the machining parameters of ultra-sonic vibration assisted abrasive slurry jet machining. In this model, the conversion of data from 2D form to 3D by means of revolving data along a central axis to achieve 3D data. But the data was only valid/suitable for 90° impingement angle mode. However, Wang [46], build universal 3D numerical model of fluid jet polishing based on CFD method, which could be used to model both vertical and oblique impingement mode. Cao *et al*. [32] proposed a theoretical model for better understanding of material removal function and surface generation based on CFD model for NiCu, BK7, and steel materials. Their results showed that relatively higher material removal rate was found in steel whereas NiCu was more resistant to erosion. Beaucamp *et al*. [43] developed and implemented dynamic multiphase modelling technique which could achieve the surface texture of $1.0nm$ in optical die. The authors optimized the performance of the slurry delivery system to achieve nanometer level surface roughness on BK7 optical glass.

2.5 Conclusions from literature review

The findings from the review of available literature has been summarised as given below:

(i) It was observed that a lot of investigations has been done on the effect of tool profile in contact and non-contact type of nanofinishing processes. A lot of work has been undertaken in studying the single nozzle fluid jet polishing process, while in the recent literature, the use of multi-jet nozzles and special tool shapes have been studied. It was found that the use of multi-jet nozzle tool is highly beneficial for achieving better quality of polished surface with higher material removal rates. Also, the multi-jet system was capable of polishing wider area per pass, which helps in polishing the given surface in lesser number of passes which in turn minimizes the polishing time.

(ii) A unique method of using a compliance tool holder mechanism in FJP was found to be effective which used the concept of using minimum clearance between workpiece and the nozzle so that the variable sized abrasive grains can easily be released without deteriorating the quality of the polished surface.

(iii) A significant amount of efforts has been made to study the interaction of various process parameters which affect the performance of FJP process. The parameters that directly affect the material removal and surface finish in FJP are fluid pressure, fluid viscosity, abrasive mesh size, slurry concentration ratio, fluid flow rate/nozzle discharge, standoff distance, hardness of the workpiece material, hardness of the abrasive particles, nozzle diameter, distance between adjacent nozzles in multi-jet FJP, transverse speed (feed rate) of the nozzle/s and rpm of the rotary fluid jet.

(iv) Some authors have focused on the study of the different models for material erosion during impingement of the abrasive particles on the work piece with change in the incident angle of fluid jet to enhance the ability of multi-jet FJP. When abrasive particle leaves the nozzle in FJP, its energy degrade substantially after striking the machined surface. Authors have even tried to improvise the mechanism of multi-jet FJP process to enhance the material removal rate, like using the ultrasonic vibration for generating micro-bubbles, etc.

2.6 Closure

This chapter discussed the literature on various methods used for nanofinishing of dies and moulds. It also gave an account of the different factors and toolings on which the process of fluid jet polishing depends.

The next chapter discusses the materials and methods that have been followed for the present work.

Chapter 3
Materials and Methods

This chapter describes the geometric design of the polishing tool, design of experimental set-up, selection of the workpiece materials, the abrasive and the process parameters used in the present study to improve the efficiency of the FJP process.

3.1 Tool design for FJP process

In this study, the customized shaped 3D printed tool with embedded nozzles are designed and fabricated. The single nozzle and multi-jet FJP tools were fabricated using titanium alloy (Ti6Al4V) and stainless steel SS316L with SLM metal 3D printing process. The shape of the tool is cylindrical with single or multi-nozzles (two-orifices) of $1mm$ diameter with h6 tolerance on the outer cylindrical lateral surface. In the present study, the single nozzle polishing tools are used to identify the shape of the tool influence function (TIF) or polishing spot with varying process parameters whereas, the multi-jet tools have been used for studying the effect of polishing parameters for improving the polishing efficiency to cover the medium to larger size surface area of the components.

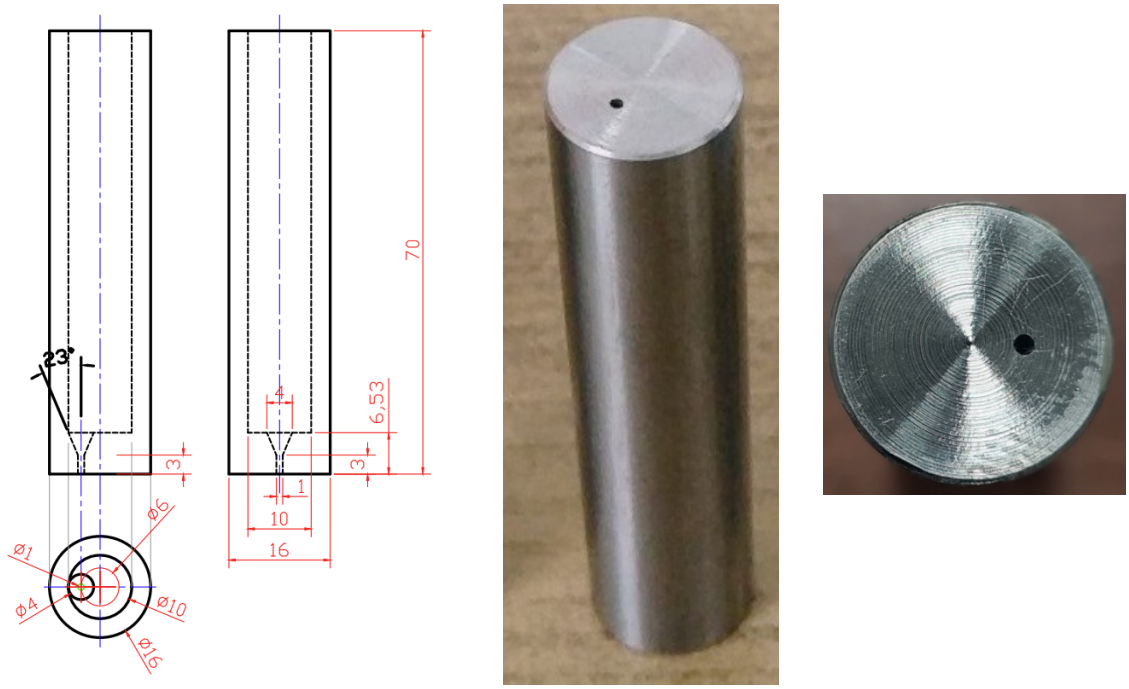

(a) (b) (c)

Figure 3.1: (a) Geometric design of customized single nozzle FJP Tool, (b) and (c) 3D printed single nozzle FJP Tool.

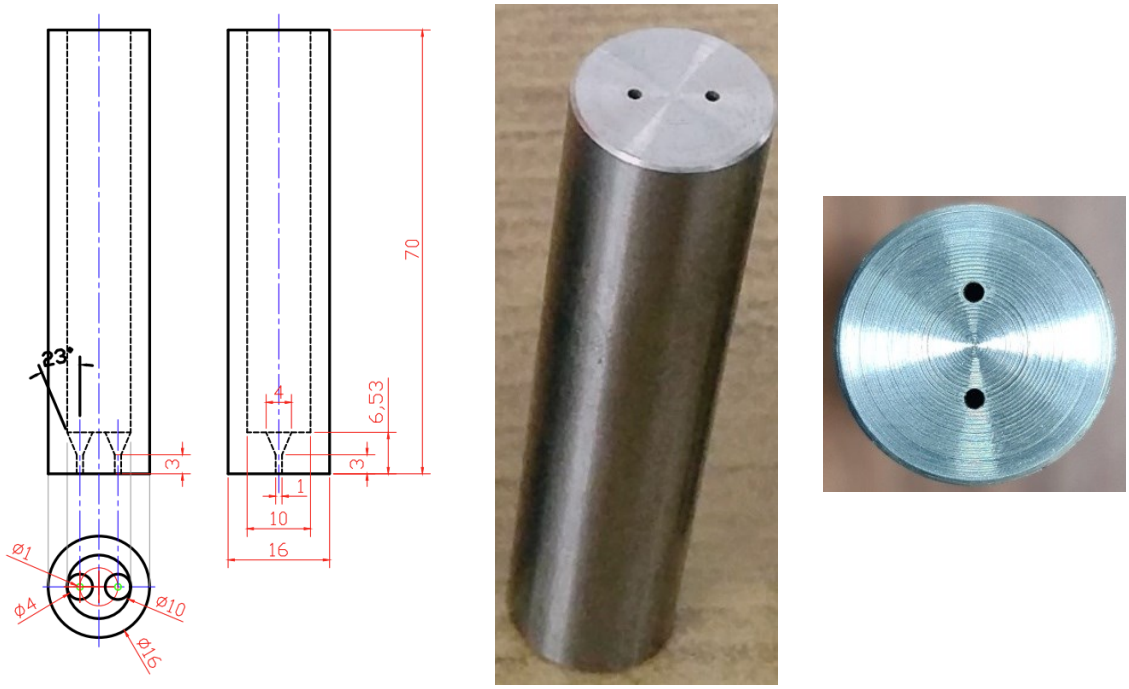

(d) (e) (f)

Figure 3.2: (a) Geometric design of customized two-nozzle FJP Tool, (b) and (c) 3D printed two-nozzle FJP Tool.

The basic shape of the single and multi-jet (two-nozzle) FJP polishing tools used in the present work are shown in Figure 3.1 and Figure 3.2 respectively. Commonly used FJP polishing tools are the inserts made from very hard materials like diamond, sapphire and tungsten carbide material to ensure the low tool wear rate and hence the longer tool life. The application of the these FJP tools is limited to commercial processes, whereas the cost of the nozzles developed from aforesaid natural material for experimental investigation is very high. Moreover, these polishing tools were only restricted to use in the normal impingement mode (90° strike angle on the workpiece surface). For achieving higher material removal rate with impingement angle varying from 90° to 45°, tool requires additional attachments as suggested by Shiou et al. [20]. To overcome this issue, the use of metal 3D printed tool is a good option where no such attachment is required. The use of multi-nozzle tools for multi-jet polishing where we can have a number of orifices and shapes of nozzle to achieve varying jet impingements (from 45° to 90°) can be easily fabricated by metal 3D printing process.

In the present work, selective laser melting (SLM) process has been used for fabrication of the FJP nozzle tool using titanium alloy, Ti6Al4V (or Ti64) and stainless steel SS316L. The Ti64 is a suitable material to fabricate components for engineering and medical application using 3D printing owing to the fact that it possesses high strength, good corrosion resistant, high fatigue and surface finish of the 3D printed parts [38]. Titanium alloys have the highest specific

strength (ratio of strength to specific weight) of all structural materials. However, the additive manufacturing process poses challenges with void formation, anisotropic behaviour, have limited selection of alloys and requires post-processing such as machining, heat treatment or chemical etching. The chemical composition, physical and mechanical properties of titanium alloy (Ti6Al4V) are given in Table A.1, A.2 and A.3 respectively in annexure A. The stainless steel SS316L is another material which has the higher hardness and is also being used in abrasive waterjet machining operations. Also, SS-316 steel can be 3D printed to a very high accuracy. In FJP process, the polishing tool is made up of hard material for longer tool life and low tool wear rate. These tools can easily be manufactured for vertical impingement mode but for higher material removal rate, the tool with impingement angle is used which requires an additional attachment [20]. This attachment can easily be manufactured using 3D printing process. Ti64 and Stainless-steel (SS316L) tool materials are hard and are commonly used as a powdered material for 3D printing process which made the reason for selecting them in the present research work. Though Ti64 and SS316L are good abrasion resistant materials and definitively not as hard as ruby or diamond inserts preferred for abrasive fluid jet polishing, but owing to the unique custom designed shape of the FJP tool used in the present study it was convenient to develop the FJP tools using 3D printing and the hardness of the FJP tool material was found to be just sufficient for the intended life of the tool for the present work.

Thus, in this work, we used the customized FJP nozzle tools developed from both Ti64 and SS316L as per the availability. The chemical composition, physical and mechanical properties of SS316L are given in Table B.1, B.2 and B.3 respectively in annexure B.

3.2 Selection of work piece and abrasive materials

The work piece materials used for finishing process in the present work are Nickel Copper (NiCu) alloy Monel-400 and AISI H13 die steel. The silicon carbide (SiC) has been used as an abrasive with water as base fluid for the fluid jet slurry. The chemical composition, physical and mechanical properties of the materials used in the present work are discussed below.

3.2.1 NiCu alloy (Monel-400)

The NiCu alloy (Monel-400) have excellent mechanical properties, is being widely employed as heat-resistant, corrosion resistant metal with application in electrical engineering and manufacturing of optical mould inserts. Monel-400 is one of the preferred materials for optical dies which are used to fabricate the lenses for high resolution devices [5]. The chemical

composition, physical and mechanical properties of NiCu (Monel alloy-400) are given in Table C.1, C.2 and C.3 respectively in Annexure C.

3.2.2 AISI H13 die material

AISI H13 tool is chromium hot work tool steels which are widely used in hot and cold work tooling applications. H13 tool steel is classified as group H steels by the AISI classification system. This series of steels start from H1 to H19 [47]. In AISI H13, the molybdenum and vanadium act as strengthening agents. The chromium content assists die steel, H13 to resist softening when used at high temperatures. H13 die steels offer an excellent combination of shock and abrasion resistance, and possesses good red hardness. It is capable of withstanding rapid cooling and resists premature heat checking. H13 tool steel has good machinability, good weld ability, good ductility, and can be formed by conventional means. Due to its excellent combination of high toughness and fatigue resistance, AISI H13 steel is used more than any other tool steel in tooling applications. The chemical composition and mechanical properties of H13 Tool Steel are given in Table C.4 and C.5, respectively in Annexure C. The application of H13 as extrusion and plastic moulding tool steel are shown in Table C.6 and C.7, respectively in Annexure C.

3.2.3 Silicon Carbide abrasive particles

In multi jet polishing process, the cutting action is caused by the abrasive particles, which have the biggest influence on the quality of the polished surface. If the particle sizes are smaller, the material removal rate from the substrate surface will be lesser but the quality of the polished surface will be better. It is recommended in the available literature that the threshold values of abrasive particle size should be less than $100nm$ for the fluid jet polishing process [4]. The selection of abrasive material mainly depends on the density, physical properties and target surface roughness to be achieved from the FJP process. The commonly used abrasive materials being used in the FJP and the other abrasive waterjet machining processes are Silicon Carbide, Cerium Oxide, Boron Carbide or Aluminium Oxide and diamond. Out of the mentioned abrasive materials Silicon Carbide has the highest hardness value of 9.5 on Mohs scale.

3.3 Selection of FJP Process Parameters

The process parameters that influence the quality and the reliability in FJP process includes fluid pressure (P), stand-off distance (D), polishing time (T), impact angle (α), type of abrasive particles, abrasive particle shape and size, type and quantity of machining oil in

abrasive slurry, slurry concentration ratio, nozzle shape, nozzle material, hardness and other mechanical properties of the substrate material [4]. As observed from the literature reviewed, out of the enlisted process parameters the most critical are the jet pressure, stand-off distance and the polishing time [5]. These parameters play an important role for improving the polishing efficiency in the FJP Process and hence their study for the targeted materials is a must.

In the FJP process, the when abrasive particles leave the nozzle outlet contains huge amount of energy. The abrasive particles contained in the outermost streams of the fluid jet tend to lose some part of their energy due to the air drag while noticeable amount of energy of the abrasive particles is lost within the stagnation zone where they strike each other before almost slowing down while touching the workpiece surface as discussed in section 1.5 in Chapter 1. The loss of energy of the abrasive particles in the stagnation zone can be prevented marginally by a combined effect of rotation of the fluid-jet about an offset axis along with the movement of the rotating nozzle-jet tool along the feed direction. The rotation of the fluid-jet assists in augmenting marginal kinetic energy to the abrasive particles in the fluid-jet due to the addition of horizontal velocity component V_x in addition to the existing kinetic energy levels due to the vertical velocity component V_y of the abrasive particles. This is the reason why the custom designed single-nozzle and two-nozzle FJP tools have the position of the nozzle/s located away from the tool-axis as shown in Figure 3.1 and Figure 3.2.

The phenomenon of rotation of the vertical abrasive fluid-jet emanating from the nozzle located offset from the rotating tool-axis has been found to be beneficial for achieving relatively better surface finish levels in our preliminary investigation. Thus, the study for the optimization of FJP process parameters including the rpm of the rotating fluid-jet has the potential to enhance the polishing efficiency. Thus, the new parameter introduced in our work is the study of the effect of the rotation of the vertically striking abrasive fluid-jet or the spindle rotation per minute (rpm).

The different spindle rotations can generate different surface finishes in the FJP process. The spindle rpm can be directly used to estimate the shear energy in an abrasive particle of a particular mesh size. At the same time a higher spindle rpm may distort the shape of the vertical fluid-jet because of higher air drag. Thus, an initial estimate for the spindle rpm can be made for the given mesh size of abrasive particle to be used for FJP process study. An initial estimate

of amount of shear energy required when the abrasive particle strikes some particular peak to valley of the roughed surface having particular hardness would help in better design of the experiments.

Table 3.1 contains the list of the various FJP process parameters studied to achieve nano scale surface finish with the 3D printed fluid-jet polishing tools on a 3-axis CNC vertical milling machine having $1\mu m$ positioning resolution with an accuracy and repeatability of $\pm 10\mu m$ and $\pm 5\mu m$, respectively. These ranges of the process parameters are identified from the available literature along with the initial trials which were conducted on the developed experimental set-up. The range of fluid pressure and abrasive particle size are selected based on the experimental trials and the recommended range for FJP polishing [4,5,6,10,19,20]. The experimental test rig we used in this work is designed for fluid-jet delivery at maximum pressure of $12.5 bar$ and from the initial trials we have observed that below $4 bar$ pressure negligible material removal takes place for Monel-400 and H13 die steel. The range of stand-off distance for polishing ductile material to achieve the "U" shaped TIF profile is reported by Wang [10] which lies in the range of $24 mm$ to $36 mm$. The range of polishing time is selected between $90\ seconds$ to $210\ seconds$ on the basis of available literature [4-6] and the initial trials where it is found that this range of polishing time offers the better surface finish. The selection of feed rate value of $20 mm/min$ is also done on the basis of the literature [4] and the initial trials to achieve nano scale surface finish both in case of non-rotary and the rotary fluid-jet. The design of the nozzle shape and the number of orifice (one or two) in the customized FJP tool is also based on the recommended nozzle parameters suggested in the literature [48-49].

Table 3.1: FJP process parameters used in the present study.

S. No.	Process Parameter	Range
1	Finishing of the grinded input workpiece surface	>1000 nm
2	Pressure of the fluid jet	4-12 bar
3	Stand-off distance	24-36 mm
4	Polishing time	90-210 seconds
5	Spindle rotation	50 to 100 rpm
6	Horizontal traversing rate of the tool (feed rate)	10-50 mm/min
7	Mesh/grain size of the abrasive particles	4000 mesh/ 3.2 microns
8	Number of orifices in the nozzle	1 and 2
9	Nozzle orifice diameter	1 mm

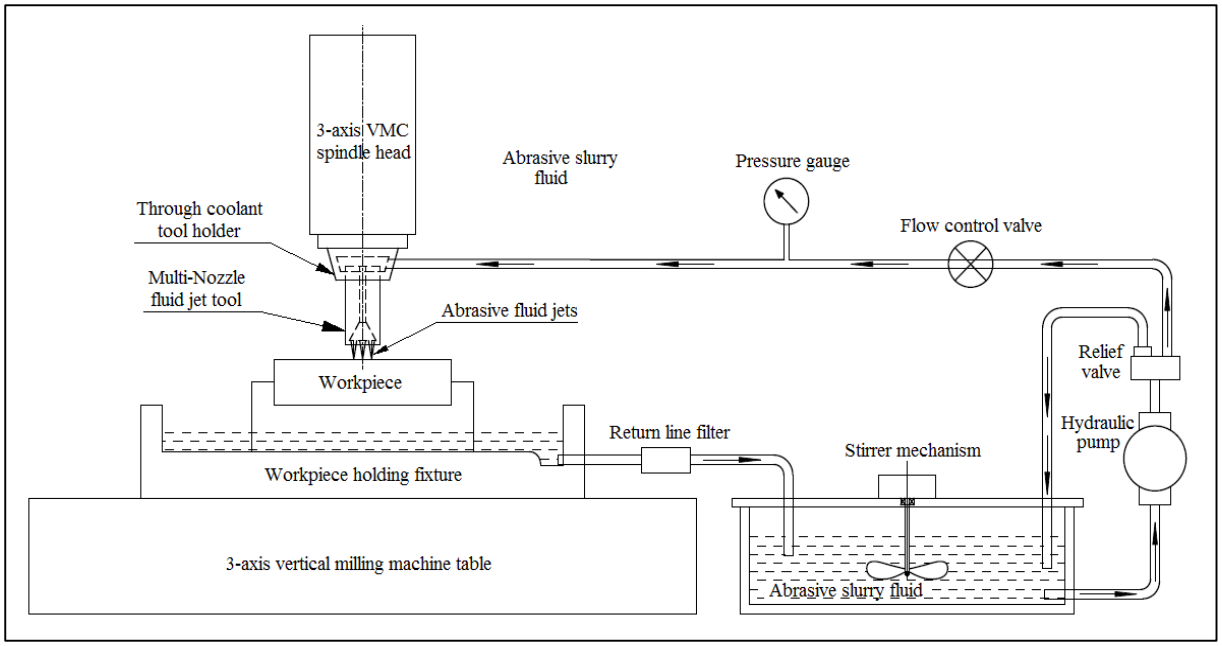

Figure 3.3: The layout of the experimental set-up designed for the present work.

3.4 Experimental Setup

The Figure 3.3 shows the layout of the experimental set-up designed and developed for the present work. The actual experimental set-up, shown in Figure 3.4 and 3.5, has been developed for delivering the slurry-fluid to the 3D printed embedded nozzle tool at pressure ranging from $2bar$ to $14bar$. The FJP set-up consists of a 3-axis CNC vertical milling centre attached with a BT40 coolant inducer tool holder, a geared stirrer with a range of $180 - 650rpm$, a vertical multistage centrifugal pump of $14.75bar$, a diaphragm type pulsation dampener, ball valves for regulating slurry flow, a pressure regulating valve (PRV), a non-return horizontal and horizontal valves, a Y-stainer filters, pressure sensors (marked as PS1 and PS2), three pressure gauges (marked as PG1, PG2 and PG3). The x, y and z-axis traverse of the CNC machine tool used in the developed experimental set-up is $800mm$, $350mm$ and $380mm$ respectively.

The customized 3D printed multi-nozzle rotary tool was fixed inside the BT40 coolant inducer assembly on a 3-axis vertical CNC milling machine. The coolant inducer assembly is the tool holder attachment for the CNC machines which do not have through coolant spindle option. Figure 3.6 shows the BT40 coolant inducer tool holder assembly that has been used for holding the custom design FJP tools using the sealed collet to prevent the leakage of the pressurised abrasive fluid. The BT40 coolant inducer assembly made it possible for delivering the

pressurized abrasive slurry mixture from the pump to the tool mounted on the rotating or the stationary spindle of the 3-axis vertical CNC machine tool.

The slurry tank shown in Figure 3.4 has been used to prepare a homogenous mixture of abrasive particles of 4000 mesh size ($3.2\mu m$) with water as the base fluid. The abrasive slurry is pumped to pass through the converging nozzle/s of the custom developed FJP tool held in the rotating spindle of the CNC machine as shown in Figure 3.7. The composition of the slurry was the mixture of 94% pure water (by weight) and 6% silicon carbide (SiC) abrasive (by weight). The viscosity of the slurry was measured by using Modular Compact Rheometer (MCR 102 SN81405169). The viscosity of the abrasive slurry was measured before the start of the experimentation. The embedded nozzle designed in the 3D printed FJP tools have a convergent-throat design with 1.0mm exit diameter and 3.0mm as the nozzle throat length as shown in the Figure 3.1 and 3.2. The nozzle throat length was decided based upon reducing the effect of carrier fluid attachment against the outlet wall and to achieve the streamlined flow of slurry jet [48,49]. The shape of the tool was selected based on the available literature. According to A.T. Beaucamp [4], the convergent-throat shape leads to better results compared to other shapes. It is due to the reason that there is no development of cavitation near vena-contracta region due to depressurization of fluid jet beam and have lesser convergence losses as the flow is uniform in the throat region.

The abrasive particles in the slurry-jet strikes onto the workpiece surface and cause the removal of the material from the workpiece surface because of the abrasion and shear effect, which in turn generate the nanoscale surface finish.
The following are the limitations of the developed experimental set-up:

(i) The experimental test rig was only restricted for polishing flat surfaces. To polish free form or curved surface, the 5-axis or higher machine along with the additional attachment is required.
(ii) The set-up consist of vertical multi-stage centrifugal pump which is subjected to wear due to the higher speed rotation of abrasive slurry.
(iii) The size of polished area depends upon the maximum limits of the 3-axis CNC vertical milling centre used in the experimental set-up. The x, y and z-axis traverse of the CNC machine tool used in the developed experimental set-up was 800 mm, 350 mm and 380 mm, respectively.

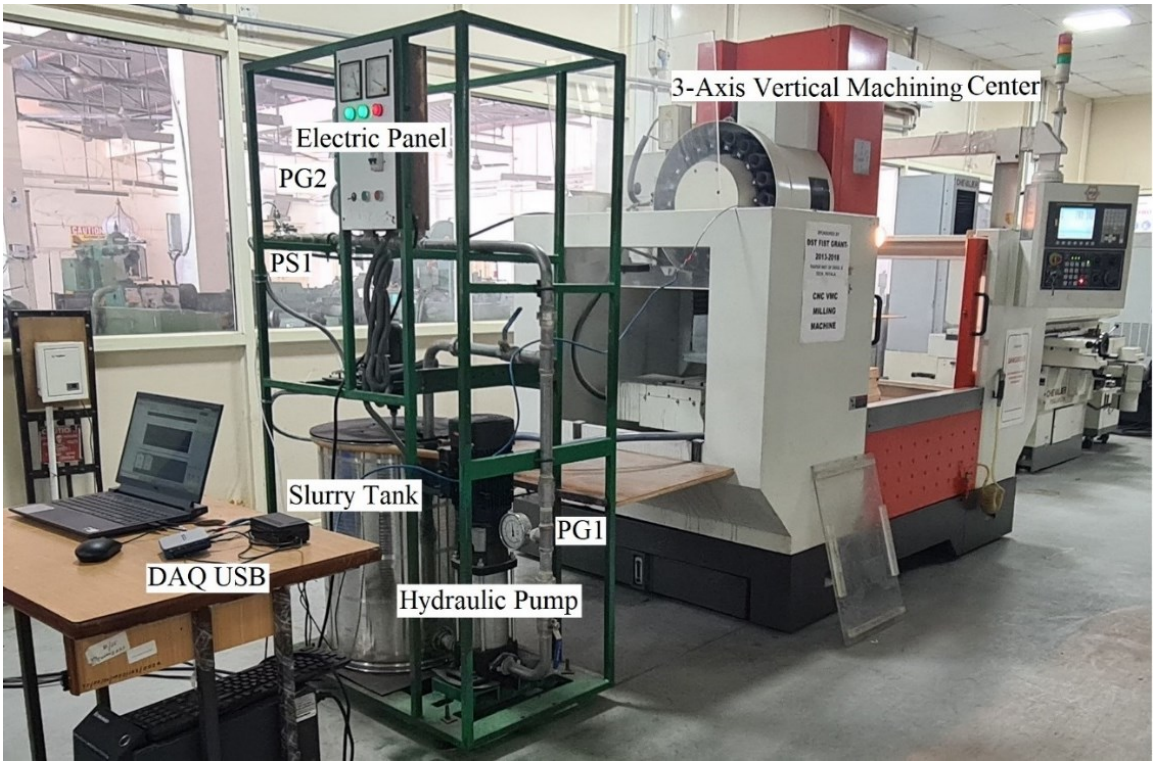
3-Axis Vertical Machining Center
Electric Panel
PG2
PS1
Slurry Tank
PG1
DAQ USB
Hydraulic Pump

Figure 3.4: The experimental test rig developed for the FJP study in the present work.

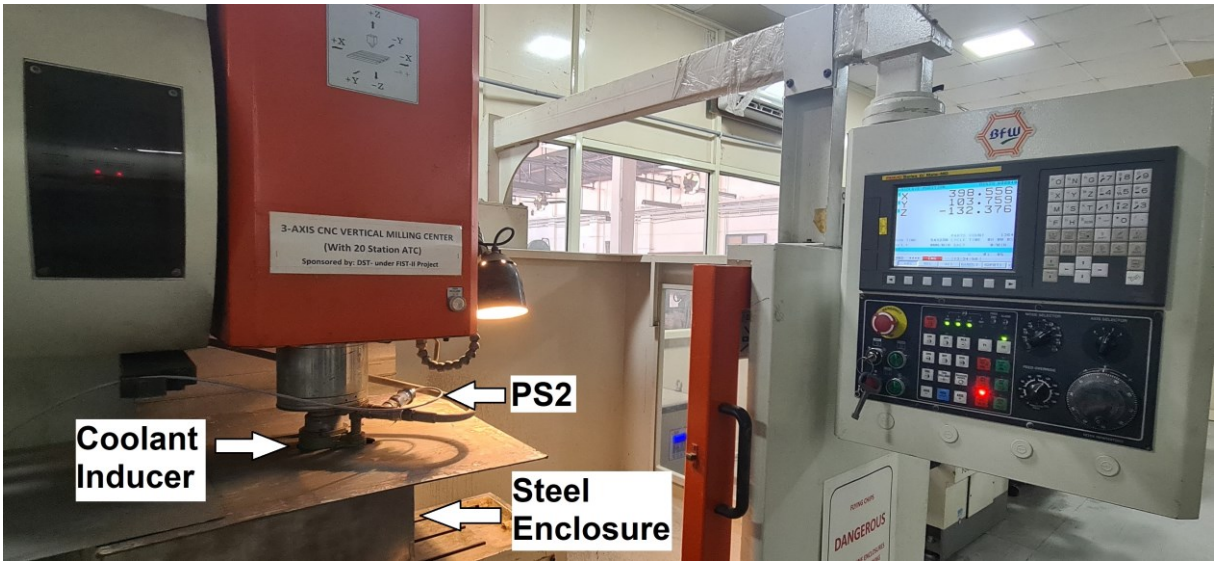

Figure 3.5: BT40 coolant inducer mounted on the spindle of 3-axis vertical CNC milling centre with the pressure sensor (PS2) mounted at the inlet of BT40 coolant inducer.

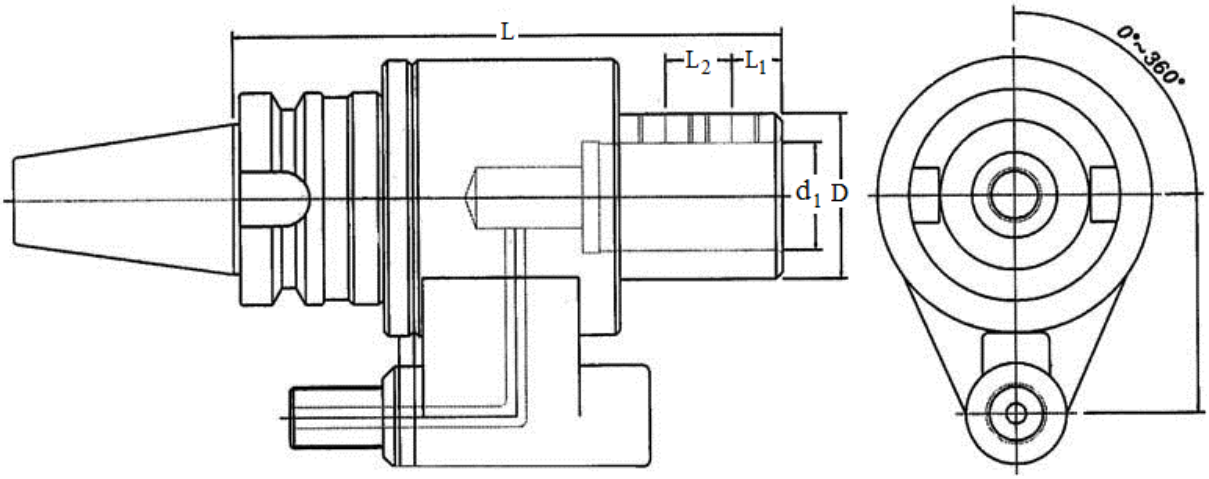

Figure 3.6: BT40 coolant inducer tool holder assembly used in the present work.

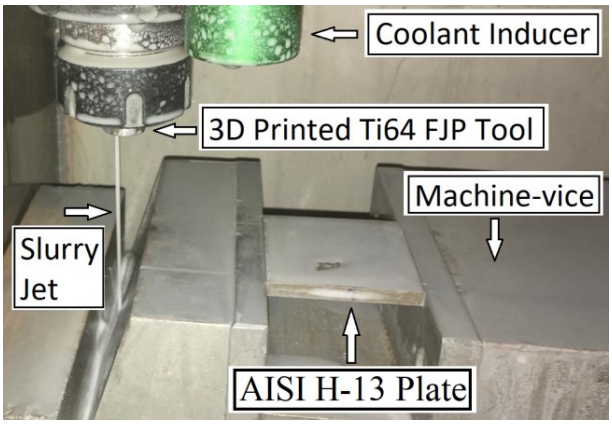

(a)

(b)

(c)

Figure 3.7: (a) The profile of the single-nozzle slurry-jet and the work holding vice, (b) consistency of the abrasive slurry-jet obtained and (c) the image shown two-nozzle slurry-jet delivered from the developed experimental set-up.

In order to achieve the streamlined flow and better binding of the abrasive particles in the slurry jet for longer stand-off distances, HOCUT 795-H water-soluble high performance machining oil was used. The presence of machining oil in the slurry jet also improves the sliding of

abrasive particle across the surface, thereby reducing the embedment effect of because of the vertically impinging fluid-jet and improves the surface finish as compared to the surface finish obtained using only water based abrasive slurry [11]. The length of the stream of the slurry-jet obtained from the developed experimental set-up for single-nozzle and two-nozzle tool has been shown in Figure 3.7.

The experimental setup was designed such that the slurry-jet remains vertical and strikes normal to the workpiece surface as shown in Figure 3.3 and Figure 3.7. The abrasive slurry, after striking the workpiece surface, is collected in a stainless-steel container mounted on the CNC table as shown in Figure 3.7(c). The slurry was then passed through a number of filters and is reclaimed in the main slurry tank for reuse. As per the working pressure range, it is assumed in the present work that there will be no cavitation effect in the set-up.

3.4.1 Inlet pressure stability

The experimental test rig is bound to have variation in the nozzle pressure owing to the pulsation generated from the slurry pump. It is known that the stability of the inlet pressure is an important factor in the FJP process to achieve the desirable surface finish [43]. The quasi-static linear rise in temperature was observed in the slurry tank and this linear variation of the temperature achieves steady state.

After achieving the steady state temperature, the variation in the pressure at the inlet of the coolant inducer assembly was noted for the planned range of pressure using two pressure sensors (marked as PS1 and PS2 shown in Figure 3.4 and 3.5). These identical pressure sensors from Applied Measurements Ltd., UK have a range of pressure from $0bar$ to $16bar$. The pressure sensors have been coupled with a NI-USB-6002 data acquisition card from National Instrumentation to get the pressure data in a personal computer.

The variation of the pressure as noted from the developed test rig for $4bar$, $8bar$ and $12bar$ pressure is shown in the Figure 3.8. The measured inlet pressure at the coolant inducer assembly showed variation in the order of $\pm\ 0.1bar$ for the entire run of 5 minutes for each of the three different sets of observations as shown in Figure 3.8. The minor variations in the mean pressure can be attributed to the minor turbulence due to the abrasive particle and the minor variation in the rpm of the vertical multistage centrifugal slurry pump.

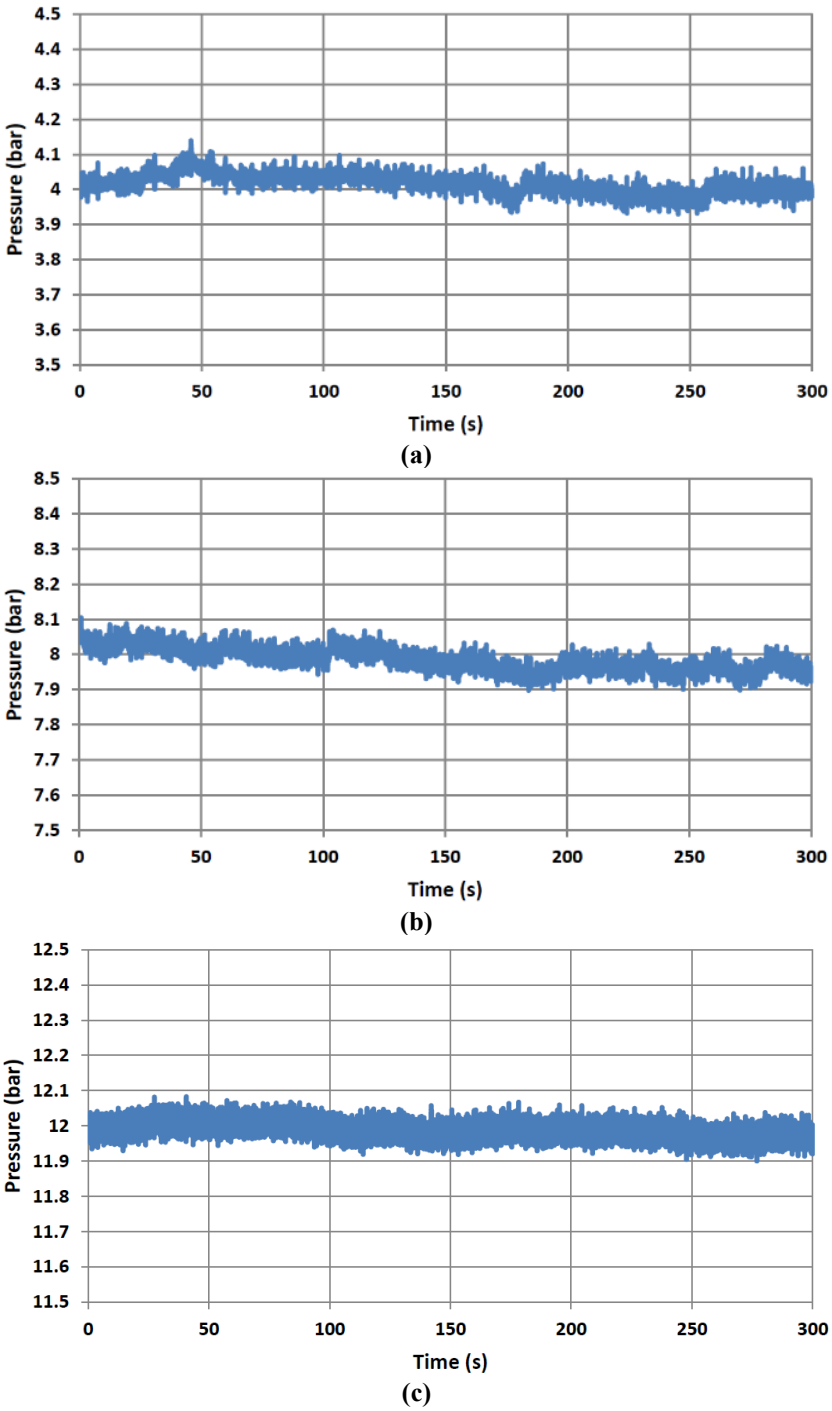

Figure 3.8: Pressure stability of the abrasive slurry line measured by the pressure sensor PS2 at the inlet of coolant inducer assembly at (a) 4 bar (b) 8 bar and (c) 12 bar.

3.5 Sample preparation

There is an increasing need for high quality surface finish in ultraprecision dies and components in specialized applications like optical lenses used in remote sensing, broadcasting, medical and defence [5]. The precision optical dies used to fabricate the optical lenses use hard and corrosion resistant materials. Monel-400 (NiCu alloys) material is one of the preferred

materials for optical dies used to fabricate the lenses for high resolution devices [12]. The other type of dies used to fabricate non-optical precision components need to have good mechanical properties like toughness, hardness, and sufficient resistance to with stand high temperature fatigue cycles. AISI H13 die steel material is one of the preferred materials for dies used to manufacture a variety of precision components.

It is desirable to design and manufacture die and moulds that are free from surface defects, cracks and have better service life [50]. The surface finish of the die and mould plays an important role in the quality of the finish good as well as the life of the die and mould. The better surface finish on the die surfaces tend to resist the formation of surface cracks and other undesirable phenomenon like pitting, cavitation and surface irregularities [4]. Thus, in the present work, two type of workpiece materials, one for optical and another used for non-optical applications, have been used for studying the FJP process, namely: NiCu alloy Monel-400 and AISI H13 die steel material.

The sample preparation is the initial stage of FJP process where workpiece surfaces were machined using the end milling operation. The sample surfaces were then grinded to eliminate the uneven marks and to enhance the surface finish by reducing the irregularities from the substrate surfaces in the range less than $500nm$. After, the grinding operation the workpiece surfaces were cleaned using the acetone solution and dried before conducting experiments using FJP process. The initial surface roughness was measured for all the test surfaces before proceeding for the experimental studies of FJP polishing.

3.6 Measurement and characterization techniques

The surface roughness (Ra) values for the test surfaces were measured using SJ-400 Mitutoyo surface roughness profilometer with $0.25mm$ and $0.8mm$ cut-off lengths. The surface roughness was measured at three different locations and their average value was taken. The 3D topography of material removal profile was measured using Zeta-20 optical microscope.

The hardness of the materials was measured with the help of micro-hardness tester (Mitutoyo HM-210 model) with an accuracy (least count) of $0.0001HV$. The hardness tests were carried with a load of $300gms$ and dwell time as 20 seconds. The diamond indenter was used to measure the micro-hardness on the ground and FJP polished surface of Monel-400 and AISI H13 die steel workpiece. The hardness value obtained after the test was in Vickers Pyramid

Number (HV). The average hardness values before and after polishing were measured at 10 different positions on the workpiece.

3.7 Design of experiments

The statistical tool known as Design of Experiments (DOE) is used in the design and optimization studies of systems, processes and product. DOE can also be used for design comparisons, variable screening, transfer function discovery, optimization, and resilient design studies. DOE is a field of applied statistics used to carry out scientific investigations of a system, process, or product where the input variables (X) are changed to investigate their influence on the response variable (Y).

An enhanced design of experiments (DOE) methodology known as a response surface helps to better understand and optimise the response parameters. The most popular method, Central Composite Design (CCD), bases its construction on a factorial design. It includes axial points known as star points as well as central points. The estimation of the quadratic terms is made possible by CCD's three-level examination of each factor. CCD can fit a complete quadratic equation and is most often used when sequential experimentation is required in the design plan, allowing these designs to incorporate data from well organised factorial experiments.

There are mainly two DOE methods of fitting response surfaces by identifying various locations in the design space are the Central Composite Design (CCD) and Box-Behnken Design (BBD) models [51]. The lesser number of degrees of freedom in BBD accounts for the discrepancies between CCD and BBD models. The benefit of BBD is that it assumes fewer runs for the three components, whereas this method is not suitable for four or more variables. The understanding of analysis of variance (ANOVA) and linear regression is necessary in order to implement and interpret the results depicted by the DOE approaches. In this work we have used the CCD approach of Response Surface Methodology (RSM) for planning of the experimental studies as well as to analyse and interpret the finding of the DOE studies on the FJP polishing.

3.8 Preliminary computational fluid dynamics (CFD) study

This section discusses the preliminary computational fluid dynamics (CFD) study of the associated FJP process for basic understanding of material removal profile at lower standoff distances on Monel 400 (NiCu alloy) workpiece surface. The CFD simulation helps to visualize the effect of multiphase flow (Interaction of air, water and abrasive particles) and determine pressure, velocity and erosion rate distribution onto the substrate surfaces. It also provides the

information related to material removal profile or tool influence function (TIF) at vertical and inclined impingement modes.

3.8.1 Geometric modelling

The Figure 3.9 shows the geometric model of the FJP process using single nozzle tool. The convergent-throat type of nozzle was modelled for the CFD analysis. The hexahedral mesh, shown in Figure 3.10, was used to achieve accurate results using simulation on ANSYS 2020R1 platform. The workpiece material was Monel-400 (NiCu alloy) with silicon carbide (SiC) abrasive of 4000 mesh size and $1mm$ nozzle diameter.

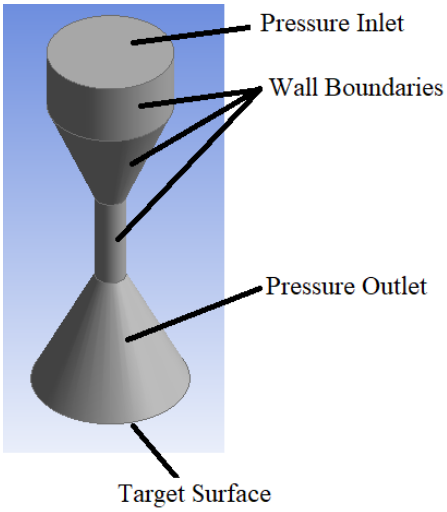

Figure 3.9: Geometric modelling of Fluid jet polishing process with single nozzle tool.

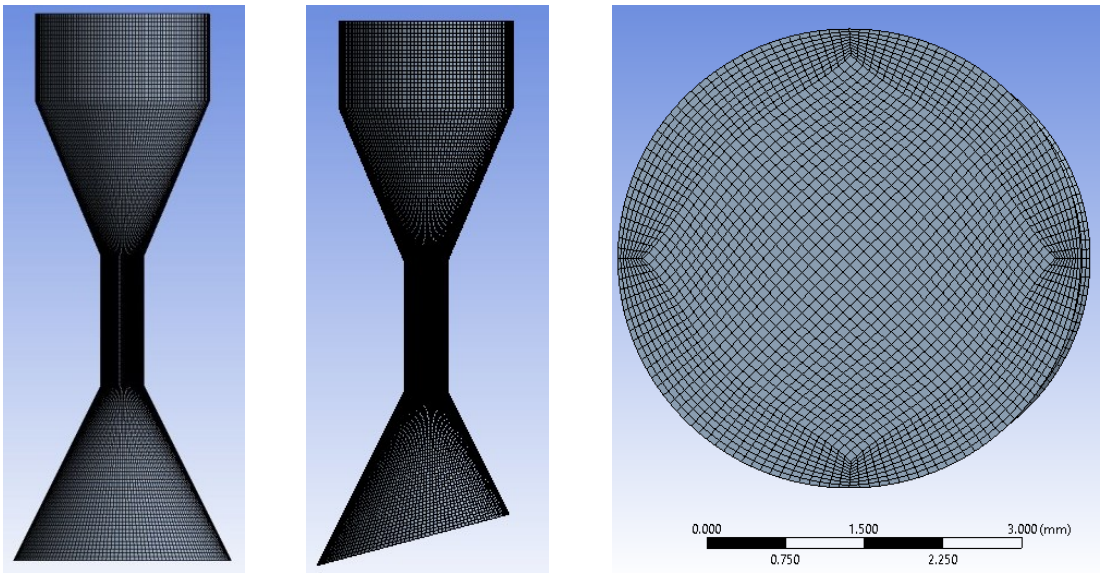

(a) **(b)** **(c)**

Figure 3.10: Meshed models for study of, (a) vertical impingement of abrasive particles (b) oblique impingement of abrasive particles, and (c) the bottom view of the meshed model used in vertical and oblique impingement studies.

3.8.2 Multiphase fluid flow model

The Eulerian-Lagrangian approach was used to simulate the multiphase fluid flow which includes water, air and abrasive particles. During the analysis, air and water were treated as Eulerian phase while, abrasive particles were treated as Lagrangian phase. Following assumptions have been considered during the CFD analysis:

(a) negligible tool wear and heat generation in the domain,

(b) shape and size of abrasive particles is considered uniform throughout,

(c) slurry concentration is constant, and

(d) particle to particle interaction is negligible during fluid flow.

3.8.3 Continuous phase model

In FJP process, the fluid domain has been assumed to be incompressible, having constant temperature and constant density. The Navier-stokes equation, Equation (3.1), has been used for describing the fluid flow condition [11].

$$\rho\left(\frac{\partial v}{\partial t} + v.\nabla v\right) = -\nabla p + \mu_f \nabla^2 v + F_e \tag{3.1}$$

Where, ρ is the density, p is the pressure of the fluid-jet, μ_f is viscosity, v is velocity field and F_e denotes the applied external force.

To study the influence of turbulence inside the flow domain, the shear stress transport (SST) based $K-\omega$ and $K-\varepsilon$ models have been used to express the turbulence inside the fluid flow domain [52]. Simple algorithm was used to solve the pressure-velocity relationship, particle treatment selected was unsteady particle tracking, turbulent dispersion model was considered as discrete random walk model and gradient was based on least square cell.

3.8.4 Discrete phase modelling

The particle trajectories were evaluated by discrete phase modelling (DPM) [53]. Abrasive particles were treated as Lagrangian phase in DPM. The change in particle velocity is directly dependent on drag force and external forces which can be described by Equation (3.2).

$$\frac{dv_p}{dt} = F_D\left(v - v_p\right) + \frac{g(\rho_p - \rho)}{\rho_p} + F \tag{3.2}$$

Where, ρ_p is density of the particle, F_D is drag force, second term in the equation represents the gravity force and F is an external forces. Equation (3.3) represents the drag force.

$$F_D = \frac{18\mu C_d R_e}{\rho_p d_p^2\, 24} \tag{3.3}$$

Where, d_p is diameter of the particle, R_e is the Reynolds number and C_d coefficient of drag. Other forces were assumed to be very small compared to the drag force and hence considered negligible during the simulation.

3.8.5 Particle rebound velocity model

The particle rebound model was used to visualize the wall effect because the abrasive particle may collide with the wall boundary, lose its kinetic energy and mix with the main fluid flow domain. This model was first given by Grant and Tabakoff [54] to determine the particle trajectory and rebound velocity after striking. The coefficients of normal (e_n) and tangential (e_t) components were given by Equation (3.4) and Equation (3.5), respectively.

$$e_n = 0.993 - 1.76\theta_i + 1.56\theta_i^2 - 0.49\theta_i^3 \quad (3.4)$$

$$e_t = 0.988 - 1.66\theta_i + 2.11\theta_i^2 - 0.67\theta_i^3 \quad (3.5)$$

Where, θ_i is the impact angle (radians)

3.8.6 Erosion model

The mechanism of material erosion in FJP process is best modelled using Oka's erosion model [55]. The basic input parameters used in the models are: impact angle (θ), material hardness, particle impact velocity, and the particle diameter (D_p).

Oka's Model defines the erosion damage (mm^3/kg) at a different impact angle using Equation (3.6) to Equation (3.10).

$$E(\theta) = g(\theta)E_{90} \quad (3.6)$$

$$\text{Where, } g(\theta) = (\sin\theta)^{n_1}\left(1 + Hv(1 - \sin\theta)\right)^{n_2} \quad (3.7)$$

$$E_{90} = K\,(Hv)^{k_1}\left(\frac{V_p}{V'}\right)^{k_2}\left(\frac{D_p}{D'}\right)^{k_3} \quad (3.8)$$

$$n_1 = s_1(Hv)^{q_1} \quad (3.9)$$

$$n_2 = s_2(Hv)^{q_2} \quad (3.10)$$

Where, $g(\theta)$ is the impact angle depending upon two trigonometric functions, Hv is the vickers hardness number of the material expressed in *GPa*, n_1 and n_2 are exponents calculated by material hardness and impact conditions, E_{90} is the erosion damage, V_p and V' are the particle velocity and the reference velocity in m/s, D_p and D' are the particles diameter and reference diameter expressed in µm, K denotes particle properties including particle shape and hardness, other factors; k_1, k_2, k_3, q_1, q_2, s_1 and s_2 are the exponents and constants values used in the

erosion model. Table 3.2 shows the coefficients and exponents while, Table 3.3 represents the properties of the workpiece material used in the simulation.

Table 3.2: Coefficients used in erosion model [55,56].

Coefficients	k_1	k_3	s_1	s_2	q_1	q_2
Values	-0.05	0.19	0.71	0.14	2.8	-1

Table 3.3: Workpiece material properties.

Materials	Monel-400 (NiCu alloy)	SiC
Density (kg/m3)	8800	3160
Hardness of the material (Vicker's hardness (GPa)	1.363	27.445

The substrate surface erosion rate $R_{erosion}$ (kg/m^{2}s) is expressed as:

$$R_{erosion} = \sum_{p=1}^{N_{particles}} \frac{\dot{m}_p ER}{A_{face}} \tag{3.11}$$

$$ER = 1 \times 10^{-09} \rho_w E(\theta) \tag{3.12}$$

Where, ER is the erosion ratio, $\dot{m}_p$ is the mass flow rate of the particle in (kg/s), A_{face} is the area of the face on target surface expressed in m^2, and ρ_w is the density of the workpiece material expressed in kg/m^3.

3.8.7 Simulation parameters, boundary conditions and the model setting used in CFD analysis

The Table 3.4 and Table 3.5 show the set of simulation parameters, boundary conditions and the model setting used in preliminary CFD simulation analysis to compare the results for the vertical and oblique impingement of the abrasive-fluid jet for stand-off distance from $4mm$ to $20mm$. In this chapter we have presented the CFD results for $4mm$ stand-off distance to keep the discuss concise. This is because the simulation results for all stand-off distance from 4mm to $20mm$ have similar trends for vertical and oblique impingement of the abrasive fluid jet. Moreover, the CFD solver could not converge for the simulations for stand-off distance beyond $20mm$.

Table 3.4: Simulation parameters and boundary conditions.

S. No.	Input Process Parameter for the study	Range
1	Abrasive particle size (SiC),	4000 mesh (3.2µm)
2	Slurry concentration in water,	6% (by weight)
3	Nozzle diameter,	1.0 mm
4	Pressure of the fluid jet, *P*	8 bar
5	Stand-off distance, *D*	4 mm to 20mm
6	Impingement angle, α	90° and 75°
7	Workpiece material	Monel 400 (NiCu alloy)

Table 3.5: Model setting for CFD analysis.

S. No.	Model setting [46]	
1	Multi-phase model	VOF model
2	Body force	Implicit body force
3	Viscous model	Turbulence
4	Turbulence model	SST K-W model
5	Particle Treatment	Unsteady particle tracking
6	Turbulent dispersion	Discrete random walk model
7	Solver type	Pressure-based
8	Pressure-velocity coupling	SIMPLEC
9	Gradient	Least squares cell based
10	Upwind scheme	Second-order

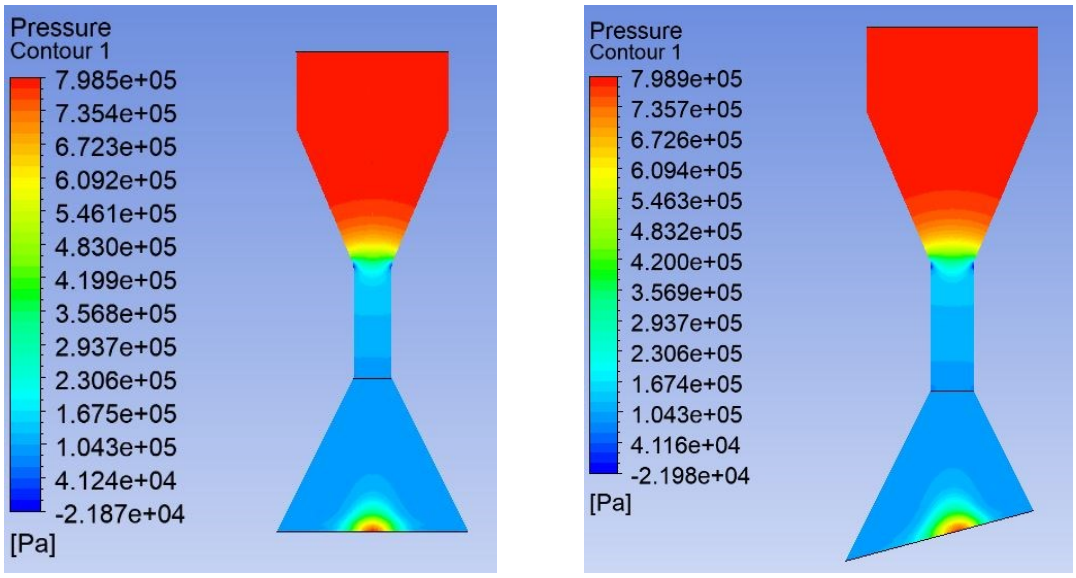

(a) **(b)**

Figure 3.11: Simulation results of fluid pressure distribution at (a) vertical impingement and (b) oblique impingement.

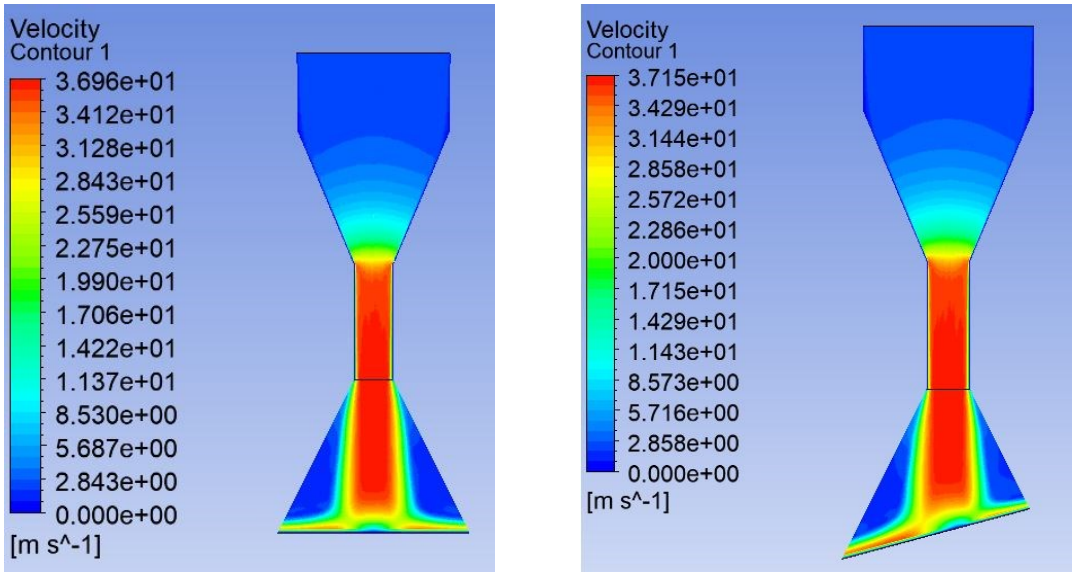

(a) **(b)**

Figure 3.12: Simulation results of velocity distribution at (a) vertical impingement and (b) oblique impingement.

3.9 Effect of pressure and velocity distribution on target surface

The abrasive particles flowing in the fluid-jet just after leaving the nozzle follows the Gaussian distribution curve due to environmental drag force at the outlet. The Figure 3.11(a) and 3.11(b) shows the variation of pressure and velocity profiles when the abrasive fluid-jet strikes the substrate surface in normal and oblique impingement mode. It can be seen from the Figure 3.11(a) and 3.11(b) that the pressure is maximum at the central part of jet striking the substrate surface (called the stagnation zone), due to which the velocity of the abrasive particles is stagnated at the centre of the impact point in the stagnation zone. This is because of the reason that the abrasive particles in stagnation zone partially lose its kinetic energy when they strike on to the substrate surface as shown in Figure 3.12(a) and 3.12(b), respectively.

3.10 Effect of material removal on target surface

For vertical impingement of the abrasive fluid-jet, the slurry fluid flow uniformly in all direction leading to the uniform axisymmetric erosion distribution over the substrate surface as seen in Figure 3.13(a). It is observed from Figure 3.13(a), that there is an uncut material at the central part which is attributed to the fact that velocity of the abrasive particles near the substrate surface is almost zero in the stagnation zone. It is can be observed from the Figure 3.13(a) that the sectional view of the tool influence function (TIF) will have the W-shaped profile (similar to the one shown in Figure 1.9(a) or 1.9(b)), when the pressurized abrasive fluid-jet strikes normal to the surface. On the contrary, when the abrasive fluid-jet strike at an oblique angle to the substrate surface we get an unsymmetrical or distorted erosion/ material removal profile as shown in Figure 3.13(b).

Also, it is worth noticing that the magnitude of the total material removal is more in oblique impingement mode as compare to vertical impingement because abrasive particles gain sufficient energy for chipping off material from the substrate surface without losing any significant kinetic energy compared to the vertical impingement.

Form the CFD analysis presented above, it is found that the vertical implement is a better choice FJP polishing owing to the symmetric TIF of the polished zone compared to the oblique impingement. It is also observed that at lower stand-off distance (less than $10mm$), the shape of TIF was ‘W-shaped’ which is not desirable for achieving higher material removal rate as well as to achieve nano-scaled surface finish efficiently. For transforming from ‘W-shaped’ to ‘U-shaped’, the stand-off distance should be increased between $24mm$ to $36mm$ for ductile

materials as suggested by Wang et. al [10]. But at the higher stand-off distance beyond $20mm$, the CFD solver does not converge. Thus, in the present work, we conducted extensive

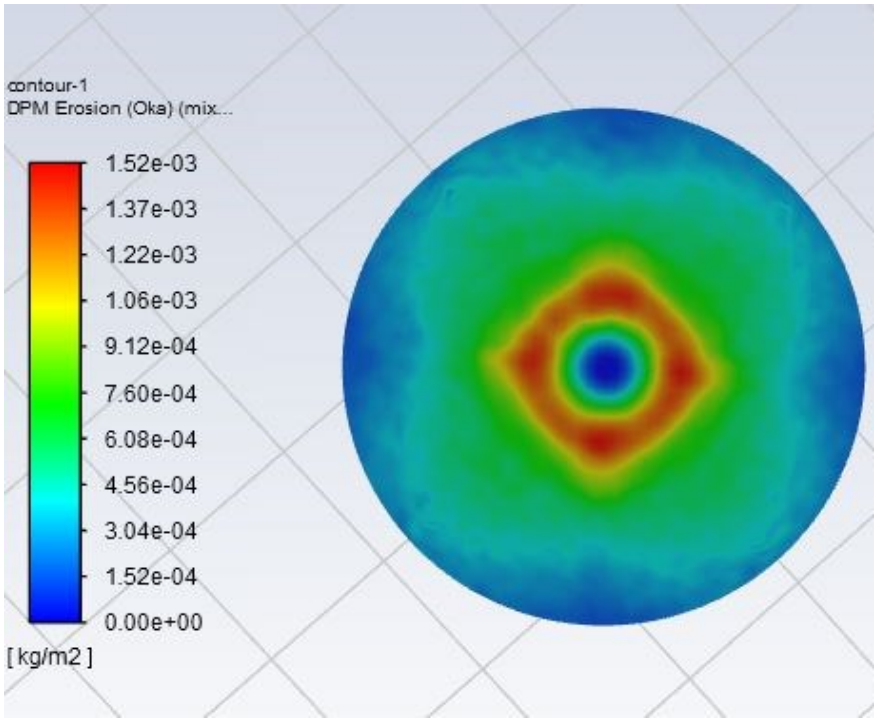

(a)

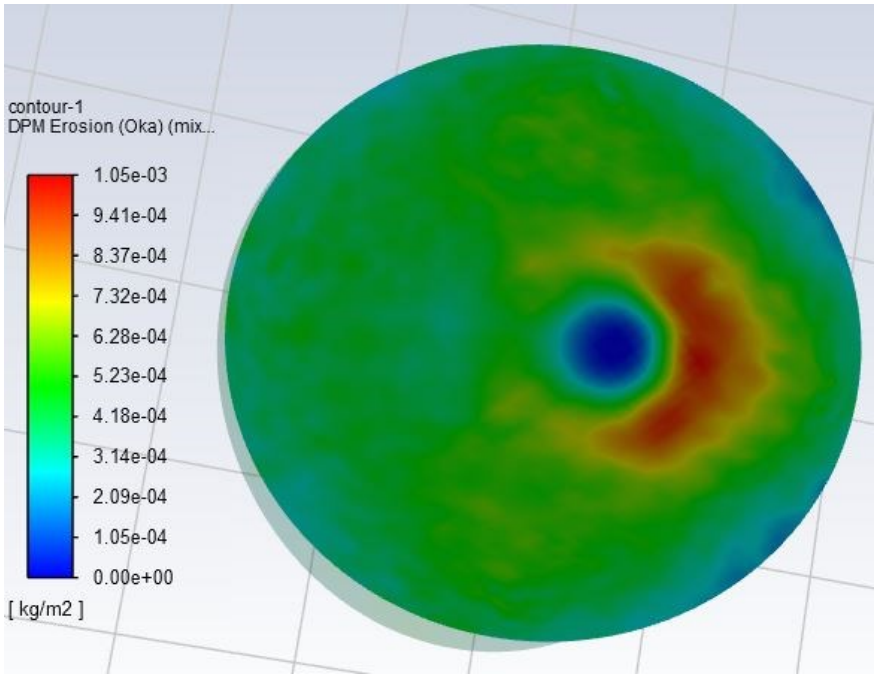

(b)

Figure 3.13: Simulation results of erosion profiles on target surface at, (a) vertical impingement and (b) oblique impingement.

experimental analysis of FJP polishing at stand-off distances from $24mm$ to $36mm$ on the Monel-400 and AISI H13 steel for rotary and non-rotary fluid-jet.

3.11 Closure

The present chapter gave the details of design of customized 3D printed FJP tool, selection of the workpiece material, details of the developed experimental set-up, characterization/measurement procedure and the range of the FJP parameters used for the DOE study. Also, the CFD simulation were performed for the basic understanding of material removal profile at lower stand-off distance on Monel 400 (NiCu alloy) workpiece surface to evaluate the material removal profile or TIF, pressure and velocity contours onto the substrate surface. The CFD study could not be performed for higher stand-off distances, thus extensive experimental studies were conducted for investigating the effect of various FJP parameters (within the parameter ranges listed in Table 3.1) for the optimization of the surface finish and enhance the process efficiency in polishing the Monel-400 and AISI H13 steel for the stationary and axisymmetric rotation of the fluid-jet.

The chapter 4 presents the parametric study for the optimization of the surface finish in FJP process for Monel-400 is presented for non-rotary and rotary FJP tool. In the chapter 5 and 6 the detailed discussion about the parametric study for the optimization of the surface finish in FJP process for AISI H13 die steel is presented for non-rotary and rotary FJP tool respectively.

Chapter 4
Fluid jet polishing of NiCu alloy using a single nozzle tool

In FJP process, the stand-off distance plays an important role and influences the vertical as well as horizontal component of the particle velocity in the shear zone which in turn affects the shape of the tool influence function (TIF) zone. As discussed in chapter 3, in this work, experimental investigations have been made to study the effect of higher stand-off distance (from $24mm$ to $36mm$) along with effect of variation in the pressure of the abrasive fluid-jet, and the polishing time in order to improve the surface finish of tool influence function (TIF) zone in polishing NiCu alloy (Monel-400) die material using FJP process.

4.1 Design of experiment

The RSM methodology has been used with three variables having five levels to determine the optimal process parameters, namely: jet pressure, stand-off distance and polishing time, as shown in Table 4.1, to achieve the optimized $\% \Delta R_a$ on the Monel-400 optical die material. RSM is a set of advanced design of experiments (DOE) technique that helps to better understand and optimize response [51]. The RSM methodology provides the central repetition of control parameters with ensuring the closeness to the developed model.

Table 4.1: Control factors and their levels in CCD design of experiment.

S. No.	Factors	Levels				
		1	**2**	**3**	**4**	**5**
1.	Pressure, P (bar)	4	6	8	10	12
2.	Stand-off distance, D (mm)	28	30	32	34	36
3.	Polishing time, T (sec)	90	120	150	180	210

The experimentation range of three selected process parameters was evaluated from the literature [4,5,6,10,19,20] and initial experimental trials. Table 4.2 shows the values of the fixed parameters used during the experimental analysis.

Table 4.2: Fixed parameters in CCD design of experiment.

S. No.	Parameters	Value
1.	Impact angle (α)	90
2.	Abrasive material	Silicon carbide (SiC)
3.	Slurry concentration (Weight, %)	6
4.	Abrasive mesh size	4000
5.	Workpiece material	MONEL-400
6.	Nozzle diameter	1.0 mm

There are mainly three methods which are used for modelling and optimization i.e., Response Surface Methodology (RSM), Taguchi method and one factor at a time (OFAT). Authors have used RSM in place of Taguchi method and one factor OFAT methodology for selection of levels. This is because the numbers of levels for process parameters are limited in this work, therefore, these methodologies may require more experimental runs for same precision as of RSM. Also, they cannot provide interaction estimation between the independent variables and can also miss optimal settings of the factors. However, RSM determine good interaction estimation among independent variables, repeatability of the experimental data is more and also provide optimal results.

Table 4.3: Experimental combinations and their responses.

Exp. No.	P (bar)	D (mm)	T (sec)	Experimental results for surface roughness (nm)					Predicted % ΔR_a Eq. (4.2)
				X_1	X_2	X_3	Average roughness	Experimental % ΔR_a Eq. (4.1)	
1	6	30	120	200	190	200	197	34	35.90
2	10	30	180	130	110	120	120	60	64.65
3	8	32	150	100	100	110	103	66	64.38
4	8	36	150	110	110	120	113	62	60.03
5	6	30	180	160	180	170	170	43	43.77
6	6	34	180	140	130	140	136	55	60.90
7	8	32	150	100	100	110	103	66	64.38
8	8	32	150	110	110	100	106	65	64.38
9	8	32	90	180	160	170	170	43	44.78
10	8	28	150	170	170	170	170	43	42.28
11	12	32	150	110	100	120	110	64	63.28
12	10	34	180	100	110	110	106	65	65.27
13	4	32	150	190	170	180	180	40	38.03
14	6	34	120	130	140	140	136	55	53.02
15	8	32	210	110	100	110	106	65	60.53
16	10	30	120	120	130	110	120	60	56.77
17	8	32	150	130	120	130	126	58	64.38
18	8	32	150	100	110	100	103	66	64.38
19	10	34	120	140	140	130	136	55	57.40
20	8	32	150	100	100	90	96	68	64.38

The Central Composite Design (CCD) method is used to develop an experiment plan for three process parameters and five levels with 20 experiments as shown in the Table 4.3. CCD is an experimental design, useful in RSM for building a second order (quadratic) model for the response variable without the need to use a complete three-level factorial experiment. CCD is

a common method which is based on a factorial design and it adds central points as well as axial points known as star points. CCD examines each factor on three levels and consequently enables the estimation of the quadratic terms. CCD can fit a full quadratic equation and mostly applies when the design plan calls for sequential experimentation due to which these designs can contain information from a correctly planned factorial experiment. A total of 20 experiments were conducted on Monel-400 plate of $50mm \times 50mm \times 6mm$ size and polished spots obtained for the stationary fluid jet (called tool influence function TIF) obtained are shown in Figure 4.1. The trails have been carried out by changing the stand-off distance and polishing time for a constant pressure with a offset span of $8mm$ between each consecutive trial.

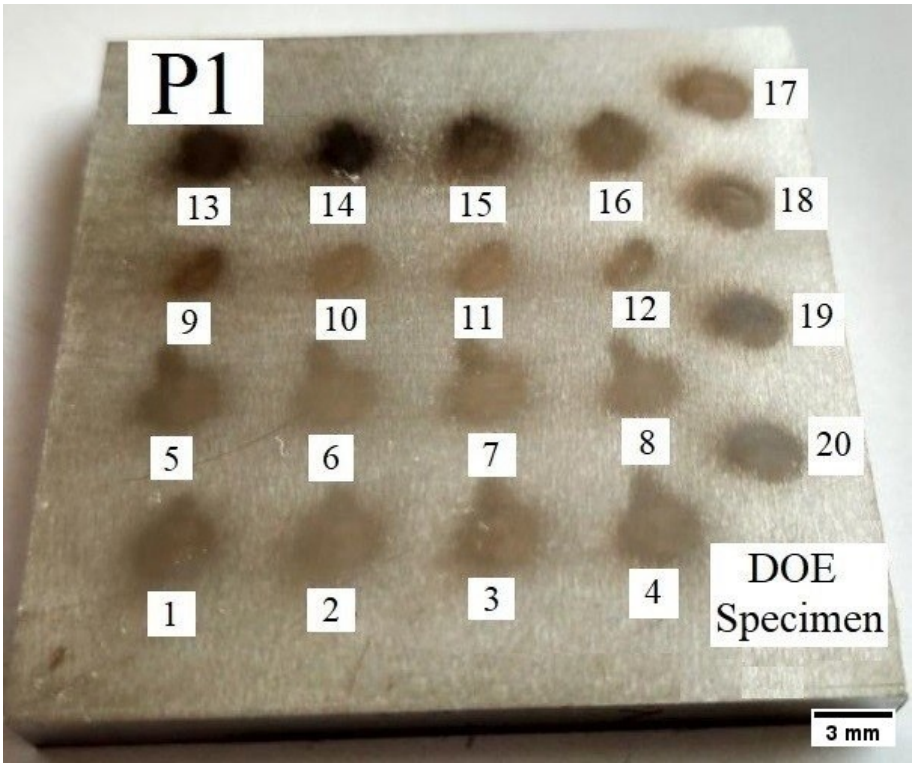

Figure 4.1 Final finished plate P1.

The surface roughness values were measured on each polished spot (TIF) at three different locations and their average values are shown in Table 4.3. The surface roughness (R_a) values were measured using SJ-400 Mitutoyo surface roughness profilometer with $0.25mm$ cut-off length with a precision of $0.001\mu m$. The percentage change in surface roughness ($\% \Delta R_a$) after polishing was calculated using Equation (4.1).

$$\% \Delta R_a = \frac{\text{Initial average surface roughness} - \text{final average surface roughness}}{\text{Initial avwerage surface roughness}} \times 100 \quad (4.1)$$

A second order regression equation was developed using the obtained experimental results. From ANOVA tables shown in Table 4.4, the non-significant terms were eliminated with the F value criteria while the significant terms were considered at 95% significance level.
Equation (4.2) shows the regression equation for the developed model.

$$\% \Delta R_a = -1290.30 + 49.89P + 63.38D + 1.11T - 0.86P^2 - 0.83D^2 - 0.0033T^2 - 1.03PD \quad (4.2)$$

Table 4.3 shows the value of the predicted $\% \Delta R_a$ given by Equation (4.2). It is evident from Table 4.3 that there is not much variation observed between the predicted and the experimental values over the entire range of the study. Also, the R^2 value for the regression model is 91.53%, R^2-Adj (adjusted R^2) is 86.60%, and the predicted R^2 is 70.65%, which are within the good agreement.

Table 4.4: ANOVA analysis for percentage change in surface roughness ($\% \Delta R_a$).

Source	Sum of squares	Degree of freedom	Mean square	F-value	Prob > F		% contribution
Model	1889.78	7	269.97	18.54	< 0.0001	Significant	
P	637.56	1	637.56	43.78	< 0.0001		29.18
D	315.06	1	315.06	21.63	0.0006		14.42
T	248.06	1	248.06	17.03	0.0014		11.35
P^2	296.12	1	296.12	20.33	0.0007		13.55
D^2	274.94	1	274.94	18.88	0.0010		12.58
T^2	216.12	1	216.12	14.84	0.0023		9.89
PD	136.13	1	136.13	9.35	0.0099		6.23
Residual	174.77	12	14.56				
Lack of Fit	113.93	7	16.28	1.34	0.3871	Not significant	
Pure Error	60.83	5	12.17				2.78
Total	**2064.55**	**19**	**108.66**				

4.2 Results and discussion

4.2.1 The effect of pressure and stand-off distance on Monel-400 surface roughness

The plots in Figure 4.2(a) and (b) shows the simultaneous effect of pressure (P) and stand-off distance (D) on $\% \Delta R_a$ at polishing time $T = 150sec$. It is clear from Figure 4.2(a) and (b) that as the fluid pressure increases from $4bar$ to $12bar$, there is an increase in $\% \Delta R_a$ value for the stand-off distance from $28mm$ to $32mm$. This is attributed to the reason that the kinetic energy of the abrasive particles for this pressure range and the stand-off distance is just sufficient for removing the material at a rate which is able to provide a better surface finish. As seen from the contour plot, Figure 4.2(b), the $\% \Delta R_a$ value is found to be in the highest range (more than

67%) corresponding to the pressure and the stand-off values near to $10bar$ and $32mm$, respectively.

For the value of stand-off distance beyond $32mm$, the % ΔR_a value starts to fall for the entire pressure range. This reduction in the % ΔR_a value is due to the fact that the simultaneous increase in slurry pressure and stand-off distance, increases the material removal rate (MRR) in the TIF zone. The increase in MRR is achieved because of the increase in the kinetic energy of the abrasive particles which strikes the workpiece surface with higher impact energy. At the same time, the increase in stand-off distance makes the slurry-jet unstable along with the randomization of the abrasive particles, which leads to the poor surface finish.

The polishing time was taken as 150 sec as it was a mid-value of the different selected levels to visualize the effect of process parameters in the entire range. The recommended value of time for such studies in the literature is mentioned as 180 seconds for polishing of non-ferrous optical die materials, but we have examined the effect of polishing time for higher stand of distances and have found that the time period of 170 seconds is the optimum value over a range of 90 seconds to 210 seconds with a step of 30 seconds.

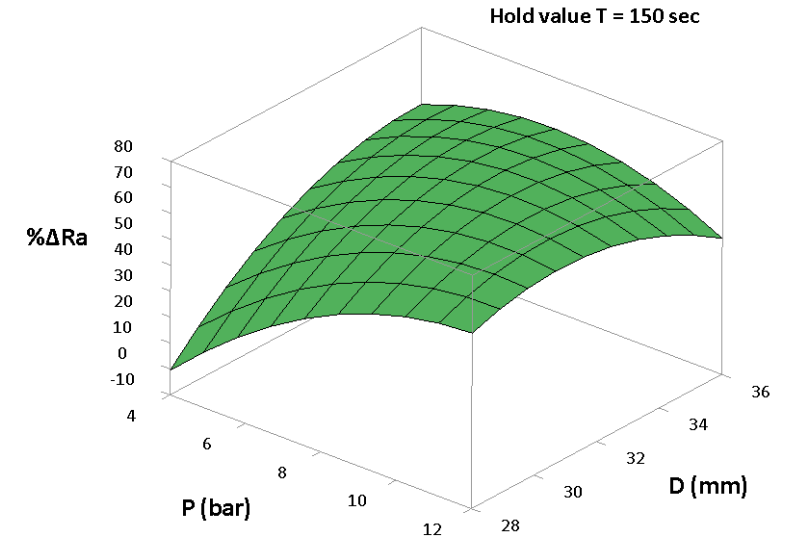

(a)

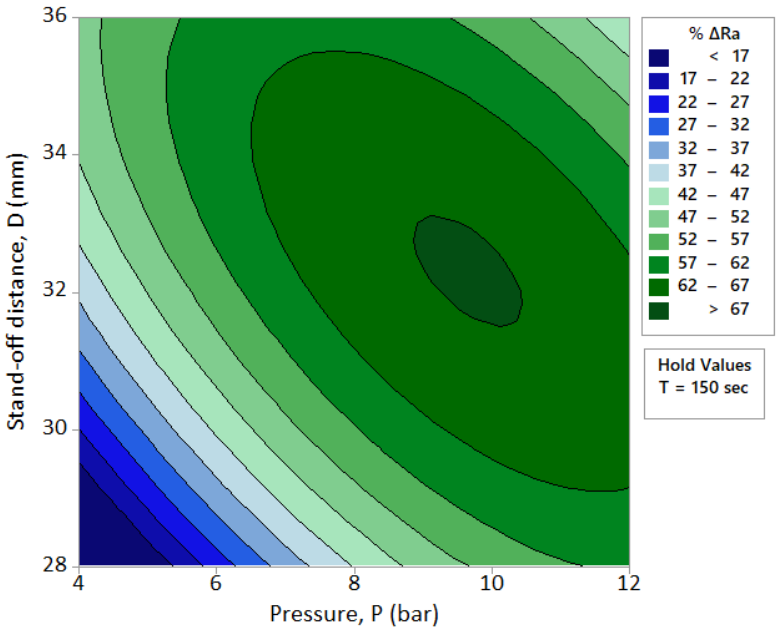

(b)

Figure 4.2: (a) Surface plot and, (b) contour plot showing variation of % ΔR_a with P and D at $T = 150\ sec$.

The fringes observed in the contour plot, clearly indicates that the kinetic energy of the abrasive particles plays an important role for achieving consistent amount of MRR to generate smooth surface finish as shown in Figure 4.2(b). The maximum kinetic energy of the impinging particles for achieving a desired range of $\%\,\Delta R_a$ can be achieved by selecting suitable combinations of process parameters, but the best performance of the FJP process was obtained near $10bar$ of pressure and $32mm$ of stand-off distance.

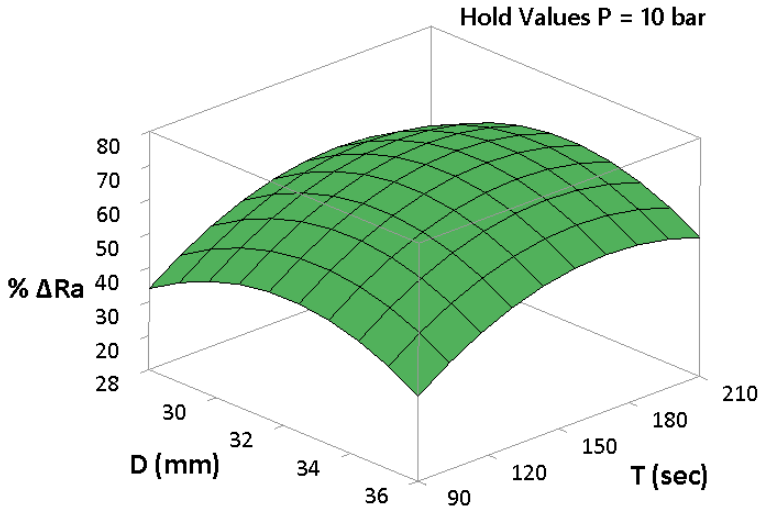

(a)

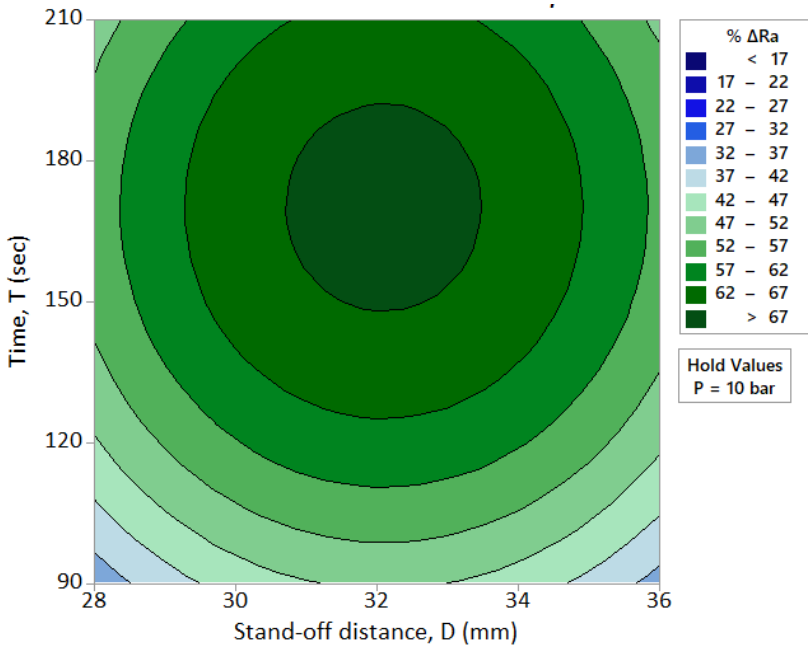

(b)

Figure 4.3: Variation in percentage change in surface roughness (% ΔR_a) at pressure $P = 10\ bar$ with respect to stand-off distance, D and time, T as (a) surface plot and (b) contour plot

4.2.2 The effect of polishing time and stand-off distance on Monel-400 surface roughness

The simultaneous effect of polishing time (T) and stand-off distance (D) on % ΔR_a is shown in Figure 4.3. It is clearly observed that the % ΔR_a rises with the increase in polishing time up to a certain value between $150sec$ to $180sec$, beyond which the % ΔR_a starts to decline. This trend is consistent for all the pressure levels from $4bar$ to $12bar$. Also, the trend for % ΔR_a shows that the slurry pressure of $10bar$ is able to generate the highest surface finish for the entire range of polishing time from $90sec$ to $210sec$. The decline in % ΔR_a at higher polishing time was due to over polishing as indicated by the parallel/offset curves corresponding to different pressure levels.

To explore the effect of stand-off distance and the polishing time, for best observed polishing pressure of $10bar$, the interaction of these two parameters were plotted using surface and the contour plots as shown in Figure 4.3. It is clear from Figure 4.3(a) and (b) that the maximum % ΔR_a is observed at stand-off distance of $32mm$ for the time period between $150sec$ to $180sec$. The concentric fringes of the contour plot in Figure 4.3(b) indicate that a particular target level of % ΔR_a can be achieved by suitable choice of stand-off distance and polishing time, out of several possible combinations.

4.2.3 Optimum process parameters

The RSM methodology used in the present work represents a harmonic response of the % ΔR_a for the range of three process parameters, P, D and T. The optimal values of % ΔR_a = 68.66 % is obtained from the developed regression model at pressure, stand-off distance and time of $9.66bar$, $32.3mm$ and $170sec$, respectively which are shown in Figure 4.4.

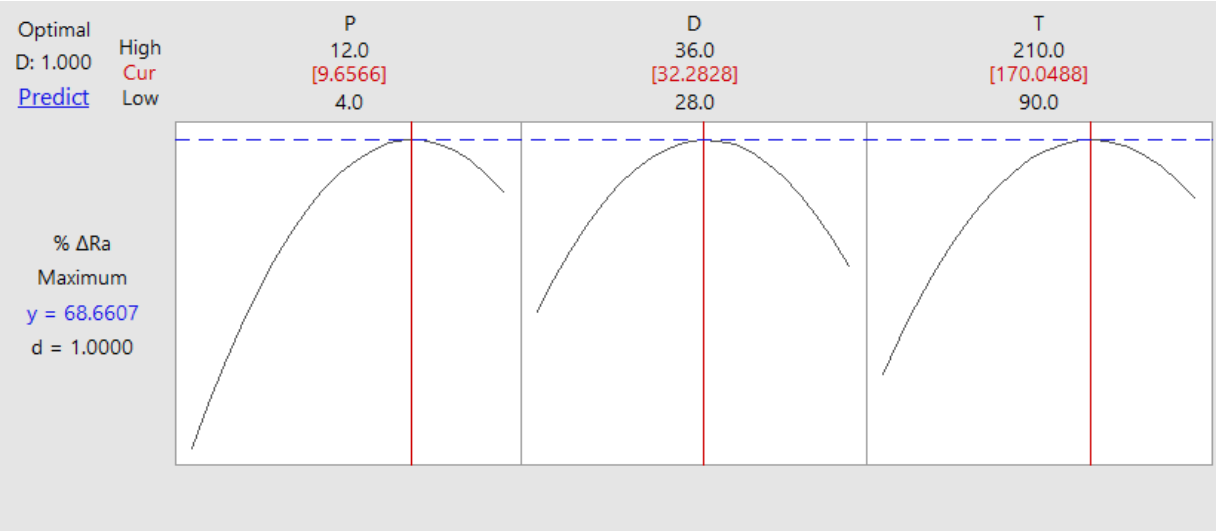

Figure 4.4: Optimized values of control parameters, *P*, *D* and *T*, obtained from the CCD study.

Figure 4.5(a) represents the initial average surface roughness of the Monel-400 plate and Figure 4.5(b) shows the achieved average surface roughness of $90nm$ from the FJP process. It is clearly evident from the roughness profile that there is reduction in the peaks to valleys as compared to the initial surface.

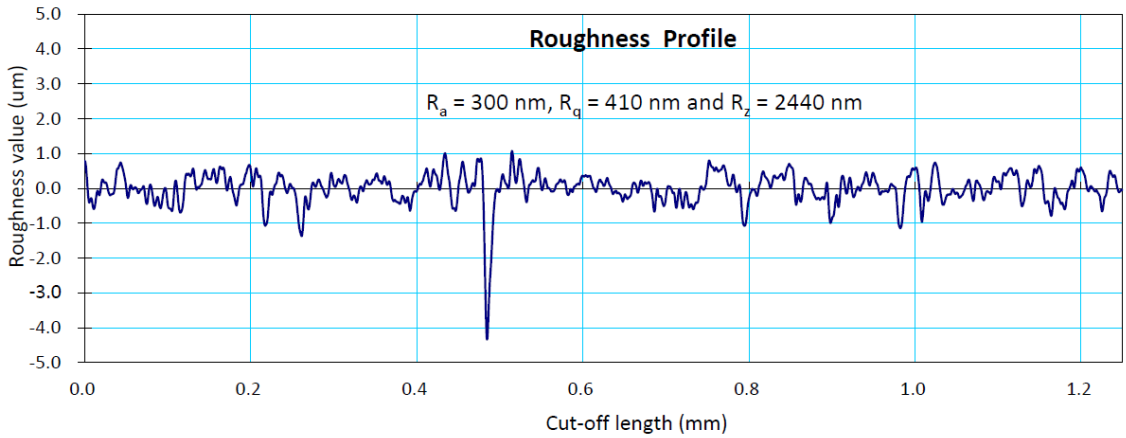

(a)

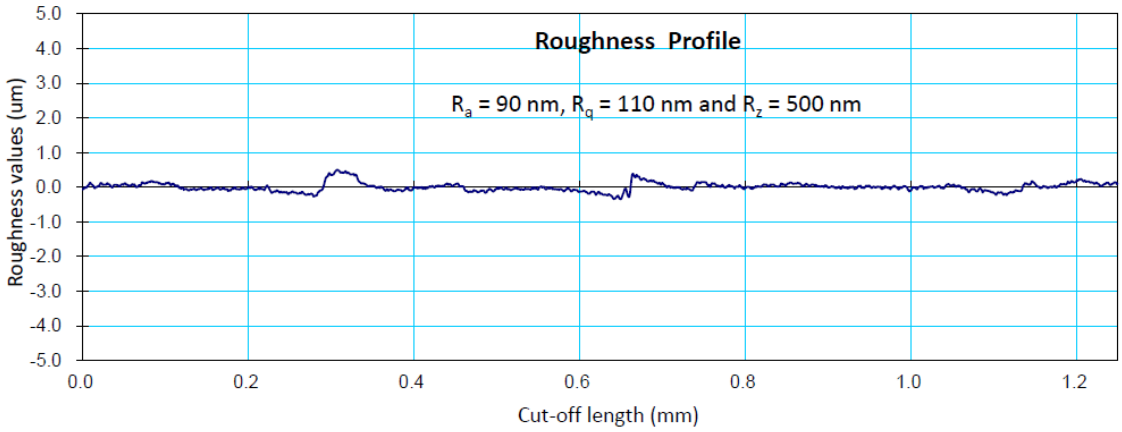

(b)

Figure 4.5: Surface roughness profiles for (a) initial surface and (b) final surface at $P = 9.6\ bar$, $D = 32.2\ mm$ and $T = 170\ sec$.

4.2.4 Characterization

The hardness of the Monel-400 material is also measured with the micro-hardness tester (Mitutoyo HM-210 model). In this method, a conical diamond indenter was used to permanently deform the surface in the form of impression/indentation. The diagonals of this impression in the form of conical diamond shape/deformed material were properly measured to calculate the value of microhardness. The values of micro-hardness were measured at ten different locations on the initial surface and FJP polished surface of Monel-400 specimen and the average of the measured values were taken. The average hardness values before and after polishing was found to be $234.6HV$ and $237.4HV$, respectively. The results of the test revealed that the hardness of the material increases marginally after the FJP polishing process. It was due to the fact that polished surface was relatively smooth and particle impact caused hardening effect on to the substrate surface of Monel-400. Also, embedment of SiC abrasive particles caused a marginal rise in the surface hardness. The surface characterization of the polished spots on workpiece material were analysed and comparison was done with the initial workpiece surface using SEM images which are shown in Figure 4.6 below.

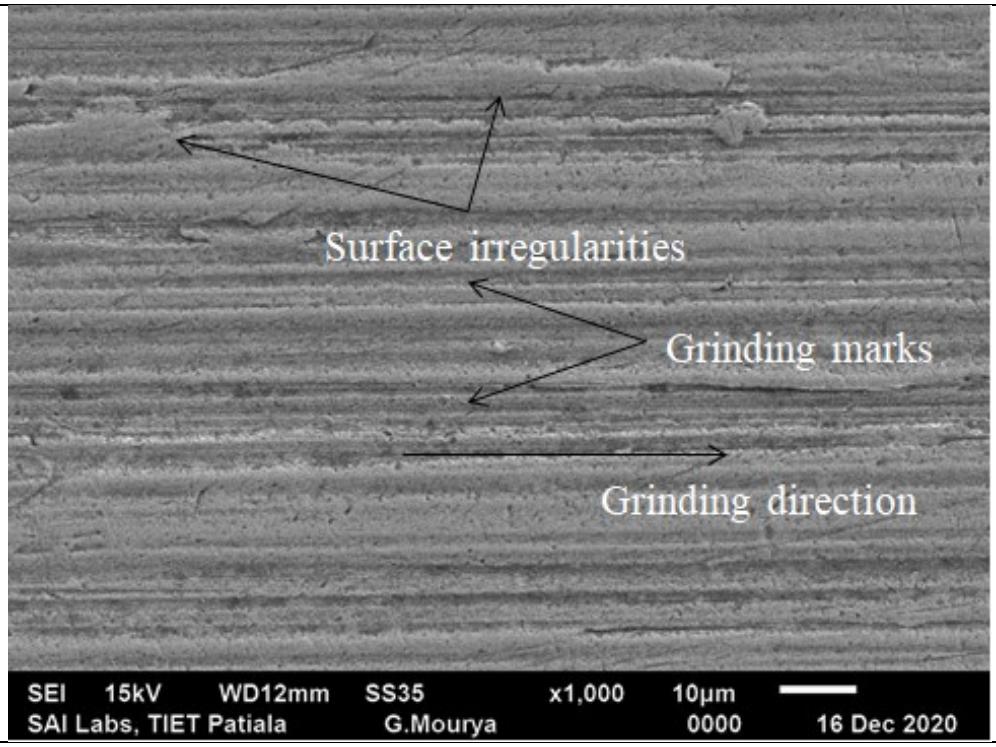

(a)

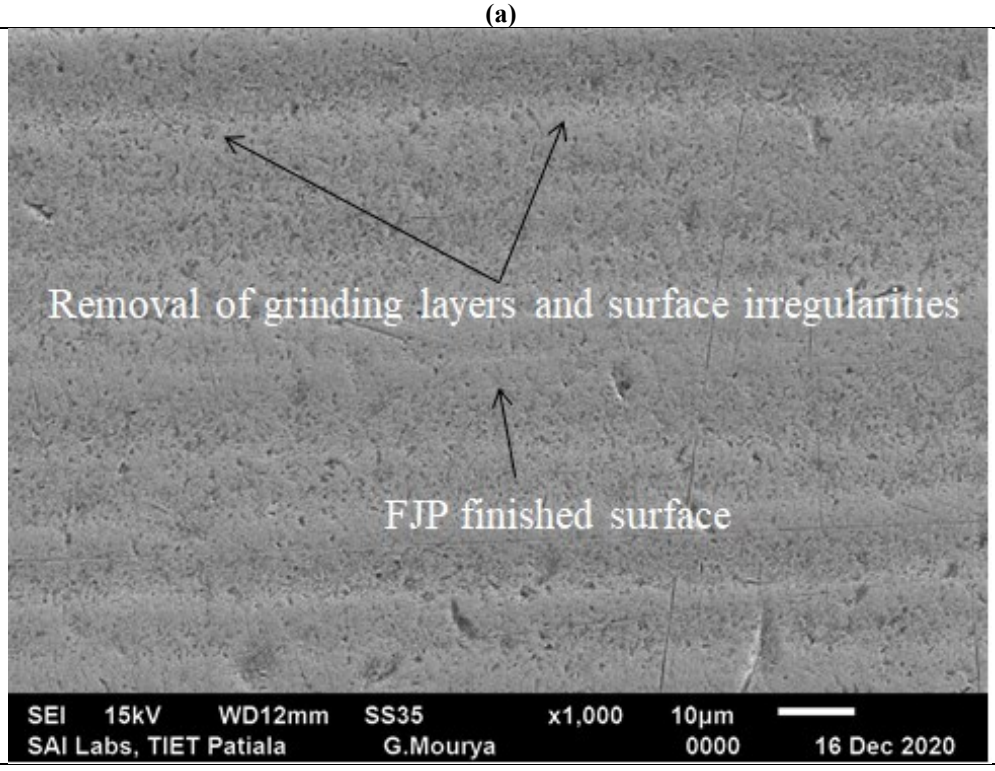

(b)

Figure 4.6 Surface morphology of (a) initial surface and (b) final FJP finished surface at $P = 9.6\ bar$, $D = 32.2\ mm$ and $T = 170\ sec$.

The Figure 4.6(a) and (b) shows the SEM images of both the initial surface and the polished surface, respectively. From Figure 4.6(a), the existence of the cusps or voids as well as uneven surface irregularities into the initial surface can be seen. These defects were generated during initial pre-processing polishing process that left the scratch marks on workpiece surface.

However, as shown in Figure 4.6(b), after FJP process the surface defects and major irregularities on the surface were controlled and a nano-scale surface finish was achieved in the TIF zone.

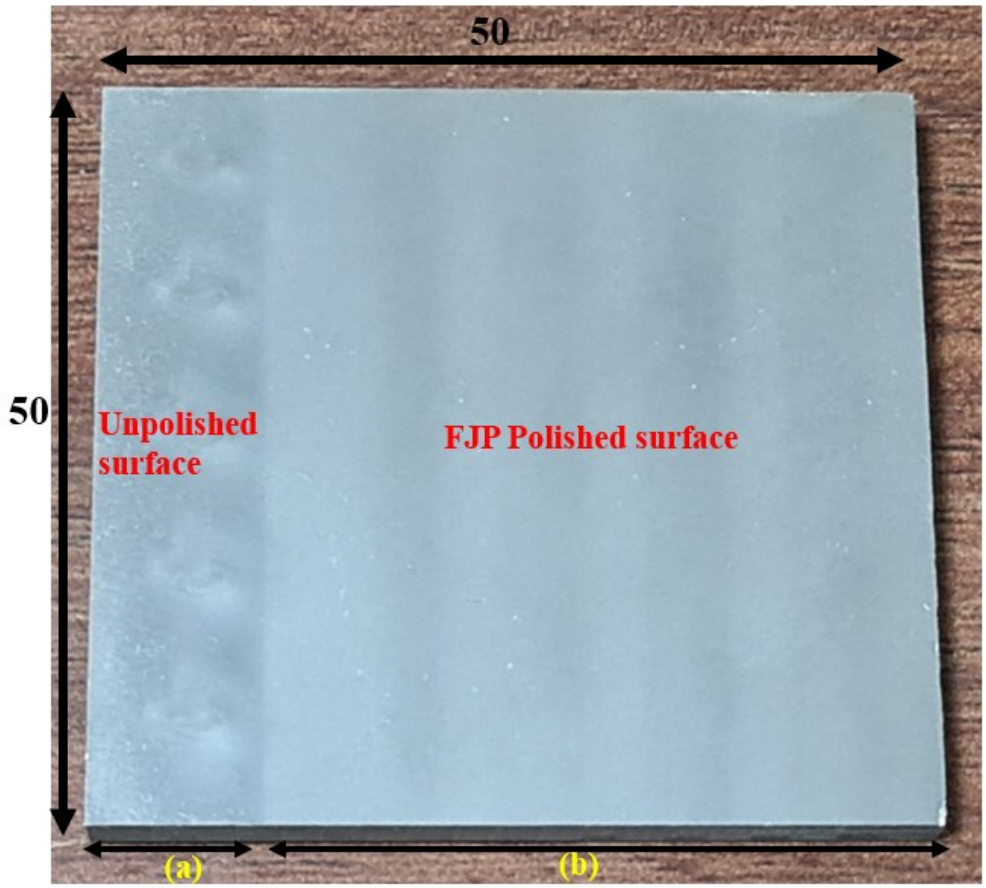

Figure 4.7: Surface image of, (a) an unpolished area and (b) FJP polished area on the Monel-400 surface. The area of the test specimen surface being 50mmx50mm.

4.3 Study of surface polishing with non-rotary fluid-jet of Monel-400 specimen

Further, a square flat plate of Monel-400 die material of dimension $50mm \times 50mm$ of initial average surface roughness of $300nm$ (initial R_a for specimen surface shown in Figure 4.7, was polished on an area of $40mm \times 50mm$ upto 16 sets of raster polishing passes one after other at constant feed rate of $20mm/min$ [5, 57] using optimum process parameters determined in the above study. The parameters used for polishing in each raster toolpath set are given in Table 4.5. The sample surface area of 40mm×50mm was polished using the raster toolpath of 50mm feed-forward length for each set of toolpath with 2.0mm side-step distance between the polishing passes making the total toolpath length of 1050mm. The toolpath length of 1050mm in each set of toolpath is given by (20+1) number of feed-forward polishing passes of 50mm

feedforward traverse to cover the span of 40mm for covering the entire targeted specimen surface area.

Table 4.5: Optimum FJP Parameters used for polishing Monel-400 sample.

S. No.	Parameter	Magnitude
1.	Pressure, P (bar)	9.6
2.	Stand-off distance, D (mm)	32.2
3.	Feed rate, F (mm/min)	20
4.	Travel path, L (mm)	50
5.	X-spacing (mm)	15
6.	Y-spacing (mm)	15
7.	Polished region, (mm^2)	40×50
8.	Polishing toolpath Pattern	Raster with 2.0mm side-step
9.	Number of passes	10

After polishing the specimen surface each time, with a set of two surface polishing passes, the surface roughness was measured which was found to be lower than the previous stage until the 10^{th} polishing pass as shown in Table 4.6. During the 10^{th} pass the surface roughness was found to be the best as $80nm$ and $130nm$ along the direction of polishing and perpendicular to the direction of polishing which is also shown in Figure 4.8(a) and 4.8(b), respectively. It is observed that after 10^{th} pass the average surface roughness gradually increased and hence, it is concluded that the 10 number of polishing passes with a federate of $20mm/min$ are necessary to get the best possible result for a Monel-400 surface with initial average surface roughness of $300nm$.

The polishing time, T is proportional to the length of the tool path and inversely proportional to the feed rate as given by Equation (4.3).

$$T = \frac{L}{F} \tag{4.3}$$

Where, L is the length of the tool path (mm) and F is the feed rate (mm/min).

The overall time taken for polishing the $40mm \times 50mm$ area with 10 passes where each pass covers the entire surface area is given by:

$$Total\ polishing\ Time$$
$$= (Toolpath\ length\ per\ pass \times Number\ of\ passes)/Feed\ rate$$
$$= (1050mm \times 10)/(20mm/min) = 525min.$$

Table 4.6: Average surface roughness obtained for non-rotary single-nozzle fluid-jet polishing of Monel-400 test surface of initial average surface roughness R_a of $300nm$.

S. No.	Number of passes	Total Tool path length (in mm)	Polishing time (in min) at feed rate $20mm/min$	Surface roughness, R_a after polishing (nm)	Percentage change in surface roughness (% ΔR_a) Eq. (4.1)
1	2	$1050 \times 2 = 2100$	105	270	10
2	4	$1050 \times 4 = 4200$	210	230	23.3
3	6	$1050 \times 6 = 6300$	315	180	40
4	8	$1050 \times 8 = 8400$	420	150	50
5	10	$1050 \times 10 = 10500$	**525**	**130**	**56.7**
6	12	$1050 \times 12 = 12600$	630	170	43.3
7	14	$1050 \times 14 = 14700$	735	210	30
8	16	$1050 \times 16 = 16800$	840	280	6.7

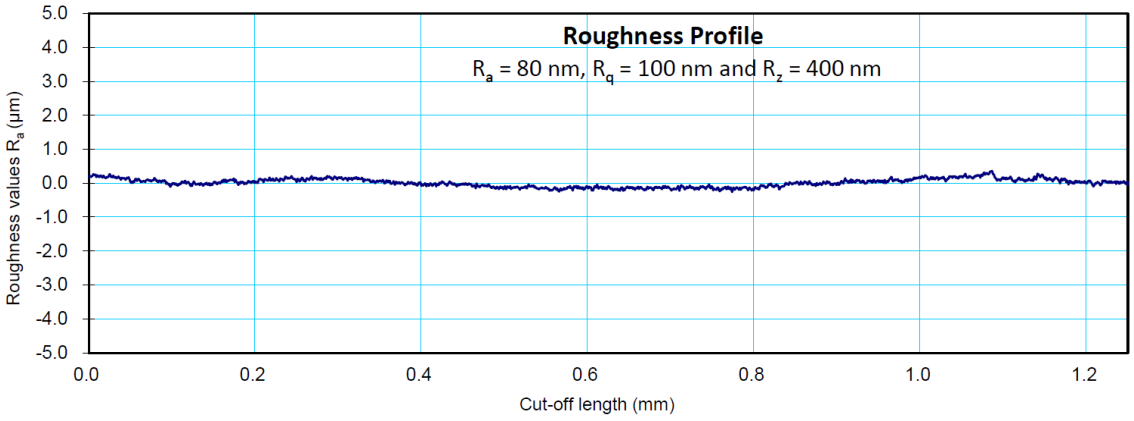

(a)

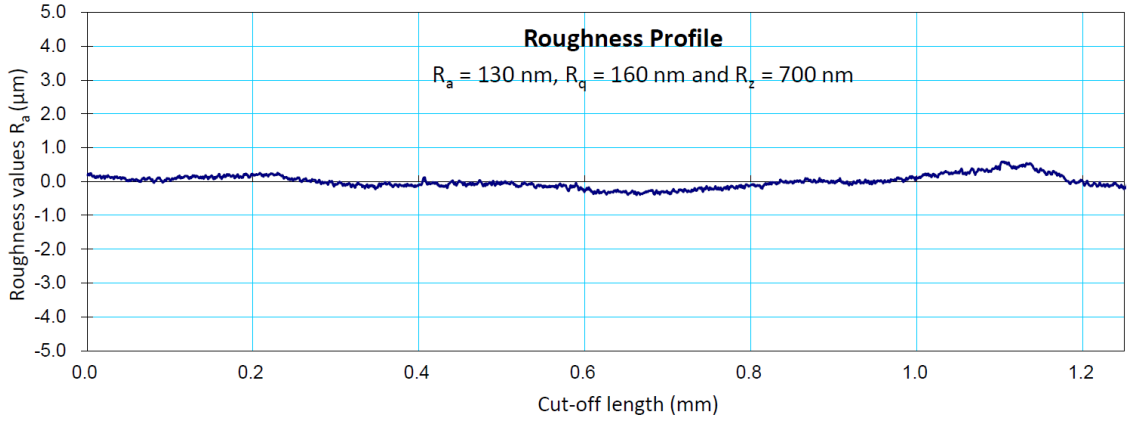

(b)

Figure 4.8: Surface roughness values (a) along the feed direction and (b) perpendicular to the feed direction of tool used for FJP polishing.

At the feed rate of $20mm/min$, the percentage change in surface roughness (ΔR_a) values increases. It is due to the reason that the velocity was increased in the throat area of the nozzle and becomes maximum when slurry jets moves out of the nozzle. So, abrasive particles strike onto the workpiece surface with the higher impact velocity. This impact velocity was further divided into normal and tangential velocities. As the abrasive particles impact the surface, their

normal component of velocity was responsible for penetration into the workpiece material, which leads to deformation wear. Whereas, the horizontal component of the velocity was responsible for cutting action of the particles. In cutting process, abrasive particles with high energy will bounce off from the workpiece surface after striking the surface and remaining abrasive particles are responsible for shearing action or chipping off material from the substrate surface which removes the peak to valley from the workpiece surface.

The reduction in surface roughness ($\% \Delta R_a$) after 10 polishing passes was observed to be 73.33% for polishing Monel-400 specimen surface, which took total time of $525 min$. Figure 4.7(a) and 4.7(b) shows the comparison between the unpolished and FJP polished surfaces of Monel-400 die material, where an average surface roughness value of $80 nm$ and $130 nm$ along the direction of polishing and perpendicular to the direction of polishing which are shown in captured surface profiles as shown in Figure 4.8(a) and 4.8(b), respectively.

4.4 Study of effect of rotation of fluid-jet on polishing of Monel-400 specimen.

The optimized FJP process parameters for single nozzle non-rotary FJP tool determined for polishing of Monel-400 has been used to extend the study further to understand the effect of rotation of the fluid-jet on the quality and efficiency of the polishing process. In this case we used the single-nozzle and the two-nozzle FJP tools as shown in Figure 3.1(a) and 3.1(b). It is known that the vertical impingement of the fluid-jet in FJP process at low stand-off distance leads to the formation of the stagnation zone and the formation of the stagnation zone can be avoided by increasing the stand-off distance. At higher stand-off distance, the TIF has the symmetric "U" formation and leads to better material removal in the central part of the TIF. The effective polishing area in FJP process can be increased by rotating the axisymmetric FJP nozzle/s about the vertical tool-axis by rotating the spindle of the 3-axis CNC vertical milling center. Also, the rotary moment of the vertical fluid-jet about the vertical tool-axis also helps suppress the stagnation of abrasive particles in the central TIF zone.

During the course of the present work, it is observed for the FJP polishing of H13 die steel with rotary FJP tool [57] that the spindle rotation of $63 rpm$ and a feed rate of $20 mm/min$ yield the best results. Thus, for the comparative study of FJP polishing on Monel-400 surface with rotary single-nozzle and rotary two-nozzles, the spindle rotation and feed rate are taken as $63 rpm$ and $20 mm/min$. The relative efficiency of rotary fluid-jet polishing with the single-nozzle

tool and the two-nozzle tools has been determined for the optimum FJP process parameters determined for Monel-400 for single-nozzle non-rotary FJP tool, as given in Table 4.8.

Table 4.7: Fluid jet polishing trial for single and double nozzle with rotary tool.

S. No.	Parameters	Value
1.	Pressure, P (bar)	9.6
2.	Stand-off distance, D (mm)	32.2
3.	Feed rate, F (mm/min)	20
4.	Spindle rotation, R (rpm)	63
5.	Travel path, L (mm)	10
6.	X-spacing (mm)	16
7.	Y-spacing (mm)	13
8.	Polishing region, (mm^2)	$8.5mmx10mm$ (except semi-circular ends)
9.	Polishing path pattern	Raster
10.	Number of passes	2, 4, 6, 8, 10, 12, 14, and 16

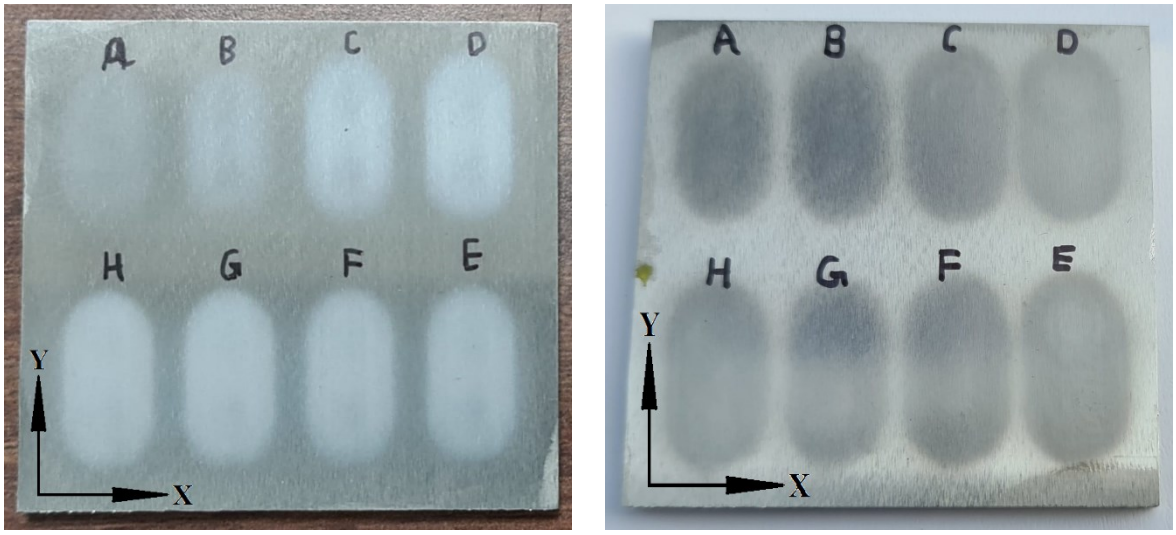

(a) **(b)**

Figure 4.9: Monel-400 surface polished with rotary vertical fluid-jet FJP Tool with, (a) single nozzle, and (b) two nozzles.

Two specimen surfaces were prepared by surface grinding on Monel-400 workpiece of sizes $52mm \times 58mm$. One of the test surfaces, with initial average surface roughness $\boldsymbol{R_a}$ of $370nm$, was polished using rotary single-nozzle rotary tool as shown in Figure 4.9(a), while the second test surface, with initial average surface roughness $\boldsymbol{R_a}$ of $380nm$, was polished using rotary two-nozzle tool as shown in Figure 4.9(b). For both the rotary FJP tools, eight different trials were conducted on the respective test surfaces of $10mm$ tool-axis traverse length with raster toolpaths (with no side-step distance between two toolpaths for each trial). The number of raster passes taken for the eight trials were for 2, 4, 6, 8, 10, 12, 14 and 16, and are shown with capital letters $\boldsymbol{A}$ to $\boldsymbol{E}$ in the Figure 4.9(a) and Figure 4.9(b).

Table 4.8: Average surface finish obtained for single-nozzle rotary fluid-jet polishing of Monel-400 test surface of initial average surface roughness R_a of $370nm$.

S. No.	Number of passes	Polishing time (in min) at feed rate $20mm/min$	Surface roughness, R_a after polishing (nm)	Percentage change in surface roughness (% ΔR_a) Eq. (4.1)
1	2	1	350	5.41
2	4	2	330	10.81
3	6	3	320	13.51
4	8	4	310	16.22
5	10	5	310	16.22
6	12	6	300	18.92
7	14	7	290	21.62
8	16	8	280	24.32

Table 4.9: Average surface finish obtained for two-nozzle rotary fluid-jet polishing of Monel-400 test surface of initial average surface roughness R_a of $380nm$.

S. No.	Number of passes	Polishing time (in min) at feed rate $20mm/min$	Surface roughness, R_a after polishing (nm)	Percentage change in surface roughness (% ΔR_a) Eq. (4.1)
1	2	1	290	23.68
2	4	2	280	26.32
3	6	3	250	34.21
4	8	4	230	39.47
5	10	5	200	47.37
6	12	6	190	50.00
7	14	7	260	31.58
8	16	8	280	26.32

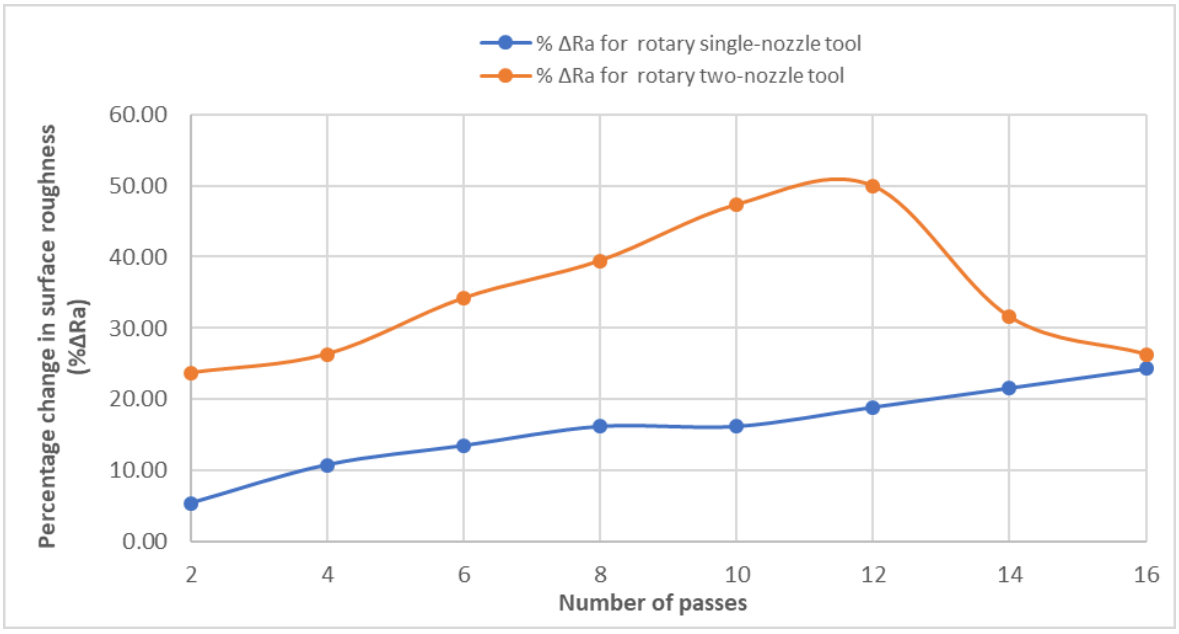

Figure 4.10: Comparison of trends for percentage change in surface roughness (%ΔR_a) for fluid-jet polishing with rotary single-nozzle and two-nozzle tool.

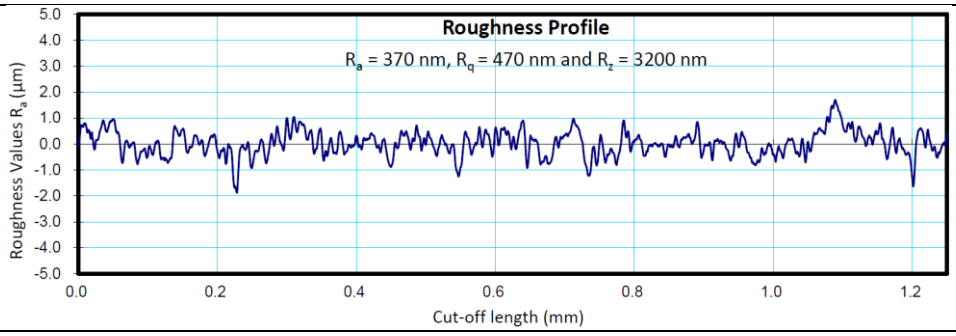

(a) Initial surface specimen of Monel-400 with $R_a = 370nm$

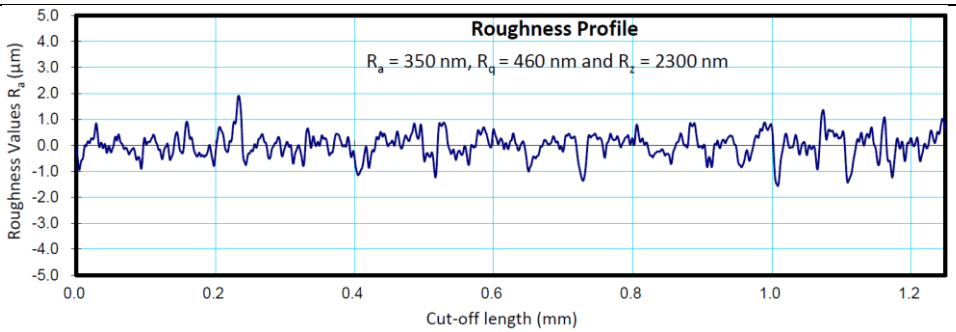

(b): Average R_a after 2 set of polishing passes shown as spot A in Figure 4.9(a)

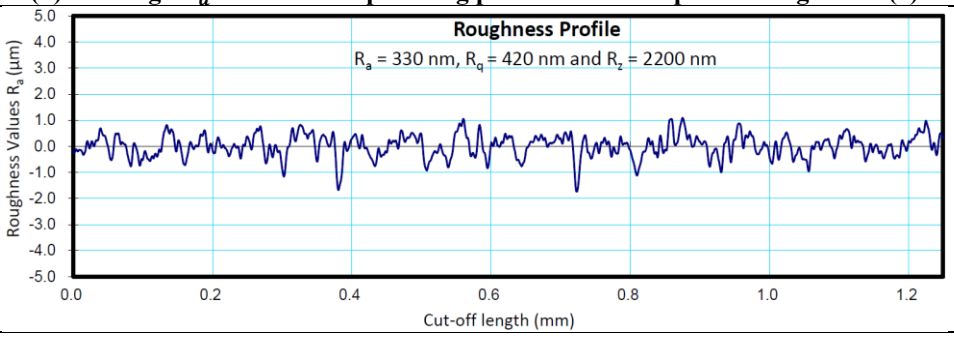

(c): Average R_a after 4 set of polishing passes shown as spot B in Figure 4.9(a)

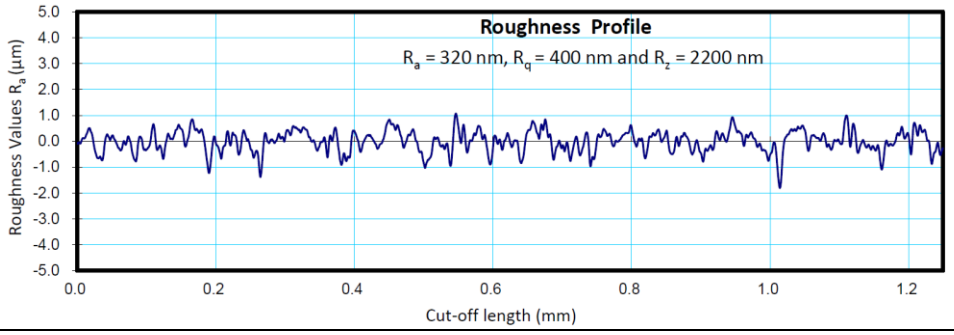

(d): Average R_a after 6 set of polishing passes shown as spot C in Figure 4.9(a)

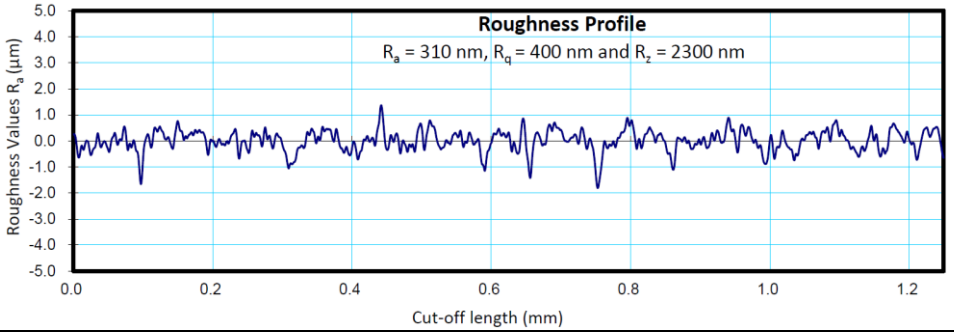

(e): Average R_a after 8 set of polishing passes shown as spot D in Figure 4.9(a)

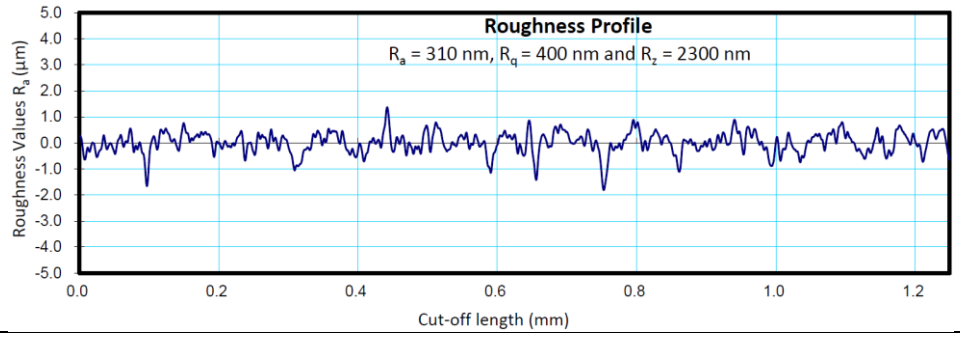

(f): Average R_a after 10 set of polishing passes shown as spot E in Figure 4.9(a)

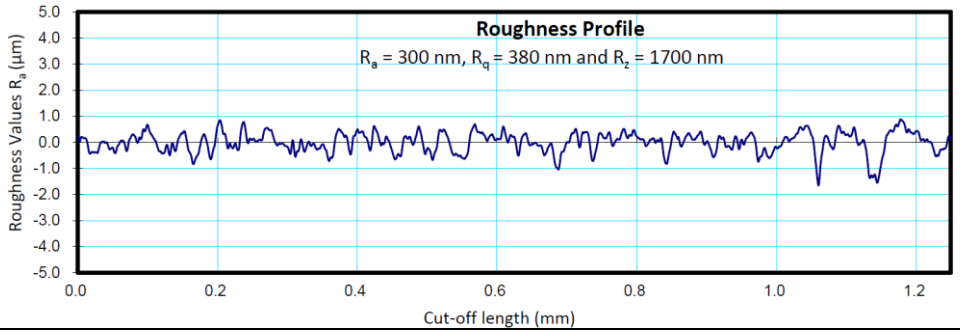

(g): Average R_a after 12 set of polishing passes shown as spot F in Figure 4.9(a)

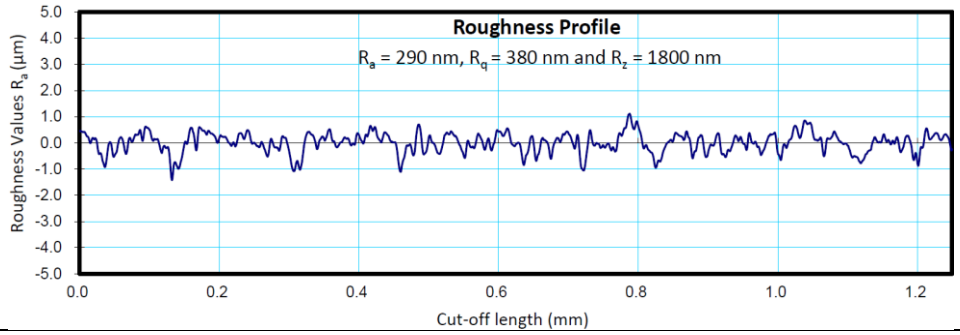

(h): Average R_a after 14 set of polishing passes shown as spot G in Figure 4.9(a)

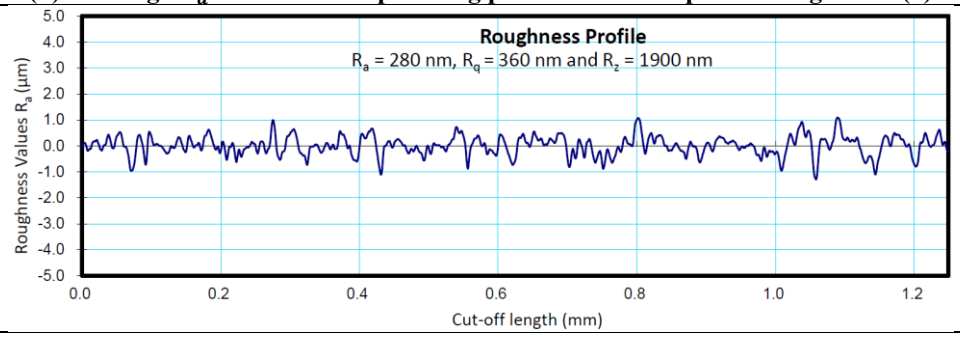

(i): Average R_a after 16 set of polishing passes shown as spot H in Figure 4.9(a)

Figure 4.11: Surface roughness profile for, (a) initial grinded Monel-400 test surface ($Ra\ 370nm$), and (b-i) test surface after FJP polishing with rotary single-nozzle tool with 2 to 16 set of surface polishing passes.

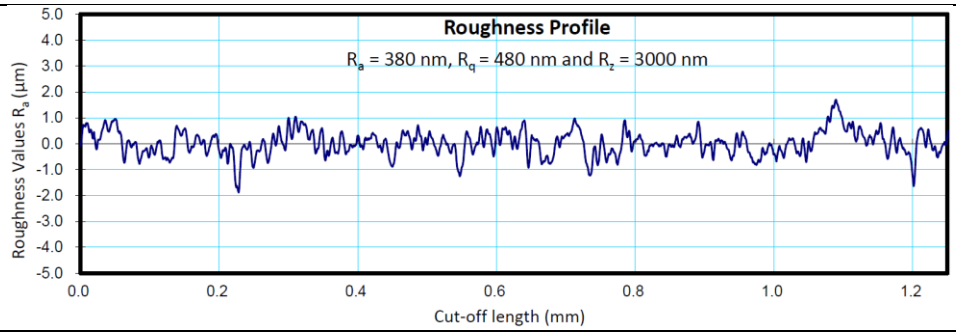

(a) Initial surface specimen of Monel-400 with $R_a = 380nm$

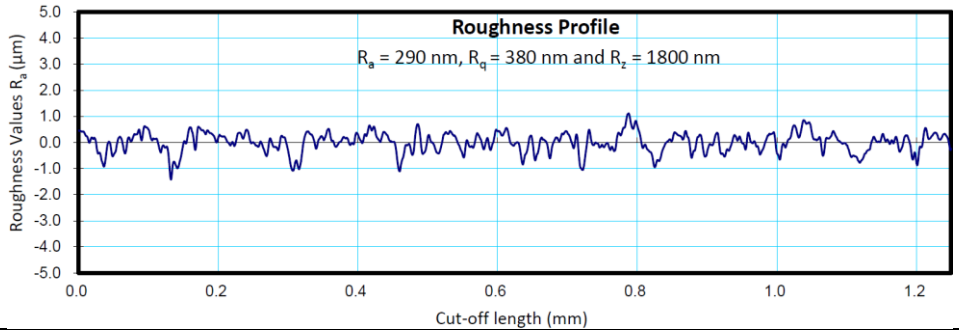

(b) Average R_a after 2 set of polishing passes shown as spot A in Figure 4.9(b)

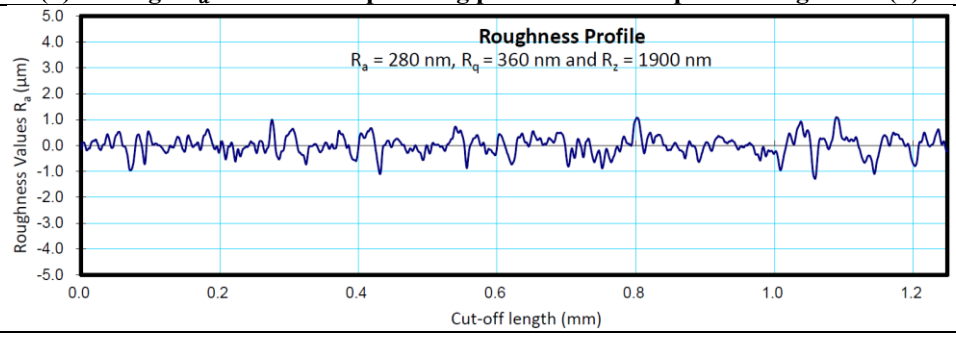

(c) Average R_a after 4 set of polishing passes shown as spot B in Figure 4.9(b)

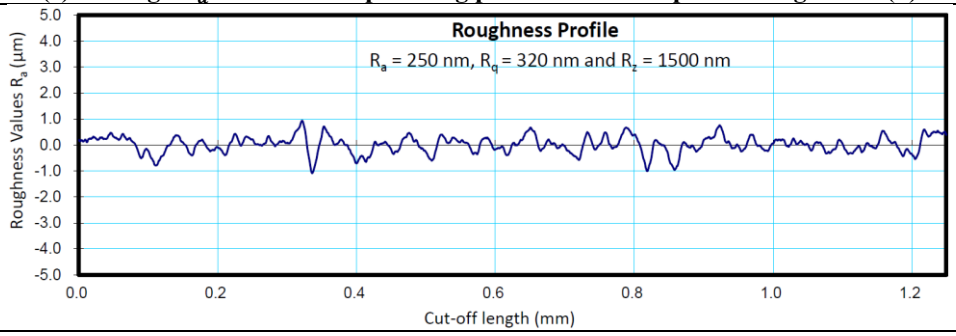

(d) Average R_a after 6 set of polishing passes shown as spot C in Figure 4.9(b)

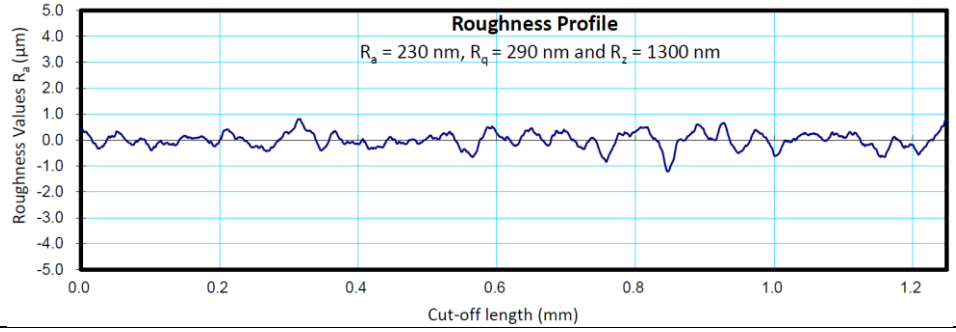

(e) Average R_a after 8 set of polishing passes shown as spot D in Figure 4.9(b)

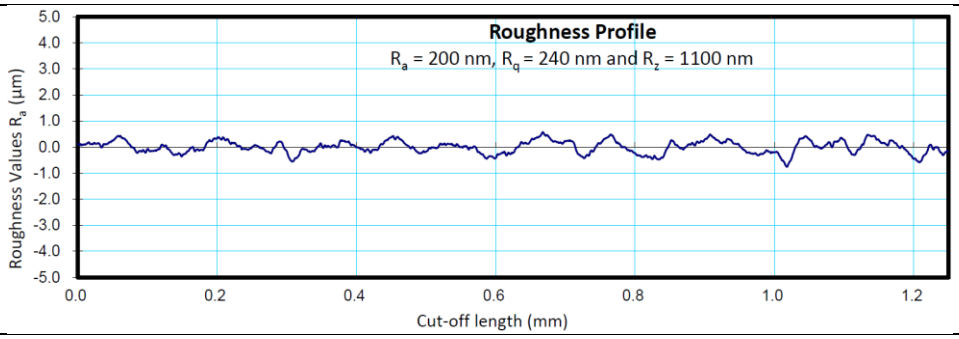

(f) Average R_a after 10 set of polishing passes shown as spot E in Figure 4.9(b)

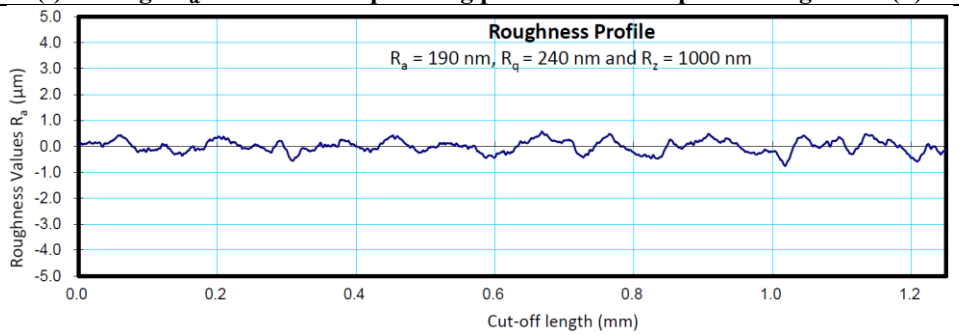

(g) Average R_a after 12 set of polishing passes shown as spot F in Figure 4.9(b)

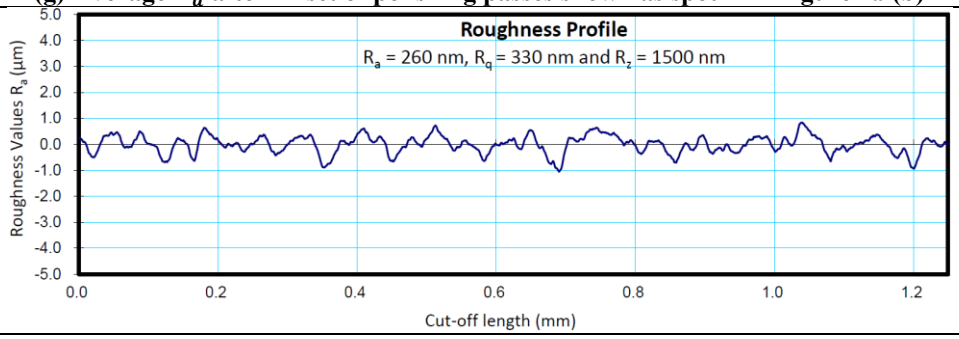

(h) Average R_a after 14 set of polishing passes shown as spot G in Figure 4.9(b)

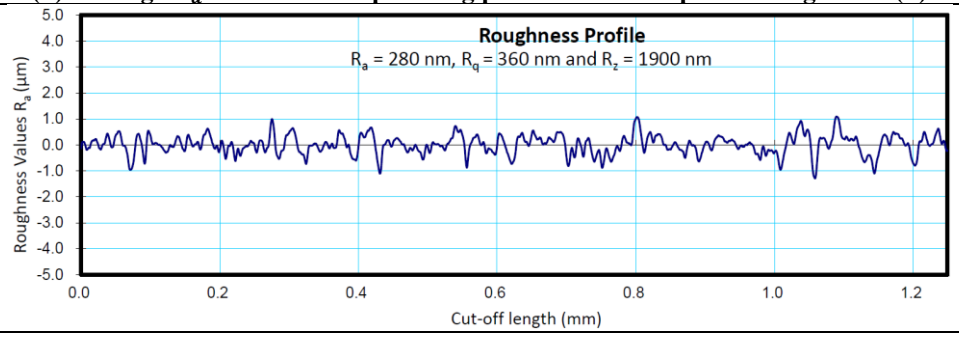

(i) Average R_a after 16 set of polishing passes shown as spot H in Figure 4.9(b)

Figure 4.12: Surface roughness profile for (a) initial grinded Monel-400 test surface ($Ra\ 380nm$), and (b-i) test surface after FJP polishing with rotary two-nozzle tool with 2 to 16 sets of polishing passes.

To get the impression for the polished areas for each of the eight trials on the two separate test surfaces (shown in Figure 4.9(a) and Figure 4.9(b), the tool-axis position are separated from each other by a distance of $16mm$ along X-axis and $13mm$ along Y-axis. The polishing conditions used in the experimentation are shown in Table 4.8. The Table 4.9 and Table 4.10 shows the average surface roughness (R_a) and the percentage difference of average surface

roughness (% $\boldsymbol{\Delta R_a}$) with respect to the initial average surface roughness of the Monel-400 test surfaces, obtained after polishing the test surfaces with single-nozzle and rotary double-nozzle rotary FJP tools for 2 polishing passes to 16 polishing passes.

It is observed from the Table 4.9 and Table 4.10, that the fluid-jet polishing performance obtained for Monel-400 test surfaces using the rotary two-nozzle tool for all polishing passes is better than the rotary single-nozzle fluid jet. In case of rotary single-nozzle fluid jet, the maximum $\%\Delta R_a$ value of 24.32% is obtained for 16 machining passes, which reduced the initial roughness of $370nm$ to $280nm$ in 8 minutes for an effective polished area of $10mm \times 8.5mm$. In case of rotary two-nozzle fluid-jet polishing, the maximum $\%\Delta R_a$ value of 50% is obtained for 12 machining passes, which reduced the initial roughness of $380nm$ to $190nm$ in just 6 minutes for the same size of the effective polished area of $10mm \times 8.5mm$.

Also, the trends for $\%\Delta R_a$ obtained for rotary single-nozzle fluid jet tool and rotary two-nozzle fluid jet tool are plotted for the 8 different set of machining passes and is shown in Figure 4.10. It is quite apparent from Figure 4.10 that the best results for rotary fluid-jet polishing is obtained when using the two-nozzle tool for all polishing passes and the best results is observed for polishing the same area as many as 12 consecutive polishing passes. Also, the difference between the maximum $\%\Delta R_a$ obtained in case of two-nozzle tool (observed for 12 passes) is as high as 24.68% compared to the maximum $\%\Delta R_a$ obtained in case of single-nozzle tool. The surface roughness profile for the grinded Monel-400 test surface ($Ra\ 370nm$), used for studying the effect of number of polishing passes with rotary single-nozzle FJP tool is shown in Figure 4.11(a), while Figure 4.11(b) shows the best surface profile ($Ra\ 280nm$) obtained for FJP polishing with rotary single-nozzle tool with 16 machining passes. Similarly, the surface roughness profile for the grinded Monel-400 test surface ($Ra\ 380nm$) used for studying effect of the number of polishing passes with rotary two-nozzle FJP tool is shown in Figure 4.12(a), while Figure 4.12(b) shows the best surface profile obtained for FJP polishing with rotary single-nozzle tool with 12 machining passes. It is also observed from the comparison of the FJP polishing results obtained from the rotary fluid-jet tools that the polishing performance (in terms of $\boldsymbol{\%\Delta R_a}$), and the process efficiency (in terms of the polishing

time required to polish a unit area) gets significantly enhanced as we increase the number of nozzles in FJP tool from single nozzle to two-nozzles.

4.5 Closure

This chapter presented the design of experiment plan developed using the CCD method for studying effect of three primary process parameters on the material removal in TIF zone and the surface finish generated in the fluid-jet polishing (FJP) of Monel-400 (NiCu) alloy for a stationary converging nozzle of 1mm diameter designed in a customized Ti64 tool. The three FJP process parameters used in the study are: pressure of the fluid-jet, stand-off distance (SoD) and the polishing time. It is found in this work that percentage reduction in surface roughness, $\% \Delta R_a$, on Monel 400 (NiCu alloy) workpiece surface was predicted at optimum values of the FJP process parameters of pressure, stand-off distance and polishing time of $9.66bar$, $32.3mm$ and $170s$, respectively.

Further a study is conducted on the effect of number of machining passes of non-rotary single nozzle on the reduction of the average surface roughness in FJP process. It is noticed in the study that for the optimized values of the three process parameters a reduction of 73.33% in the average surface roughness is possible for Monel-400 of initial average surface roughness of $300nm$. But this reduction in average surface roughness took $1025min$ on a sample surface of $40mm \times 50mm$.

Further, we studied the effect of rotation of the vertical fluid-jet on the polishing of the Monel-400 using single-nozzle and two-nozzle FJP tools. The area patches of $10mm \times 8.5mm$ were polished using the rotary single-nozzle and two-nozzle tools with number of passes. The maximum $\% \Delta R_a$ value of 24.32% has been observed for the rotary single-nozzle polishing tool in 16 number of polishing passes that took $8min$. The trend of the graph represents that the $\% \Delta R_a$value increases as number of polishing passes increases which means it takes more polishing time to polish the desired workpiece sample using rotary single-nozzle tool. While, in rotary two-nozzle polishing process, the achieved $\% \Delta R_a$value is 50% in 12 number of polishing passes that took time period of $6min$. Thus, the rotary two-nozzle FJP tool comparatively reduced the average surface roughness to half the value in $3/4$ time period compared to rotary single-nozzle. So, in this context the use of two-nozzle polishing process is more beneficial when polishing time and surface roughness is concerned and an area of $85mm^2$ was polished in just $6min$ with a $\% \Delta R_a$ of 50%.

Thus, in non-rotary single-nozzle tool that took $525min$ to polish an area of $40mm \times 50mm$ with the raster toolpath yielding the $\% \Delta R_a$ of 73.33% on an initial surface of R_a equal to $300nm$, the rate of polishing achieved is $3.8095mm^2/min$. In comparison, the performance of the rotary two-nozzle polishing tool that took $6min$ to polish an area of $85mm^2$ yielding $\% \Delta R_a$ value of 50% on an initial surface of R_a equal to $380nm$ achieved the polishing rate of $14.1667mm^2/min$. Thus, the rotary two-nozzle tool has a much higher polishing rate compared to the non-rotary single-nozzle FJP tool for the polishing of Monel-400.

In the next chapter, investigation on fluid-jet polishing of AISI H13 die steel material using a non-rotary single-nozzle tool is presented along with the detailed procedure used to find out the optimum polishing parameters.

Chapter 5
Fluid jet polishing of AISI H13 die steel using non-rotary single-nozzle tool

The quality of die and mould surfaces plays an important role in the product quality as well as the productivity of the manufacturing industries. The precision dies are used to fabricate components having good mechanical properties including, toughness, hardness, and sufficient resistance to withstand high temperature fatigue cycles. AISI H13 die steel is one such material which is mostly used in automobile, aerospace, and marine applications. Several investigations have been made to improve the quality of surface finish achieved through FJP process, which has led to various findings in terms of the suitable range of the process parameters so as to enhance the stability of the effective material removal zone (also known as tool influence function or TIF) and the material removal rate. In this chapter presents the study on the investigation on the simultaneous effect of jet pressure, stand-off distances and polishing time on the surface finish of AISI H13 die steel material. In this study, the abrasive slurry containing machining oil was used with the 3D printed single-nozzle tool under non-rotary conditions to improve the surface finish of tool influence function (TIF) zone in FJP polishing of AISI H13 die material. The optimum values of the FJP process parameters were determined for selecting the suitable range of feed rates for polishing AISI H13 die steel with improved polishing efficiency.

5.1 Design of experiment using CCD technique

The parametric study to determine the optimized parameters for fluid-jet polishing viz: fluid-jet pressure, stand-off distance and polishing time to maximize the percentage change in surface roughness ($\%\,\Delta R_a$) in polishing AISI H13 die material is conducted using design of experiment (DOE) technique. The fluid-jet pressure, stand-off distance and polishing time are the most critical parameters for transformation of W-shaped sectioned profile (central uncut material) to U-shaped sectional profile (uniform material removal) as reported by Wang et al. [10] and is discussed in detail in section 1.6. The Central Composite Design (CCD) technique of Response Surface Methodology (RSM) is used in the present work with three variables and five levels of each variable. The CCD method gives the central repeatability of process parameters to ensure the accuracy of the developed data/model.

Table 5.1: Control factors and their levels for FJP study on AISI H13 steel using non-rotary single-nozzle.

S. No.	Factors	Levels				
		1	2	3	4	5
1.	Pressure, P (bar)	8	9	10	11	12
2.	Stand-off distance, D (mm)	30	31	32	33	34
3.	Polishing time, T (sec)	150	160	170	180	190

Table 5.2: Range of fixed parameters for FJP study on AISI H13 steel using non-rotary single-nozzle.

S. No.	Parameters	Value
1.	Impact angle (α)	90
2.	Abrasive material	Silicon carbide (SiC)
3.	Slurry concentration (Weight, %)	6
4.	Abrasive mesh size	4000
5.	Workpiece	AISI H13 die steel
6.	Number of orifice	1
7.	Nozzle diameter	1.0 mm

Table 5.3: Experimental combinations and responses obtained for DoE study for FJP polishing of AISI H13 steel using non-rotary single-nozzle.

Exp. No.	P (bar)	D (mm)	T (sec)	Initial average surface roughness (nm)*	Experimental results for surface roughness (nm)					Predicted % ΔR_a Eq. (5.2)	% Error
					X_1	X_2	X_3	Average roughness	Experimental % ΔR_a Eq. (4.1)		
1	10	32	170	500 (4)	270	250	260	260	48	47.36	1.33
2	9	33	180	500 (7)	350	340	360	350	30	31.78	-5.95
3	8	32	170	500 (3)	320	310	330	320	36	33.84	6.00
4	10	32	170	500 (8)	250	260	270	260	48	47.36	1.33
5	9	31	180	500 (7)	280	260	270	270	46	46.03	-0.07
6	10	32	170	500 (9)	250	270	260	260	48	47.36	1.33
7	10	34	170	500 (4)	350	330	340	340	32	31.84	0.50
8	10	32	170	500 (9)	260	250	270	260	48	47.36	1.33
9	9	31	160	500 (10)	350	340	330	340	32	33.78	-5.58
10	10	32	170	500 (2)	250	240	260	250	50	47.36	5.27
11	11	31	160	500 (5)	320	300	310	310	38	35.53	6.49
12	10	30	170	500 (4)	310	320	300	310	38	38.34	-0.90
13	10	32	170	500 (7)	300	280	290	290	42	47.36	-12.77
14	9	33	160	500 (8)	360	350	340	350	30	30.53	-1.78
15	10	32	190	500 (10)	290	300	310	300	40	39.84	0.40
16	10	32	150	500 (9)	360	380	370	370	26	26.34	-1.31
17	11	33	160	500 (6)	280	270	290	280	44	43.28	1.63
18	11	33	180	500 (5)	280	270	260	270	46	44.53	3.19
19	12	32	170	500 (7)	280	260	270	270	46	48.34	-5.09
20	11	31	180	500 (9)	250	260	270	260	48	47.78	0.45

* Standard deviations are listed in parentheses

The range of the three control parameters and the other fixed parameters used in the CCD analysis, given in Table 5.1 and Table 5.2, have been identified from the recommended ranges of process parameters reported in the literature [4,5,6,10,19,20] for the FJP polishing and later confirmed from the initial trials conducted on the AISI H13 sample surfaces in the developed experimental set-up. The design of experiment plan developed using CCD method for three control parameters and five levels had 20 set of experiments, shown in Table 5.3.

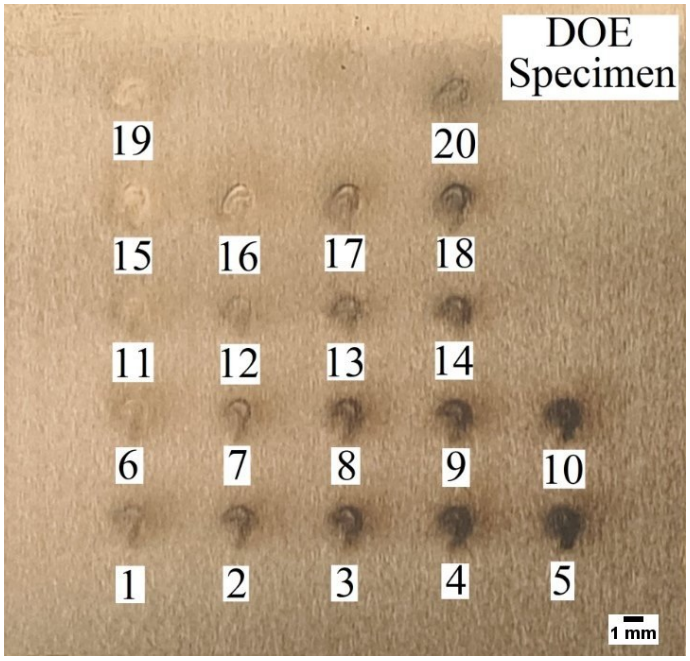

Figure 5.1: Fluid-jet polishing spots obtained on the AISI H13 die steel workpiece test surface [59].

In this work, AISI H13 die steel workpiece specimen was machined to the dimension of $75\ mm \times 70\ mm \times 12\ mm$ using a milling operation followed by grinding operation. Thereafter, the machined workpiece was cleaned using acetone solution and dried before conducting experiments using FJP process. The set of 20 trials planned for this DOE study, as per Table 5.3, were performed using the in-house developed FJP setup as discussed in chapter 3. The polished spots (TIF) for each of the 20 trials are shown in Figure 5.1. The individual trails were performed by varying the stand-off distance and polishing time for a constant jet pressure with a span of $8\ mm$ between each consecutive trial. The jet pressure was set manually while the stand-off distance, the linear traverse in XY-plane over the workpiece plate and the polishing time was automatically controlled on the CNC machine using a custom develop NC toolpath subroutine.

The surface roughness (R_a) values were measured on each polished spot of approximately 2 mm diameter (TIF) using SJ-400 Mitutoyo surface roughness profilometer with $0.8mm$ cut-off length. The measured R_a values and their averages are shown in Table 5.3. Further, the percentage change in actual surface roughness ($\% \Delta R_a$) after polishing has been determined using Equation (4.1). Where, the initial average surface roughness for the AISI H13 test sample surface was $500nm$.

5.2 Analysis of variance (ANOVA)

In order to evaluate the effect of the FJP process parameters namely: the fluid-jet pressure, stand-off distance and the polishing time for the set design of experiments as shown in Table 5.3, the central composite design (CCD) has been used. CCD method allows for the prediction of the second-order behaviour of the responses for a wider range of process parameters. The quadratic (second-order) polynomial model can be expressed with the help of the regression equation given by Equation (5.1):

$$Y = \beta_0 + \sum_{i=1}^{k} \beta_i X_i + \sum_{i=1}^{k} \beta_{ii} X_i^2 + \sum_{j>1} \sum \beta_{ij} X_i X_j + \varepsilon \quad (5.1)$$

Where, Y represents the response variable, β_0, β_i and β_{ij} are the constants, k represents the number of variables, ε represents the random error and X_i, X_i^2, $X_i X_j$ are the first order, second order and interaction terms of the process parameters, respectively [60].

In the present work, ANOVA was used to analyse the experimental results and identifying the influencing factors (fluid-jet pressure, stand-off distance and polishing time) which have a significant effect on the output variables. The ANOVA test allows a comparison of more than two groups at the same time to determine the existence of relationship between them. Based on ANOVA, non-significant terms were omitted on the basis of Fisher's F-test value while the significant terms were ordinarily acknowledged at 95% level of confidence.

The Table 5.4 lists the results of ANOVA and the F-test in order to evaluate the statistical significance of the aforementioned quadratic regression equation. The moderate Fisher's F-test value (F=22.19) with a very low probability value (also called the p-value) of prob > F (< 0.0001) demonstrates a high statistical significance of the regression model to represent the actual relationship between the obtained experimental data of percentage change in surface roughness ($\% \Delta R_a$) and three control variables. The p-values show the level of significance of each factor. Lower p-values indicate that the factor values have higher probability of falling within the ranges which impact the outcome of the experiment.

Table 5.4: ANOVA for percentage change in surface roughness (% ΔR_a).

Source	Sum of squares	Degree of freedom	Mean square	F-value	Prob > F		% contribution
Model	1020	8	127.50	22.19	< 0.0001	Significant	
P	210.25	1	210.25	36.59	< 0.0001		17.35
D	42.25	1	42.25	7.35	0.0202		3.49
T	182.25	1	182.25	31.72	0.0002		15.04
P^2	61.83	1	61.83	10.76	< 0.0001		5.10
D^2	236.69	1	236.69	41.19	< 0.0001		19.53
T^2	320.12	1	320.12	55.71	0.0078		26.42
PD	60.50	1	60.50	10.53	0.0078		4.99
DT	60.50	1	60.50	10.53			4.99
Residual	63.20	11	5.75				
Lack of Fit	25.87	6	4.31	0.58	0.7391	Not significant	
Pure Error	37.33	5	7.47				3.08
Total	1083.20	19	57.01				

Furthermore, the regression model was developed using the least square method in Minitab software, and quality of the fit quadratic regression model was assessed by R^2 (R-squared), R^2 (predicted) and R^2 (Adjusted) values. The R^2 (R-squared) value indicates the goodness of fit; or how well the regression model fits the observed data. On the other hand, the relation between the regression model predictions for the new responses is indicated by the R^2 (predicted). The comparison with R^2 (Adjusted) is done to validate the model for new responses. The Adjusted R^2 adjusts the number of terms in the model. Its value increases only when the new terms improve the model fit. The adjusted R^2 and predicted R^2 values should be within approximately 20% of each other [61].

The quadratic regression equation for the developed model is given in Equation (5.2).

$$\% \Delta R_a = -4940.10227 - 53.01136P + 213.98864D + 21.26932T - 1.56818P^2 - 3.06818D^2 - 0.035682T^2 + 2.75000PD - 0.27500DT \quad (5.2)$$

The probability values for the control parameters in the quadratic analysis are found to be less than 0.05 which shows that the model is significant. The value of the predicted $\% \Delta R_a$ determined from Equation (5.2) are also shown in Table 5.3. Figure 5.2 shows the comparison between the predicted $\% \Delta R_a$ and the experimental $\% \Delta R_a$ values.

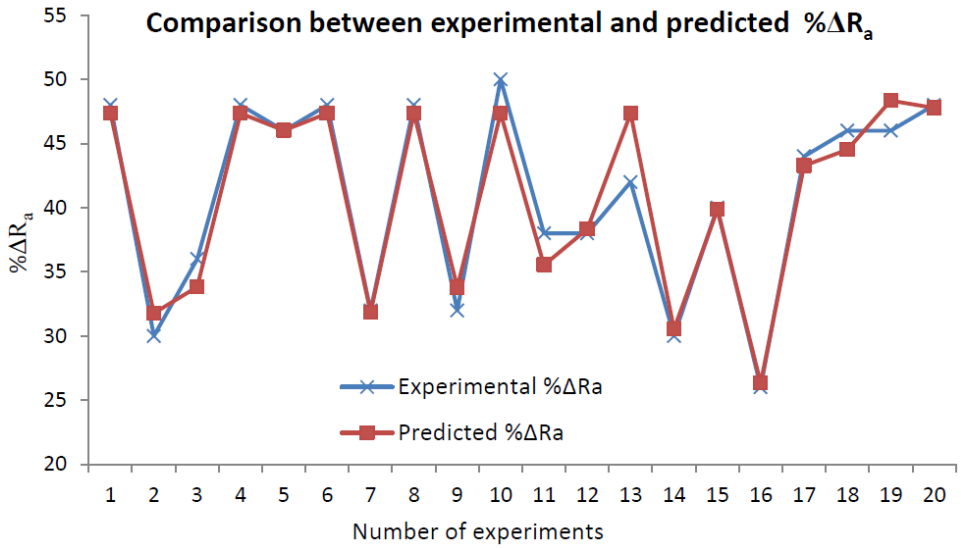

Figure 5.2: Variation between experimental and predicted values of % ΔR_a for FJP polishing of AISI H13 with non-rotary single nozzle tool [59].

It is evident from Figure 5.2 that the experimental and the predicted values do not have much variation over the entire range of the study. Also, the R^2 value for the regression model is 94.17%, R^2-Adj (adjusted R^2) is 89.92%, and the predicted R^2 is 80.04%. The predicted R^2 value for the model is in reasonable agreement with the R^2-Adj. The percentage contribution, given by Equation (5.3), depicts the parameters of significance in the regression analysis.

$$\text{Percentage contribution of parameter} = \frac{\text{Sum of square of parameter}}{\text{Total sum of square of model}} \times 100 \qquad (5.3)$$

The contribution of each of the control parameter is shown in Table 5.4, where it is observed the most contributing factor in the regression model is T^2 followed by D^2, P and T. Table 5.4 indicates that the polishing time was the most dominant factor contributing 41.46% to the predicted value of the percentage change in surface roughness (% ΔR_a) compared to stand-off distance and pressure which contribute 23.02% and 22.45%, respectively. It can also be seen from the table that the pure error contribution was only 3.08%.

5.3 Results and discussion

The regression model, given by Equation (5.2), was used to analyse the interaction of the control parameters (fluid-jet pressure, stand-off distance, time) and their effect on % ΔR_a in a single-nozzle FJP polishing. The ANOVA analysis indicates that three control parameters strongly influence % ΔR_a.

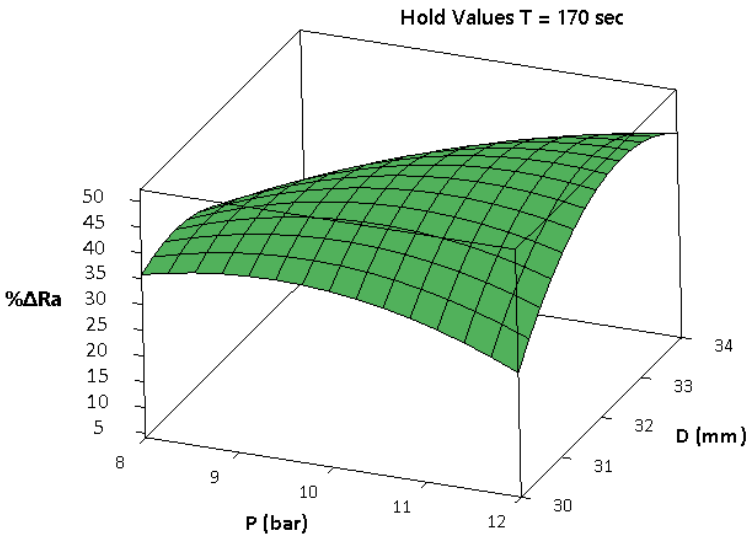

(a)

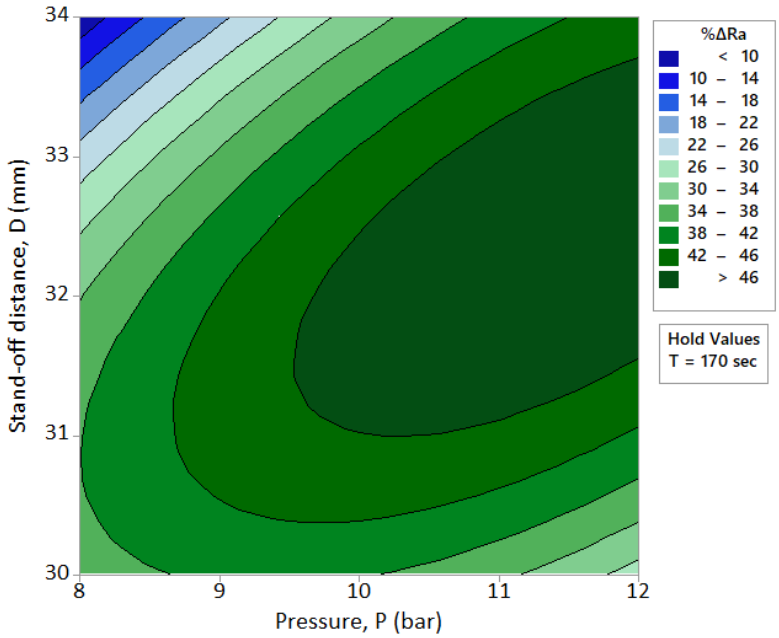

(b)

Figure 5.3: (a) Surface plot, and (b) Contour plot showing variation of % ΔR_a with P and D at $T = 170\ sec$ [59].

5.3.1 Effect of pressure and stand-off distance on surface roughness

The surface plot and the contour plot given in Figure 5.3(a) and (b) shows the simultaneous effect of pressure (P) and stand-off distance (D) on % ΔR_a at polishing time $T = 170\ sec$. It is clear from Figure 5.3 (a) and (b) that as the fluid pressure increases from $8bar$ to $12bar$, there is an increase in % ΔR_a value for the stand-off distance from $30mm$ to $31mm$. This is attributed to the reason that the kinetic energy of the abrasive particles for this pressure range and the stand-off distance is just sufficient to remove the material at a rate which is able to provide a better surface finish [62]. As seen from the contour plot shown in Figure 5.3 (b), the

% ΔR_a value is found to be in the highest range (more than 46%) corresponding to the pressure and the stand-off values of $11bar$ and $32mm$, respectively.

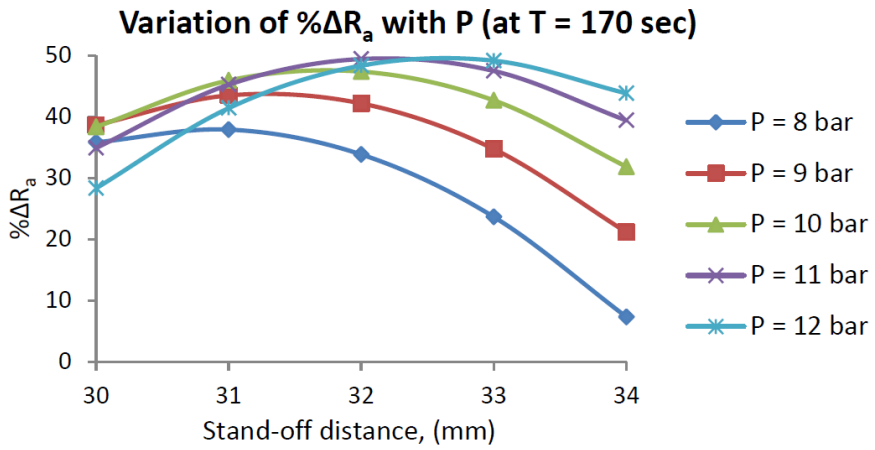

Figure 5.4: Variation in percentage change in surface roughness (% ΔR_a) at time 170 sec with respect to stand-off distance [59].

For the value of stand-off distance beyond $32mm$, the % ΔR_a declines for the entire pressure range, as can be seen in Figure 5.4. The decrease in the % ΔR_a value is due to the fact that the simultaneous increase in slurry pressure and stand-off distance, increases the material removal rate (MRR) in the TIF zone [62]. The increase in MRR is attributed to the increase in the kinetic energy of the abrasive particles which strikes the workpiece surface with higher impact energy. At the same time, the increase in stand-off distance makes the slurry jet unstable along with the randomization of the abrasive particles, which leads to the poor surface finish.

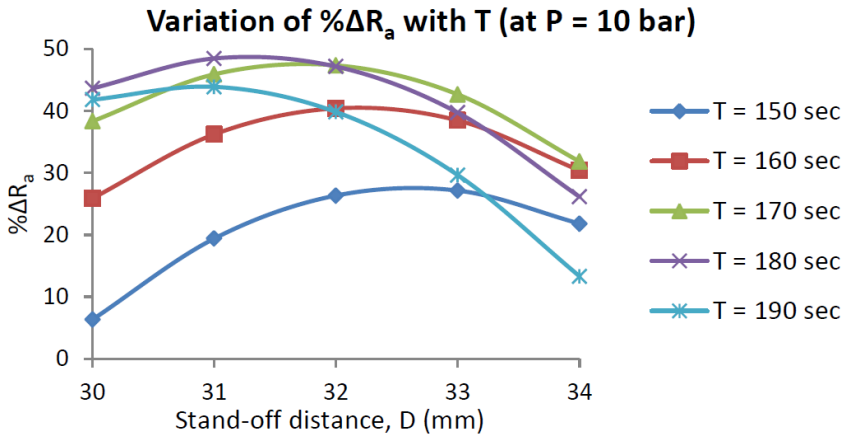

Figure 5.5: Variation in percentage change in surface finish (% ΔR_a) with stand-off distance D (at pressure $P = 10\ bar$) [59].

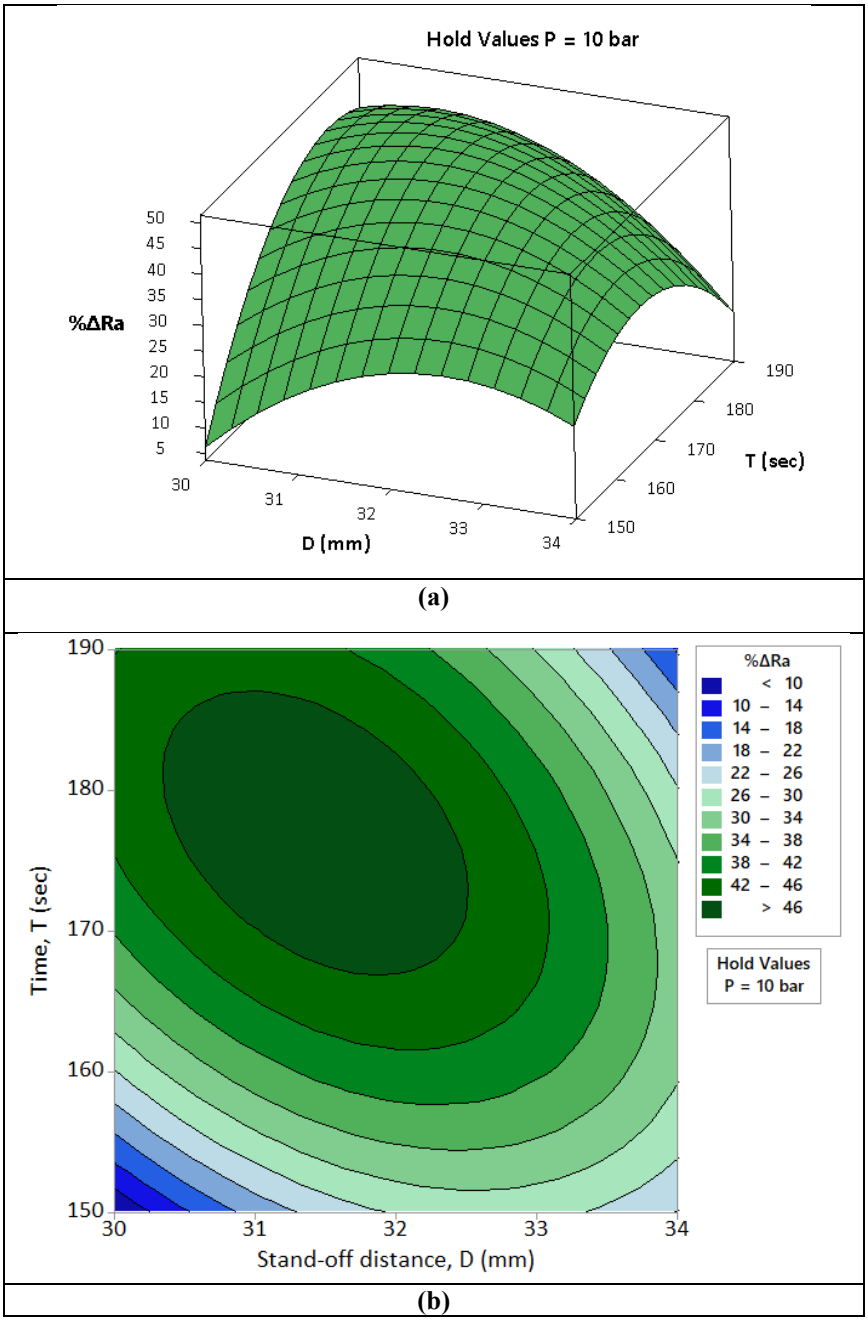

Figure 5.6: (a) Surface plot, and (b) contour plot for the percentage variation in surface roughness (% ΔR_a) at pressure $P = 10\ bar$ with respect to stand-off distance D and polishing time T [59].

5.3.2 Effect of stand-off distance and polishing time on surface roughness

Figure 5.5 shows the simultaneous effect of stand-off distance (D) and time (T) on % ΔR_a. It was clear from Figure 5.5 that the % ΔR_a increases with the increase in stand-off distance up to a certain value between $30mm$ to $32mm$, beyond which the % ΔR_a starts to reduce. This trend is found to be consistent for all time levels ranging from $150sec$ to $170sec$. The trend for % ΔR_a shows that the polishing time between $170sec$ and $180sec$ generates the highest surface finish for the entire range of stand-off distance from $31mm$ to $32mm$. The decrease in % ΔR_a at higher stand-off distance is due to over polishing with the simultaneous increase

in these two parameters [10]. The interaction of stand-off distance and polishing time is shown in Figure 5.6, where it is observed that the maximum % ΔR_a is achieved at stand-off distance of $32mm$ for the time period between $170sec$ to $180sec$.

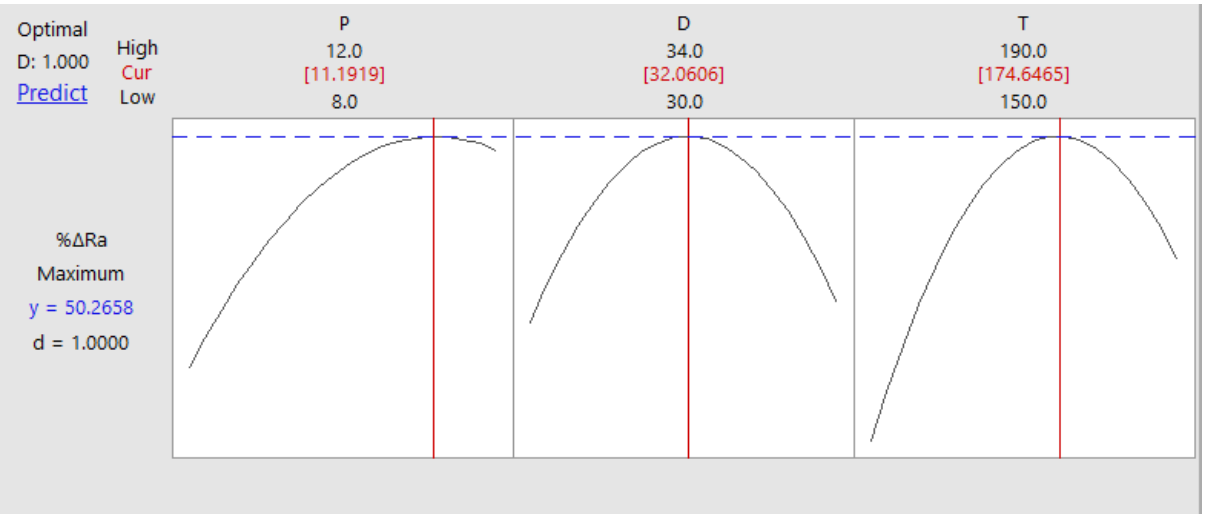

Figure 5.7: Optimized values of control parameters, *P*, *D* and *T*, obtained from the CCD study of fluid-jet polishing of AISI H13 steel using single-nozzle tool [59].

5.3.3 Optimization of the process parameters

The CCD method of Response Surface Methodology (RSM) in the Minitab (v17) software has been used to determine the optimum values of the control parameters that can maximize the % ΔR_a value during fluid-jet polishing of AISI H13 die steel material. This method helps to identify the factor settings that optimize a single response or a set of responses in order to determine the operating conditions that will result in a desirable response. The single-objective optimization has been implemented at '*unity*' of weight and importance, where '*weight*' determines how the desirability is distributed on the interval between the lower/upper bound and the target and the '*importance*' determines the relative importance of multiple response variables. The '*unity*' value of both the factors represents that all parameters (P, D and T) are equally important in the study.

The CCD approach, used in the present work, has shown a near symmetric response of the % ΔR_a for the entire selected range of the three control parameters P, D and T. Figure 5.7 shows the optimum value of 50.27% for % ΔR_a obtained from the quadratic regression model for the values of pressure, stand-off distance and time of $11.19bar$, $32.06mm$ and $174.65sec$, respectively. The vertical red lines in Figure 5.7 indicate the best values for the

factor affecting the response and horizontal dotted blue line shows the current setting of parameters.

Table 5.5: Confirmation test for FJP polishing of AISI H13 steel with non-rotary single-nozzle tool.

Exp. No.	Fluid pressure (bar)	Stand-off distance (mm)	Polishing time (s)	Experimental % ΔR_a	Predicted % ΔR_a Eq. (2)	Error (%)
1.	11.1	32	174.6	51.22	50.25	1.89
2.	11.1	32	174.6	52	50.25	3.36
3.	11.1	32	174.6	48.78	50.25	3.01

Three confirmation tests have been conducted using the optimized values of the control parameters to validate the study on the AISI H13 plate having an initial average surface roughness of $(500 \pm 10)nm$ (the surface roughness measurements have been taken at ten different locations). Table 5.5 shows the experimental % ΔR_a values and the value obtained from the regression model given by Equation (5.3). The percentage error found between the experimental and the predicted % ΔR_a values was around 3.36% which validated the accuracy of the developed regression model.

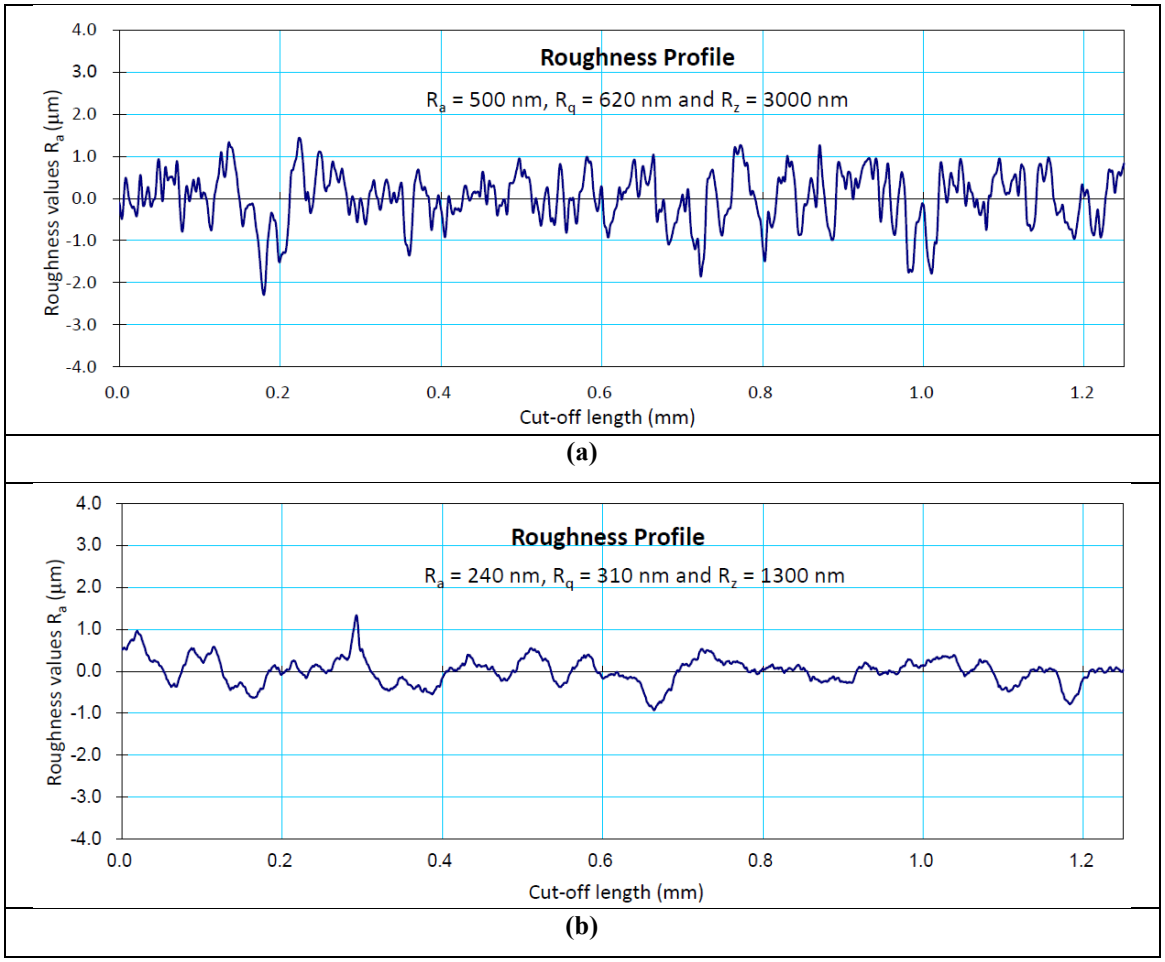

Figure 5.8: (a) Initial surface roughness profile of AISI H13 test specimen, and (b) surface roughness profile for the confirmatory tests of fluid-jet polishing at $P = 11.1 bar$, $D = 32mm$ and $T = 174.6\ sec$.

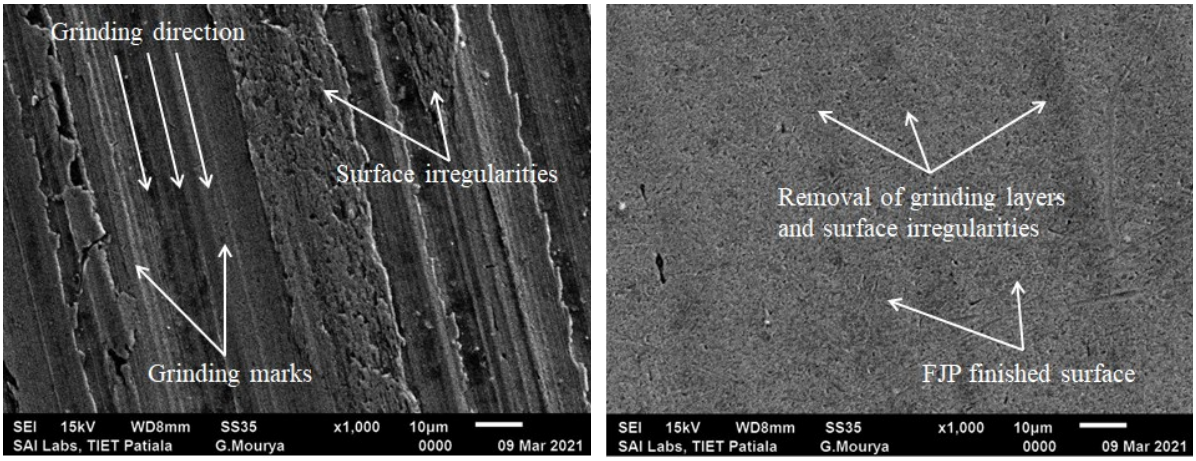

(a) **(b)**

Figure 5.9: Surface morphology of (a) initial surface and (b) final FJP polished surface at $P = 11.1bar$, $D = 32mm$ and $T = 174.6sec.$

Figure 5.8(a) shows the initial average surface roughness of the AISI H13 plate and Figure 5.8(b) shows the average surface roughness of $240nm$ achieved in one of the confirmation tests. It is clear from the roughness profile of the polished surface that a significant reduction in the peaks and valleys has been achieved using the FJP process as compared to the initial surface.

Scanning electron microscope (SEM) images of the initial specimen surface of AISI H13 steel and the surface characteristics of the polished TIF zones obtained from the confirmatory tests, shown in Figure 5.9(a) and Figure 5.9(b) respectively, have been used to analyse and compared the initial and the FJP polished surfaces. Figure 5.9(a) shows the presence of the grinding marks and surface irregularities on the initial grinded flat surface of the AISI H13. These grinding marks and major surface irregularities are minimized after applying FJP process with the optimum process parameters. Figure 5.9(b) shows a smoother surface finish achieved in the TIF zone. The polished surface also shows that it is free from the surface irregularities, the embedment of SiC abrasive particles and the cracks on the polished surface.

5.3.4 Area polishing using optimized process parameters

Selection of suitable feed rate is an important to achieve good surface finish with minimum lead time when polishing a larger surface. After determining the optimum FJP polishing parameters, we investigated the effect of different feed rates on surface roughness of rough and fine grinded AISI H13 die steel workpiece with an initial average surface roughness of $1140 \pm 15nm$ and $500 \pm 10nm$, respectively. The optimal values of pressure and stand-off distance

were kept constant at $11.1bar$ and $32mm$, respectively. The process parameters used for the experimentation are shown in Table 5.6.

Table 5.6: Process parameters and their levels.

S. No.	Process parameters	Values
1.	Feed rates, (mm/min)	0.25, 0.5, 1.0, 1.5, 2.0, 3.0, 4.0, 5.0, 7.5, 10.0, 12.5, 15.0, 20.0, 25.0, 30.0 and 35.0
2.	Pressure, P (bar)	11.1
3.	Stand-off distance, D (mm)	32.0
4.	Roughness of AISI H13 rough grinded surface (nm)	1140
5.	Roughness of AISI H13 fine grinded surface (nm)	500
6.	Toolpath footprint pattern	Raster

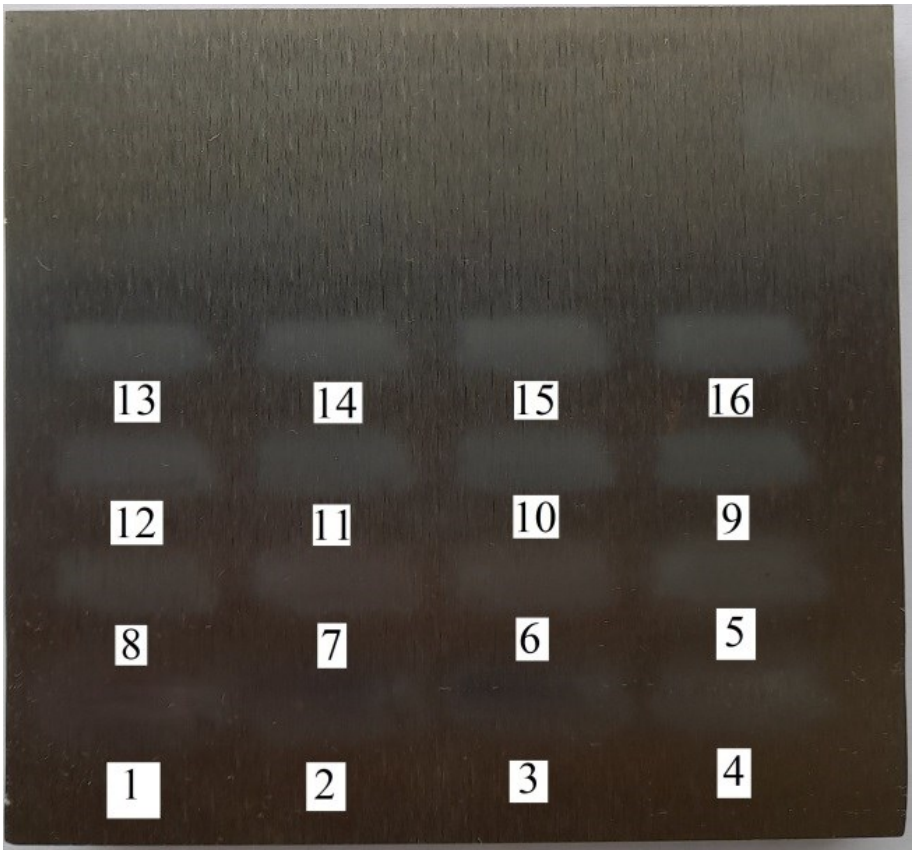

(a)

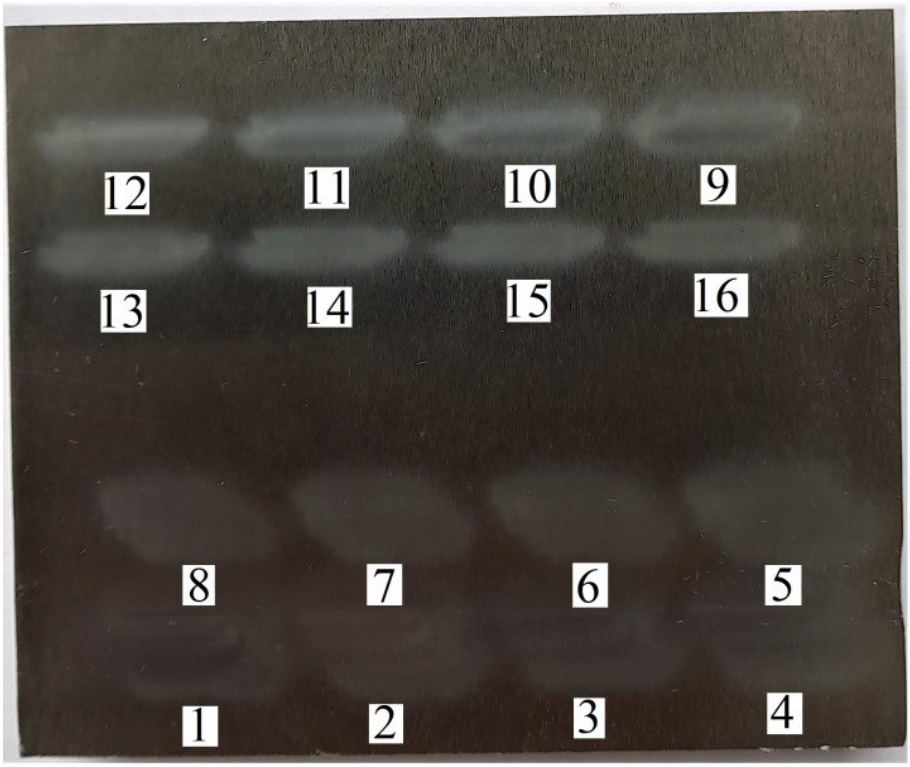

(b)

Figure 5.10: Feed rate trials on (a) rough grinded test surface (Plate-1), and (b) fine grinded test surface (Plate-2).

A total of 32 feed trials were performed on both rough and fine grinded AISI H13 specimen surfaces in raster manner as shown in Figure 5.10(a) and (b), respectively. The travel path of nozzle on workpiece plate has been kept as $10mm$ in horizontal linear direction which was perpendicular to the direction of lay of grinding. The consecutive gaps between trails have been kept as $7mm$ and $10mm$ in horizontal and vertical direction, respectively. The side-step of $1mm$ is used for the raster toolpath considering the diameter of TIF as $2mm$.

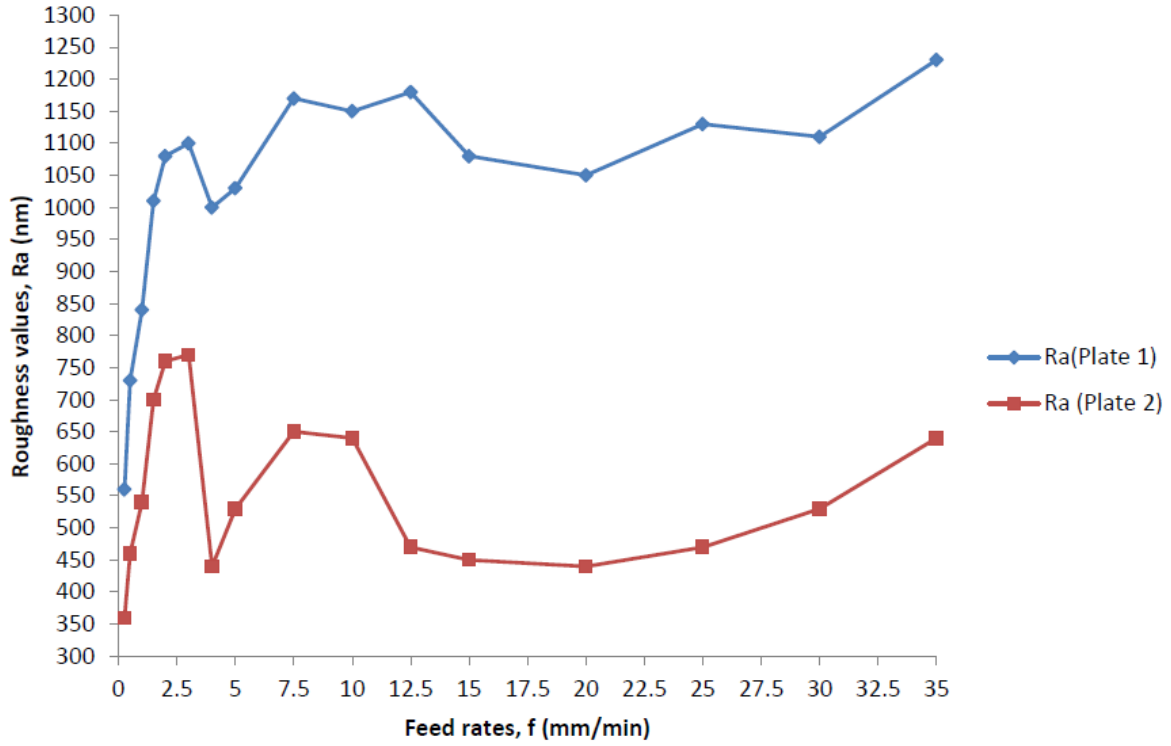

Figure 5.11: Comparison between surface roughness and feed rates on rough surface (Plate 1) and fine grinded surface of AISI H13 workpiece specimen (Plate 2).

After experimentation, the arithmetic surface roughness values were measured on each spot corresponding to all feed rates which are shown in Figure 5.11. Figure 5.11 shows a similar trend for surface roughness on both the rough and fine grinded plates. A lower feed rate of $0.5mm/min$ consumes more polishing time during experimentation as polishing time is inversely proportional to the feed rate. The polishing time is also depending on various polishing parameters such as polishing area, side-step distance and total length of toolpath. The polishing time (T) is proportional to the length of the toolpath and inversely proportional to the feed rate, as given by Equation (4.3).

As the feed rate increases, the surface roughness value increases but there are some intermediate ranges where surface roughness value decreased and reflected a better surface finish. It can be seen from Figure 5.11 that beyond the feed rate of $20mm/min$, the trend of roughness R_a increases because at higher feed rate the number of impacting particles per unit time are less which are insufficient for removing existing peaks and valleys on the substrate surface. However, this phenomenon occurred after $32mm$ stand-off distance. As the stand-off distance is measured beyond $32mm$ with $11.1bar$ fluid-jet pressure the cohesive bond between the abrasive particles becomes weaker due to which haphazard mixing (unorganised flow) between fluid-jet (carrier fluid) and abrasive particles creates highly turbulent fluid

stream. Hence, abrasive particles try to splash out from the slurry jet due to the action of higher environmental drag.

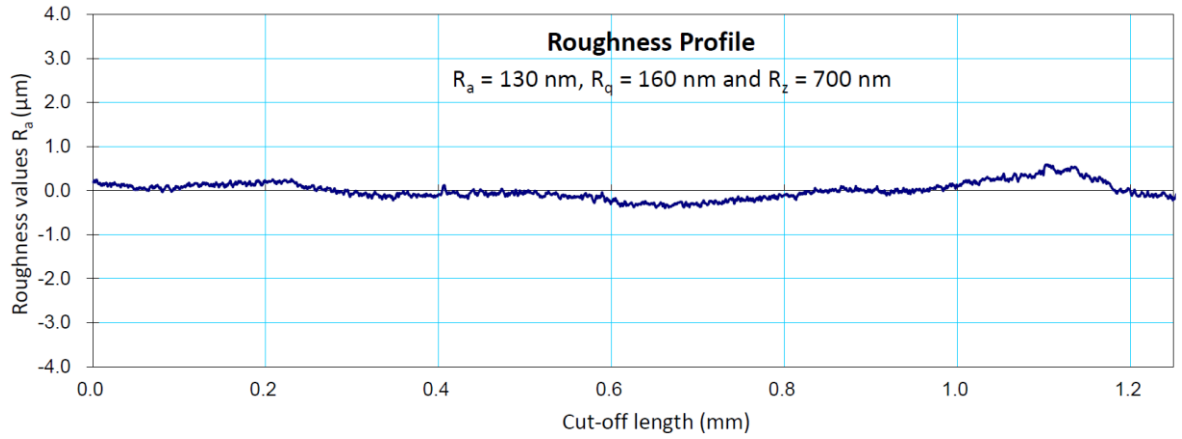

Figure 5.12: Surface roughness profile after fluid-jet polishing of AISI H13 steel specimen of $30mm \times 30mm$ with feed rate of $20mm/min$ and on the entire plate surface.

To further study the impact of polishing feed rate on the polishing quality and efficiency, the three specimens of AISI H13 die steel of dimension $30mm \times 30mm$ were polished using the fluid-jet Pressure (P) of 11.1bar and the stand-off distance (D) of $32mm$ in four multiple passes using three feed rates of $0.5mm/min$, $4mm/min$ and $20mm/min$. The initial surface roughness of the plate was $(500 \pm 10)nm$. The polishing time for the feed rates of $0.5mm/min$ and $4mm/min$ was found to be too high for the $30mm \times 30mm$ surface to be polished with the raster toolpath of side-step distance of $1mm$. The increase in polishing time increases the number of impacting particles per unit time resulting in the formation of new grooves on the polished surface causing the higher surface roughness at lower feed rates. Using the feed rate of $20mm/min$ and the side-step of $2mm$ for the raster toolpath, the surface area of $30mm \times 30mm$ was polished in $99.2min$ which yielded the average surface roughness of $130nm$ on the substrate surface as shown in Figure 5.12.

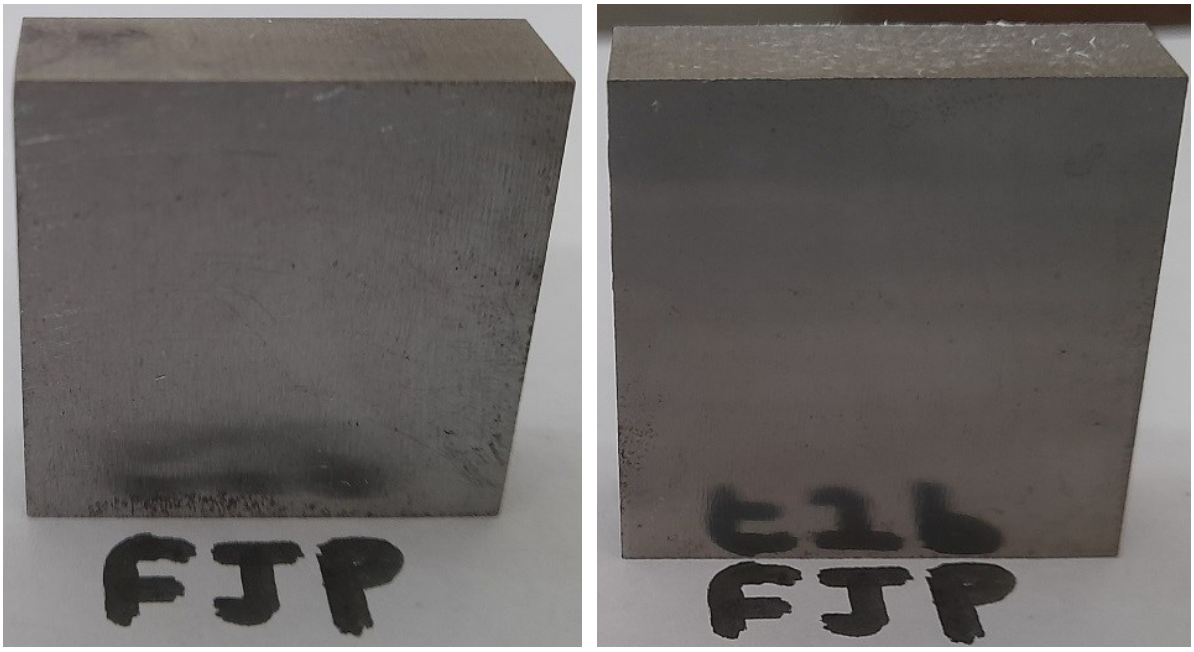

(a) **(b)**

Figure 5.13: (a) Mirror image of initial AISI H13 steel surface of $30mm \times 30mm$ after grinding to $500nm$ average surface roughness, and (b) Mirror image of AISI H13 steel surface after fluid-jet polishing with feed rate of $20\ mm/min$ with optimized parameters.

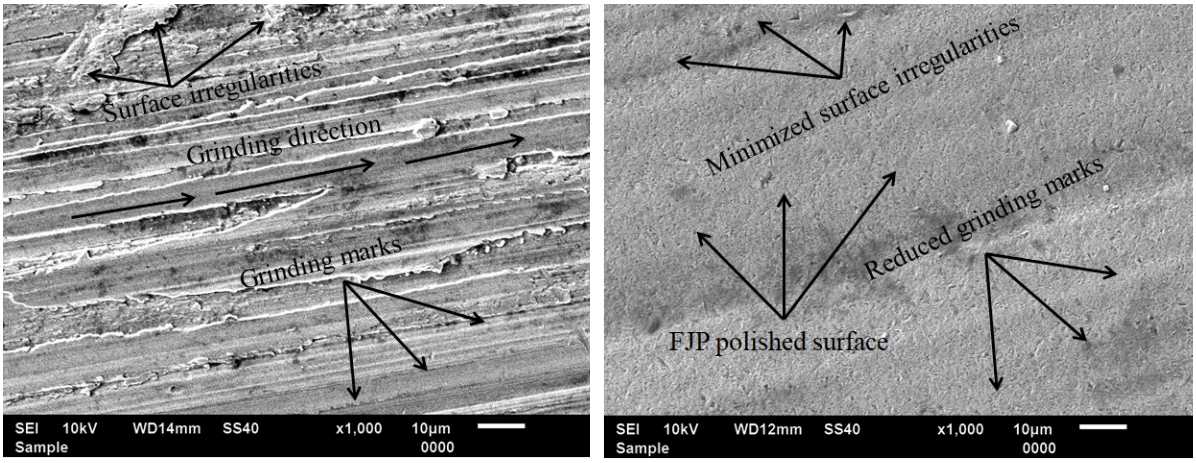

(a) **(b)**

Figure 5.14: (a) Surface morphology of initial AISI H13 test surface of $R_a = 500nm$ and (b) Surface morphology of AISI H13 steel surface after fluid-jet polishing with single-nozzle FJP tool.

The reduction in the percentage surface roughness, $\% \Delta R_a$, of 74% has been observed when the AISI H13 steel specimen of initial average roughness of $500nm$ when polished at the feed rate of $20mm/min$. The mirror images of the entire surface of AISI H13 die steel plate before and after the FJP finishing with a feed rate of $20mm/min$ are shown in Figure 5.13(a) and (b), respectively.

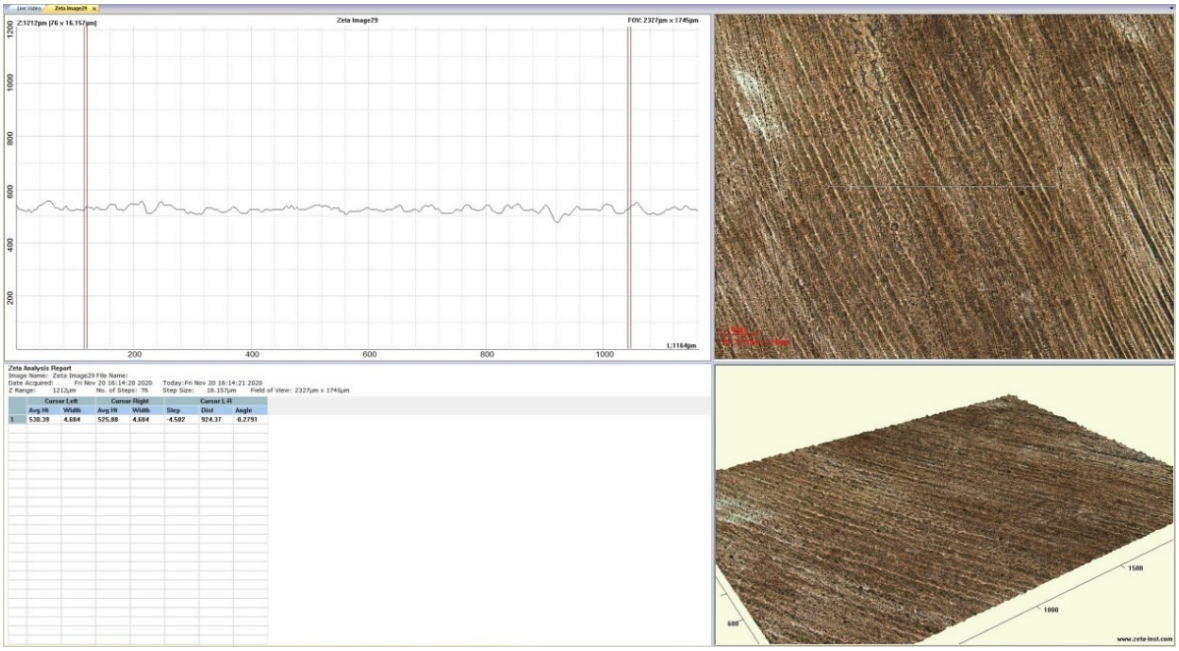

(a)

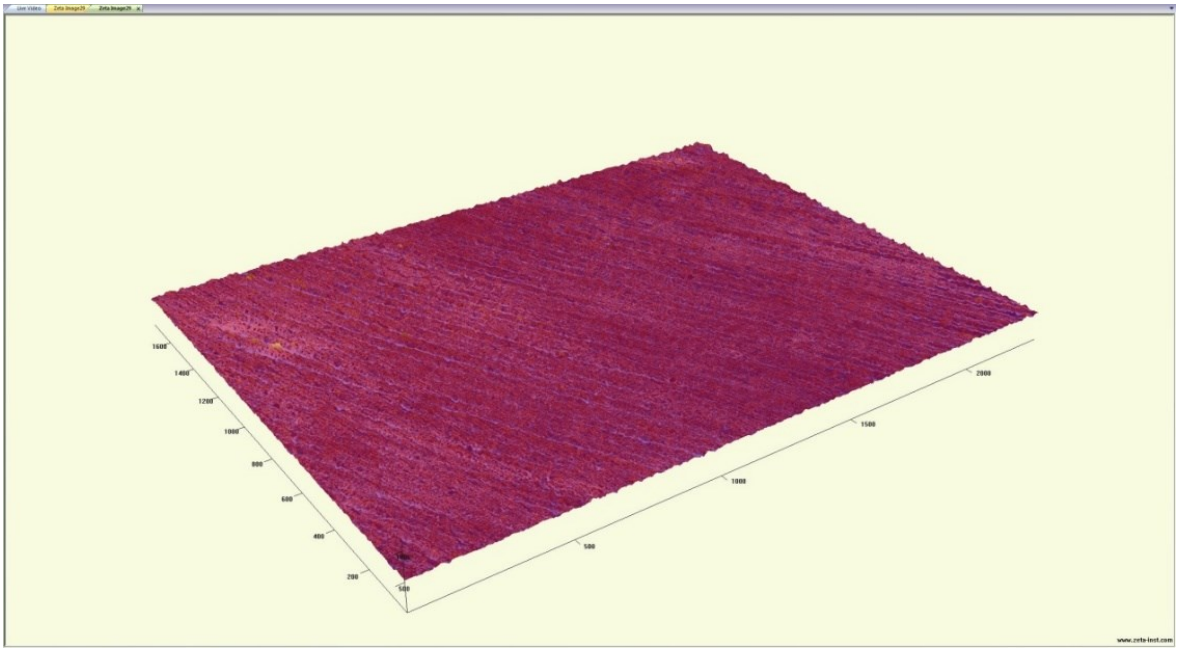

(b)

Figure 5.15: Material removal profile of fluid-jet polished AISI H13 steel of (a) measured surface and (b) 3D profile.

The surface characteristics of polished AISI H13 die steel specimen have been analysed and compared with the initial surface using scanning electron microscopy (SEM) images. The SEM images of, initial AISI H13 die steel surface of average surface roughness of $500nm$ and the surfaces polished using a fluid-jet traversing at feed rate of $20mm/min$, are shown in Figure 5.14(a) and (b), respectively. It is clear from Figure 5.14(b) that FJP polishing has significantly reduced the grinding marks and surface irregularities on the substrate surface of the AISI H13

die steel specimen as the SiC abrasive slurry jet from the single-nozzle FJP tool traverses in the raster manner resulting in a much better surface finish.

Figure 5.15(a) and (b) shows the measured contour and 3D topography of finished surface profile. The profile shows a removal of peak to valley on substrate surface using $20mm/min$ feed rate due to the reason that velocity was increased in the throat area of the nozzle and becomes maximum when slurry jets comes out of the nozzle. However, abrasive particles strike into the workpiece surface with the higher impact velocity. This impact velocity is further decomposed/divided into normal and tangential velocities. As the abrasive particles impact the surface with an inclination angle (α), their normal component of velocity was responsible for penetration of the workpiece material, which leads to deformation wear. The horizontal component of velocity was responsible for cutting action of the particles. In the cutting process, two type of abrasion occurs: Type I in which the particle loses all its kinetic energy during the collision whereas, in Type II particle loses only a fraction of its kinetic energy and bounces off the surface. Therefore, the main abrasion mechanism in FJP was ductile cutting of the surface under the lateral motion of the penetrating abrasives [4].

The abrasion mechanism was also dependent on the hardness of the workpiece material which varies over the period of time. The hardness of the AISI H13 die steel was measured with the help of micro-hardness tester. The rough sample was initially prepared to the required dimensions using milling operation. Then it was grinded to make the sample workpiece flat and to eliminate the uneven marks or peak-to-valley from the substrate surface so that the impression/indentation which is to be marked during the conduct of hardness test was visible on the surface. Thereafter the workpiece was cleaned using the acetone solution and dried properly before doing the hardness test on Vickers micro-hardness tester, MVH-1. In this method, a conical diamond indenter was used to permanently deform the surface in the form of impression/indentation. The diagonals of this impression in the form of conical diamond shape/deformed material were properly measured to calculate the value of micro-hardness. The values of micro-hardness were measured at ten different locations on the initial surface and FJP polished surface of AISI H13 die steel and the average of the measured values were taken. The average hardness values before and after polishing of 30 mm×30 mm AISI H13 die steel plate was found to be 392.2534HV and 396.2945HV, respectively. Thus, the results of the micro-hardness test reveal that the hardness of the substrate surface marginally increased after the FJP process due to the fact that that the material removal mechanism during FJP process is similar to the blasting process or shot peening process which increases the hardness of the substrate

surface. The average size of the abrasive SiC particles in FJP study is in the micrometer scale, while the size of particle used in shot peening and sand blasting is much larger. Hence, the impinging force of each particle in FJP is smaller than the shot peening and sand blasting, leading to the thinner hardness enhancement layer.

5.4 Closure

This chapter presented the study on the fluid-jet polishing (FJP) of AISI H13 die steel using a customized non-rotary 3D printed single-nozzle tool mounted on a precision 3-axis CNC vertical milling machine. The study determined the optimum values of the three most important FJP parameters namely: fluid-jet pressure, stand-off distance and polishing time, to maximize the reduction in percentage surface roughness ($\% \Delta R_a$) on the AISI H13 die steel workpiece surface using RSM methodology of CCD approach of design of experiments. As a result of the study, it is found that the maximum percentage reduction in surface roughness ($\% \Delta R_a$) in case of AISI H13 die steel workpiece surface has been found at optimum values of fluid-jet pressure, stand-off distance and polishing time of $11.1bar$, $32mm$ and $174.6sec$, respectively.

In addition, it is found in the study presented in this chapter that the feed rate of $20mm/min$ is best suited for polishing the AISI H13 steel substrate surface efficiently using a single-nozzle fluid-jet traversing in a raster toolpath with $2mm$ side-step distance. As a confirmatory test, a $30\ mm \times 30\ mm$ AISI H13 die steel plate specimen surface of initial average surface roughness of $500nm$ has been polished using fluid-jet pressure of $11.1bar$, stand-off distance of $32mm$ and feed rate of $20mm/min$. It has been found in the confirmatory test that the average surface roughness of the AISI H13 specimen surface has been reduced from $500nm$ to $130nm$ in $99.2min$ showing the reduction in peaks and valleys with surface improvement of 74%. This shows that the use of optimum values of FJP parameters (fluid-jet pressure, stand-off distance and polishing time of $11.1bar$, $32mm$ and $174.6sec$) at 20mm/min feed rate offers a significant polishing efficiency in terms of reduction in the percentage average surface roughness of 74% in four polishing passes at the polishing rate of $900mm^2/99.2\text{min}$ or $9.0725mm^2/\text{min}$.

In continuation of the study on FJP polishing of AISI H13 die steel, the next chapter presents the parametric study for fluid-jet polishing of AISI H13 die steel using customized designed 3D printed multi-nozzle rotary polishing tool.

Chapter 6
Fluid jet polishing of AISI H13 die steel using customized designed 3D printed multi-nozzle tool

In the chapter 5 the detailed investigation on the simultaneous effect of fluid-jet pressure, stand-off distance and polishing time on the surface finish of AISI H13 die steel obtained from FJP process has been described in detail. Further, the optimum values of the FJP process parameters have been determined a non-rotary single-nozzle custom designed 3D printed tool and further used to determine the suitable federate to maximize the rate of surface finish on AISI H13 steel. In this chapter, the work is further extended for studying the FJP polishing of AISI H13 die steel material using a custom designed 3D printed multi-nozzle tool to analyze the combined effect of spindle rotation and feed rate of the multi-nozzle fluid-jet tool to enhance the polishing quality and efficiency while ensuring the uniform material removal.

6.1 Initial trials of Experiments

To ensure the proper selection of the ranges for the most influencing FJP process parameters, the initial trials have been conducted using the multi-nozzle 3D printing tool as shown in Figure 3.2 in Chapter 3. In this work, we have used the custom designed 3D printed two-nozzle tools developed from Ti64 and SS316L as discussed in Section 3.1 in Chapter 3. Although the custom designed two-nozzle FJP tool which is 3D printed from SS316L has better tool life owing to the better material hardness, but we have performed some of the initial studies using the single-nozzle and two-nozzle FJP tools 3D printed from Ti64 because of the constrained availability of such materials and Metal 3D printing processes locally during the course of our work from March 2020 to December 2021. During the experimentation some of the FJP process parameters have been kept constant and others are varied with suitable combinations to study the effect of the most influencing FJP parameters on the quality of the polished AISI H13 surfaces in detail.

The multi-nozzle polishing tools are recommended for polishing large surface areas or region in minimum polishing time. For achieving uniform surface integrity and nano-scaled surface roughness, various factors that have been considered in the present study are: fluid-jet pressure, stand-off distance, spindle rotation (or the rotation of the axisymmetric fluid-jet nozzles), feed

rate, side-step distance for the raster toolpath used for area polishing and the number of polishing passes until the minimum surface roughness is achieved.

The combined effect of rotation of the axisymmetric fluid-jets (henceforth referred as the spindle rotation or spindle rpm), and the feed rate plays vital role for achieving the nano-scaled surface roughness on AISI H13 die steel workpiece material. The present work deals with the study of combined effect of feed rate and spindle rotation on surface roughness of AISI H13 die steel using two-nozzle FJP tool using the optimum values of the fluid-jet pressure and stand-off distance of $11.1bar$ and $32mm$ respectively as obtained from the study presented in Chapter 5.

Initially, a number of experimental trails were conducted to select the suitable range for spindle rotations per minute (rpm) and feed rates for improving the polishing efficiency. To check the consistency of surface polishing with the two-nozzle FJP tool, a total of 21 experiments were performed for spindle rotation ranging from $50rpm$ to $155rpm$. The polishing spots from these experiments are shown in Figure 6.1(a). It has been observed from Figure 6.1(a) that using a rotary axisymmetric two-nozzle FJP tool the consistency of polished spots on AISI H13 steel surface is maintained till $90rpm$ beyond which the jet interference phenomenon is observed. The jet interference is an undesirable phenomenon for achieving high accuracy surface finish.

Another set of experimental trails have been conducted to find out the suitable range of feed rates for surface polishing with a rotary axisymmetric FJP tool. A total of 9 experiments have been conducted for feed rate ranging from $5mm/min$ to $45mm/min$ keeping a fixed spindle rotation of $50rpm$. The polishing spots obtained from these experiments are shown in Figure 6.1(b). During experimentation, it was observed that working on low feed rates below $10mm/min$ resulted in over polishing and caused excessive material removal on the substrate surface, while the feed rate above $30mm/min$ leads to marginal polishing effect. For achieving uniform polishing process without degrading the surface integrity, the working feed rate range has been selected between 10 to $30mm/min$.

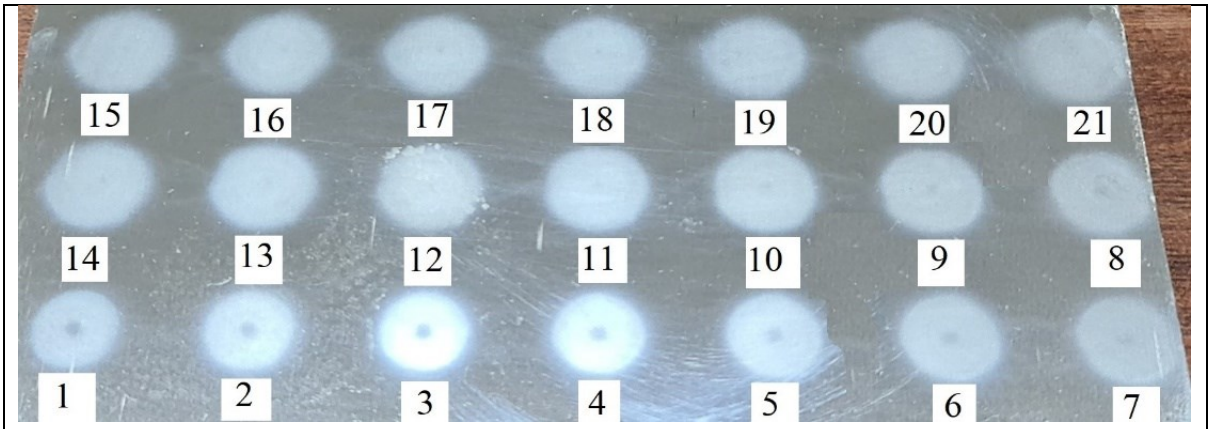

(a)

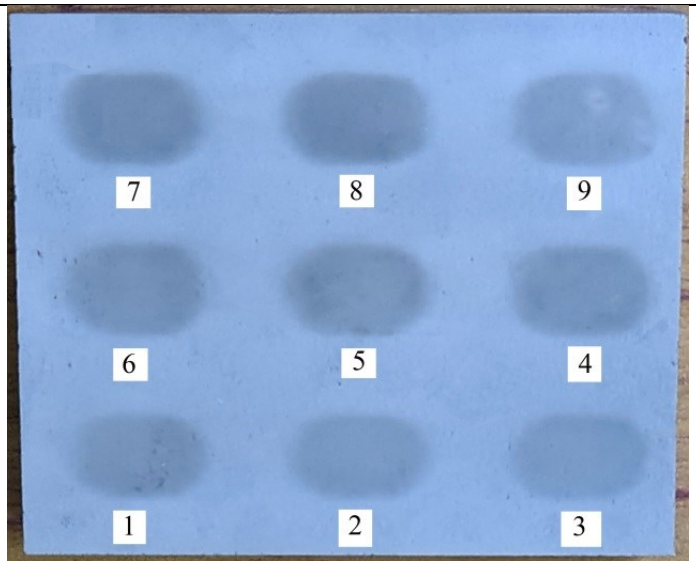

(b)

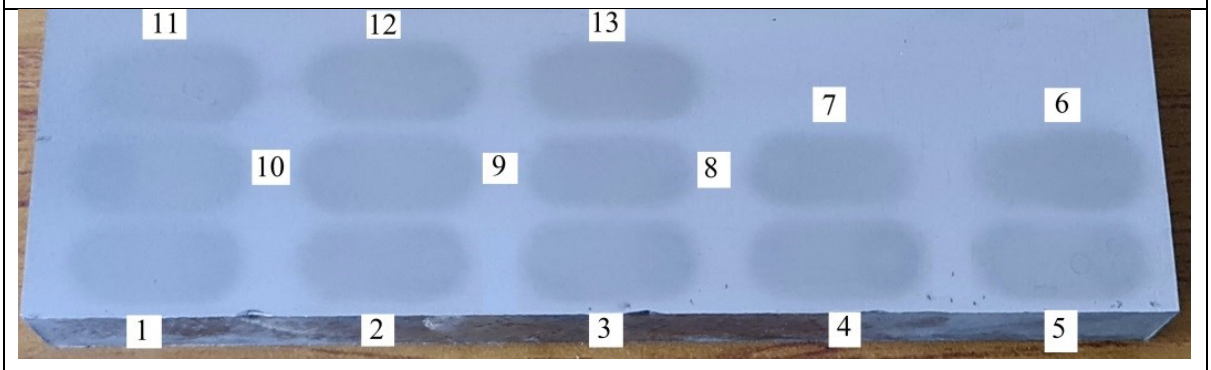

(c)

Figure 6.1: The results for the fluid-jet polishing spots obtained on AISI H13 workpiece specimen from the rotary axisymmetric two-nozzle tool for (a) spindle rotations trial experiments, (b) feed rates trial experiments, and (c) final design of experiment plan.

6.2 Design of Experiment

The parametric study to determine the optimized spindle rotation and feed rates to maximize the percentage change in surface roughness ($\% \Delta R_a$) for polishing AISI H13 die material has

been conducted using design of experiment (DOE) technique. Central Composite Design (CCD) method of Response Surface Methodology (RSM) was used with two variables and five levels of each variable. RSM explores the relationships between several explanatory variables and one or more response variables. The main idea of RSM was to use a sequence of designed experiments to obtain an optimal response.

Table 6.1: Control factors and their levels in CCD design of experiment

S. No.	Factors	Levels				
		1	2	3	4	5
1.	Feed rate, F (mm/min)	10	15	20	25	30
2.	Spindle rotation, R (rpm)	50	60	70	80	90

Table 6.2: Fixed parameters in CCD design of experiment

S. No.	Parameters	Value
1.	Impact angle (α)	90
2.	Abrasive material	Silicon carbide (SiC)
3.	Slurry concentration (Weight, %)	6
4.	Abrasive mesh size	4000
5.	Workpiece	AISI H13 die steel
6.	Number of orifice	2
7.	Nozzle diameter (mm)	1.0

The values of the control factors used in the CCD analysis are given in Table 6.1. The range of the two control parameters, namely the feed rate and the spindle rpm for the FJP study, have been determined on the basis of the quality of the polishing spots obtained from the initial trials shown in Figure 6.1(a) and (b). Also, the values of the fixed parameters used in the present study are given in Table 6.2.

The design of experiment plan developed using CCD method for two control parameters and five levels has 13 set of experiments as shown in Table 6.3. Each of the 13 trials were performed on a AISI H13 steel plate of $90mm \times 70mm \times 12mm$ using the developed FJP experimental setup. The polished spots for each of the 13 trials are shown in Figure 6.1(c). The individual trails were performed by varying the spindle rotation and feed rate horizontally (from left to right on plate shown in Figure 6.1(c)) for a constant jet pressure of $11bar$.

Table 6.3: Experimental combinations and their responses

Exp. No.	f (mm/min)	rpm (rev/min)	Initial average surface roughness, R_a (nm)	Experimental results for surface roughness, R_a (nm)					Predicted % ΔR_a Eq. (6.1)
				X_1	X_2	X_3	Average roughness, R_a	Experimental % ΔR_a Eq. (4.1)	
1	20	70	390	310	300	320	310	21	24.14190
2	30	70	390	320	330	330	327	16	17.49425
3	20	70	390	290	280	300	290	26	25.86207
4	20	50	390	290	310	300	300	23	22.49425
5	25	80	390	290	290	300	293	25	23.34483
6	15	80	390	350	350	350	350	10	11.43512
7	15	60	390	300	310	300	304	22	24.34483
8	25	60	390	300	300	300	300	23	22.01149
9	20	90	390	350	350	340	347	11	11.16092
10	20	70	390	280	280	280	280	28	25.86207
11	10	70	390	340	360	350	350	10	8.54251
12	20	70	390	280	270	290	280	28	25.86207
13	20	70	390	280	290	280	284	27	25.86207

The arithmetic average of three surface roughness (R_a) values measured on each polished spot (TIF) using SJ-400 Mitutoyo surface roughness profilometer with $2.5mm$ cut-off length have been recorded and used for the further analysis of the polishing results thus obtained. The measured R_a values and their arithmetic averages are shown in Table 6.3. Further, the percentage change in actual surface roughness ($\% \Delta R_a$) for each of the polished spot with respect to the initial average surface roughness has been determined using Equation (4.1) and is also shown in Table 6.3 under the column "*Experimental* $\% \Delta R_a$". The analysis of the values of the $\% \Delta R_a$ shows the measure of percent improvement achieved in surface roughness after the rotary FJP process.

Table 6.4: ANOVA analysis for percentage change in surface roughness ($\% \Delta R_a$)

Source	Sum of squares	Degree of freedom	Mean square	F-value	Prob > F		% contribution
Model	498.28	5	99.66	13.41	0.0018	Significant	
F	65.33	1	65.33	8.79	0.0210		10.80
R	96.33	1	96.33	12.96	0.0087		15.93
F^2	243.31	1	243.31	32.74	0.0007		40.23
R^2	116.89	1	116.89	15.73	0.0054		19.33
FR	49	1	49	6.59	0.0371		8.10
Residual	52.02	7	7.43				
Lack of Fit	18.02	3	6.01	0.71	0.5962	Not significant	
Pure Error	34	4	8.50				5.62
Total	550.31	12	45.85				

Further, the experimental results have been used to develop a second order regression model using Analysis of Variance (ANOVA) with 95% confidence level. The F-test was used to identify the implication of the process variables. The ANOVA analysis for study of % ΔR_a is presented in Table 6.4. The probability values for the control parameters in the quadratic analysis have been found to be less than 0.05 which shows that the model is significant. The quadratic regression equation for the developed model is given in Equation (6.1).

$$\% \Delta R_a = -28.44828 + 0.78046F + 1.47874R - 0.13034F^2 - 0.022586R^2 + 0.070000FR \quad (6.1)$$

The value of the predicted % ΔR_a determined from Equation (6.1) are shown in Table 6.3. As shown in Table 6.4, the R^2 value of the regression model, R^2-Adj (adjusted R^2) and the predicted R^2 values are found to be 90.55%, 83.79%, and 58.06% respectively. This show that the predicted R^2 value for the model is in reasonable agreement with the R^2-Adj.

In the regression analysis, the percentage contribution, which depicts the parameters that are significant, and are determined using Equation (6.2).

$$\text{Percentage contribution of parameter} = \frac{\text{Sum of square of parameter}}{\text{Total sum of square of model}} \times 100 \quad (6.2)$$

The contribution of each parameter is shown in Table 6.4. It is observed from Table 6.4 that the most contributing factor in the regression model is F^2 followed by R^2, R, F and FR. It indicates that the feed rate is the most dominant factor contributing 51.03% to the predicted value of the percentage change in surface roughness (% ΔR_a) compared to spindle rotation which contributes 35.26%. The pure error contribution is only 5.62% as shown in table 6.4.

6.3 Results and Discussion

The regression model shown in Equation (6.1) has been used to analyse the interaction of the control parameters; spindle rotation, feed rate and their effect on % ΔR_a for two-nozzle rotary FJP polishing of AISI H13 die steel. ANOVA analysis indicates that the two control parameters strongly influence the % ΔR_a. The variation of spindle rotation, feed rate and their interaction have been found to be significant as indicated by the regression model.

6.3.1 Effect of feed rate and spindle rotation on surface roughness

Figure 6.2(a) shows the effect of feed rate (F) on % ΔR_a at spindle rotation (R) as $60rpm$. It is clear from the trend that as the feed rate increases from $10mm/min$ to $20mm/min$, there is an increase in % ΔR_a value. This increase in % ΔR_a is attributed to the reason that the abrasive particles streamlined with the slurry-jet possess sufficient energy for material removal due to abrasion mechanism. As seen from the Figure 6.2(a), the % ΔR_a value is maximum for the feed rate value near to $20mm/min$. Beyond the feed rate value of $20mm/min$, the % ΔR_a value starts reducing. This reduction in % ΔR_a value is due to the fact that at higher feed rate the number of particles impacting per unit time less which is insufficient for removing the peaks and valleys on the substrate surface [20].

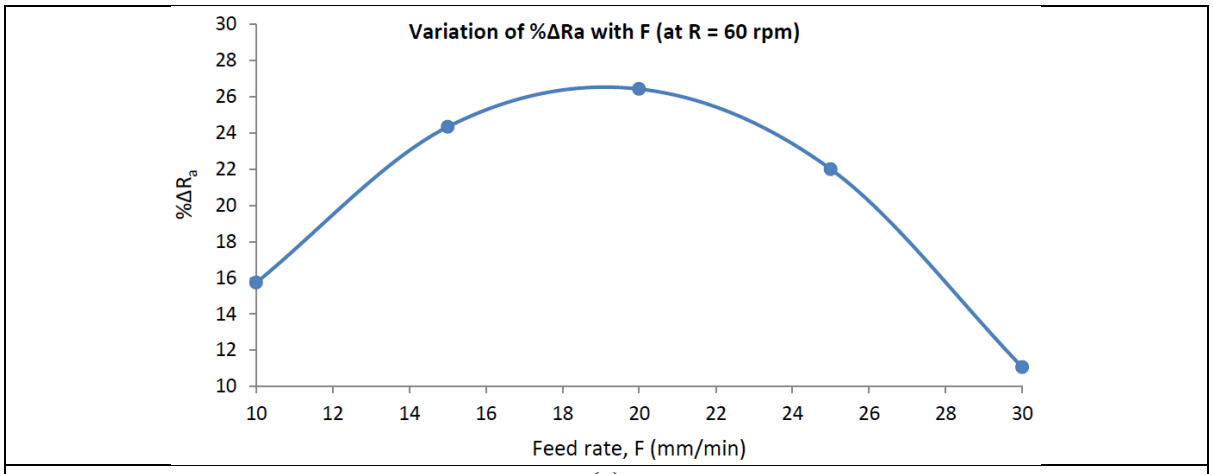

(a)

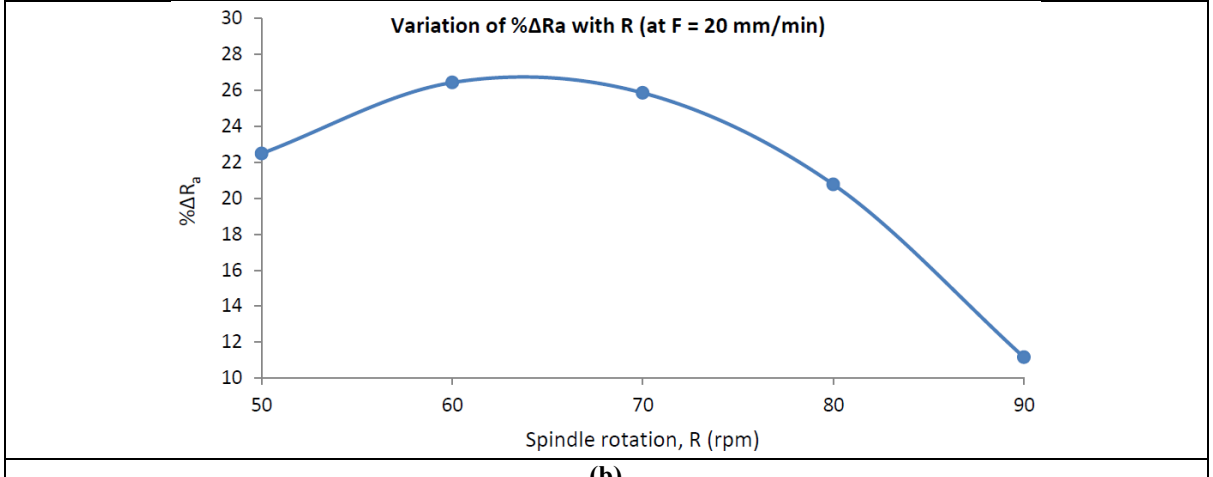

(b)

Figure 6.2: Variation in percentage change in surface roughness (% ΔR_a) with variation in (a) feed rate, and (b) spindle rotation.

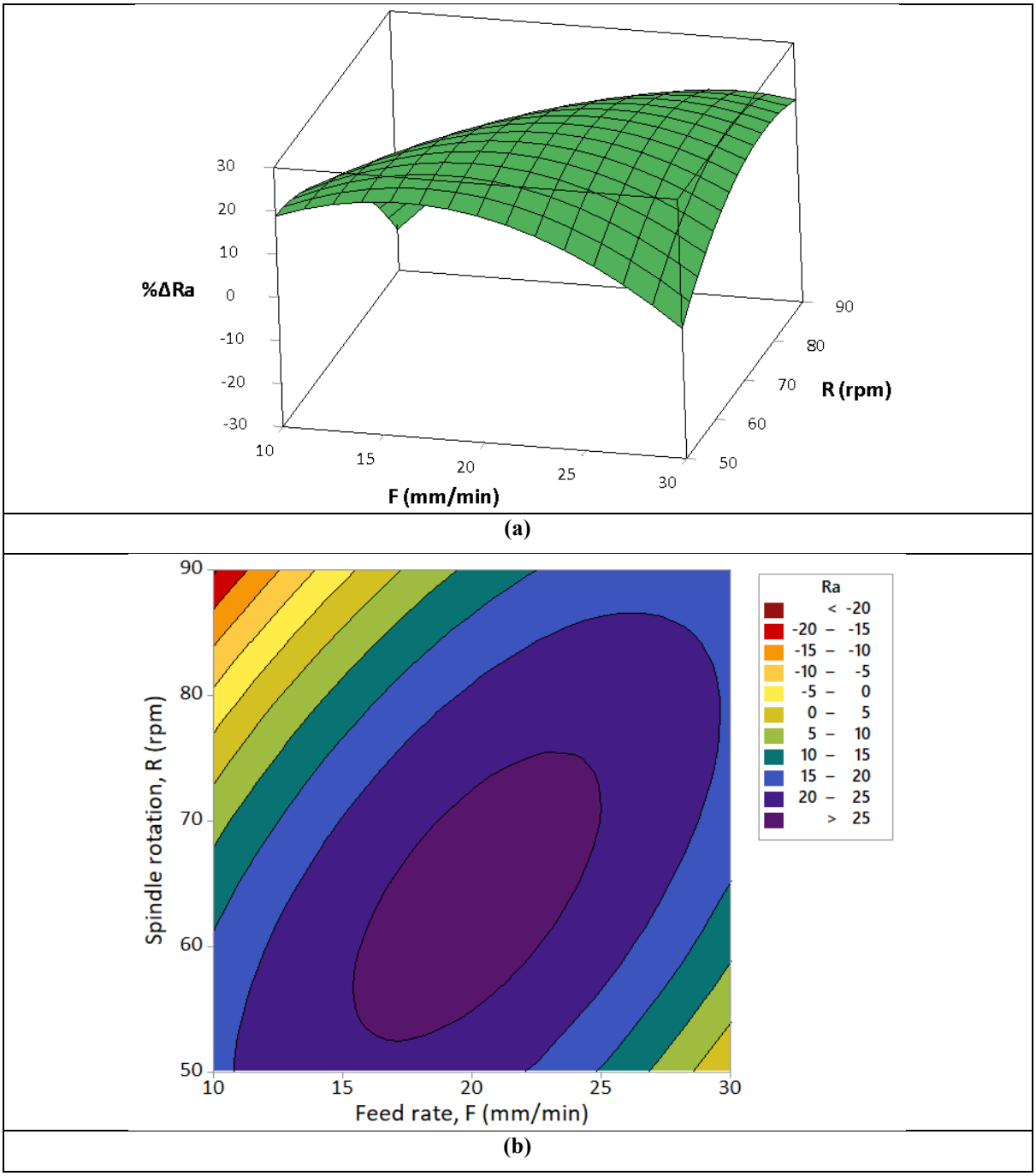

Figure 6.3: (a) Surface plot, and (b) the contour plot for the variation in percentage change in surface roughness (%ΔR$_a$) with respect to spindle rpm and feed rate.

Figure 6.2(b) shows the effect of spindle rotation (R) on $\%\,\Delta R_a$ at feed rate (F) of $20mm/min$. It is observed from the figure that as spindle rotation increases from $50rpm$ to $60rpm$, there is an increase in $\%\,\Delta R_a$ value. This is due to the reason that at lower spindle rotation abrasive particles are bonded together with the slurry jet domain and were also responsible for energizing the abrasive particles to chip-off the material with higher impact energy on the substrate surface [58]. The value of $\%\,\Delta R_a$ is found to be optimum at the spindle rotation value of $60rpm$. Beyond the optimum value of $60rpm$, the trend of $\%\,\Delta R_a$ value

decreases because at higher spindle rotation the bond between slurry jet and abrasive particles becomes weaker due to increase in air drag and the centrifugal forces. Also, abrasive particles try to splash out from the slurry jet due to the action of higher air drag and the centrifugal forces.

The simultaneous effect of feed rate (F) and spindle rotation (R) on $\% \Delta R_a$ is shown in the surface plot and the contour plot given in Figure 6.3(a) and (b). The concentric rings of the fringes in the contour plot shown in Figure 6.3(b) are a clear indicator that it is the effective kinetic energy of the abrasive particles which has a significant role to play in achieving a consistent MRR which intern can generate a better surface finish. The threshold kinetic energy of the striking abrasive particles for a desired range of $\% \Delta R_a$ can be achieved by various mutual combinations of feed rate and spindle rotation. The concentric rings of the fringes in Figure 6.3(b) shows that the optimized percentage change in surface roughness takes place at about a feed rate of $21mm/min$ and spindle speed of $63rpm$. But these optimized values of operating parameters ($F = 21mm/min$ and $R = 63rpm$) are not available in the experimental combinations given by the CCD method used in the present work. So, the closest available values to the optimized values of control parameters as per the experimental combination have been taken for further confirmatory study of the FJP process which are $F = 20mm/min$ and $R = 60rpm$. The optimized control parameters have been observed to generate a better surface finish with minimum surface irregularities.

6.4 Optimum Process Parameters

The work has been extended further to identify the FJP process parameters to maximize $\% \Delta R_a$ value for polishing AISI H13 die material using multi-nozzle tool. CCD approach used in this work has shown a near symmetric response of $\% \Delta R_a$ for the entire selected range of the two control parameters, F and R studied in this work.

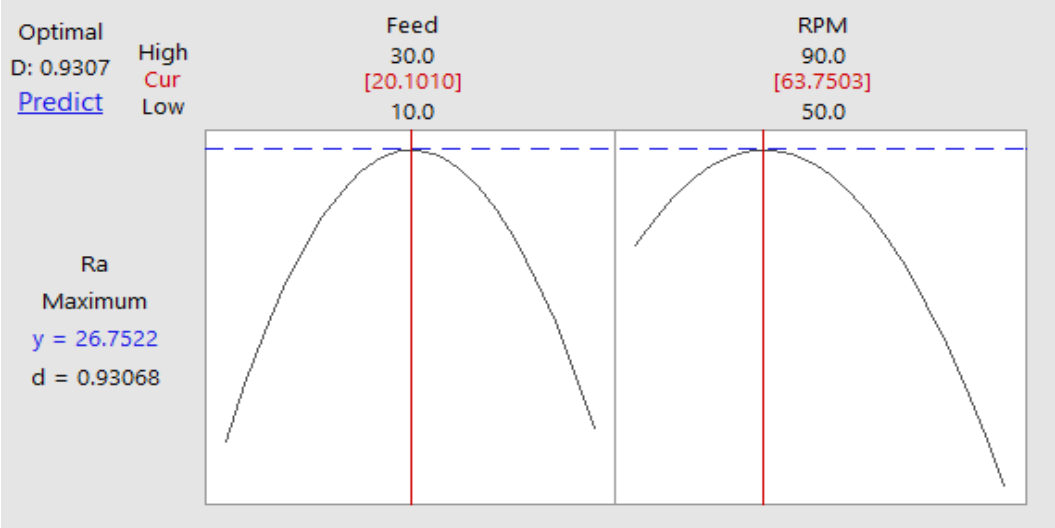

Figure 6.4: Optimized values of FJP control parameters feed rate and spindle rpm for polishing AISI H13 die steel with rotary two-nozzle fluid-jet tool.

The optimum value of % ΔR_a of 26.75% has been obtained from the quadratic regression model at feed rate of $20.1010 mm/min$ and spindle rotation of $63.7503 rpm$ respectively as shown in Figure 6.4.

Table 6.5: Confirmatory test FJP polishing AISI H13 die steel with rotary two-nozzle fluid-jet tool at optimized feed rate and spindle rpm.

Exp. No.	Feed rate (mm/min)	Spindle rotation (rpm)	X_1	X_2	X_3	Average roughness, R_a	Experimental % ΔR_a	Predicted % ΔR_a Eq. (2)	Error (%)
1.	20	60	300	280	290	290	25.64	26.43	-3.08
2.	20	60	290	280	290	286.67	26.49	26.43	0.226
3.	20	60	280	290	280	283.33	27.35	26.43	3.36

Three confirmatory tests have been conducted at feed rate and spindle rotation of $20 mm/min$ and $60 rpm$, respectively to check the validation of the study on the AISI H13 plate with $390 nm$ as average initial surface roughness. These confirmatory tests helped to validate the process parameter used in FJP process. Table 6.5 shows the experimental value of % ΔR_a and the value predicted using the regression model (given by Equation 6.2). The percentage error found between the experimental and the predicted % ΔR_a values lies between -3.08 to 3.36. The range of error found in the experimental results and regression model validate the accuracy of the developed regression model.

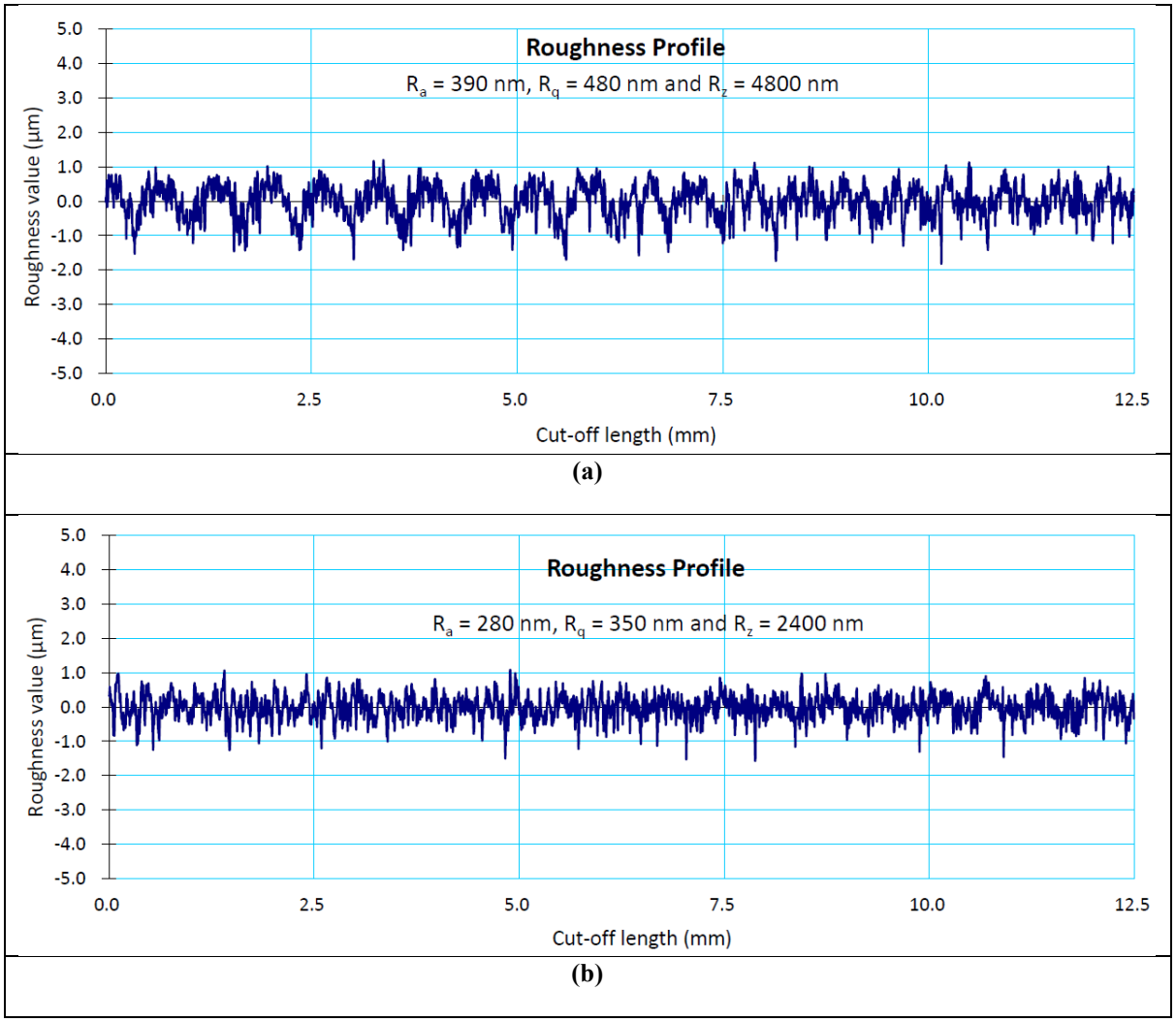

Figure 6.5: Surface roughness profiles for (a) initial surface and (b) final surface at $F = 20mm/min$ and $R = 60\ rpm$.

Figure 6.5(a) shows the initial average surface roughness of $390nm$ measured on the AISI H13 specimen plate and Figure 6.5(b) shows the average surface roughness of $280nm$ after fluid-jet polishing at feed rate and spindle rotation of $20mm/min$ and $60rpm$, respectively. It is clear from the roughness profile of the polished surface that a significant reduction in the peaks and valleys was achieved using the FJP process as compared to the initial surface.

To further study the effect of number of polishing passes on the process quality and the efficiency, the specimens of AISI H13 die steel of polishing area $25mm \times 10mm$ have been polished with number of raster tool passes with zero side-step value using optimal feed rate and spindle rotation. The initial surface roughness of the specimen plate was noted to be $390nm$. The polishing conditions used in the experimentation are shown in Table 6.6. The polishing spots for the different experimentations are shown in Figure 7.6.

Table 6.6: Polishing conditions for experimentation

S. No.	Parameters	Value
1.	Pressure, P (bar)	11.1
2.	Stand-off distance, D (mm)	32
3.	Feed rate, F (mm/min)	20
4.	Spindle rotation, R (rpm)	60
5.	Travel path length, L (mm)	25
6.	X-spacing (mm)	12
7.	Y-spacing (mm)	12
8.	Targeted polishing region, (mm^2)	25×8.5 = 212.5
9.	Polishing path	Raster toolpath with zero side-step
10.	Number of passes	2, 4, 6, 8, 10, 12, 14, 16

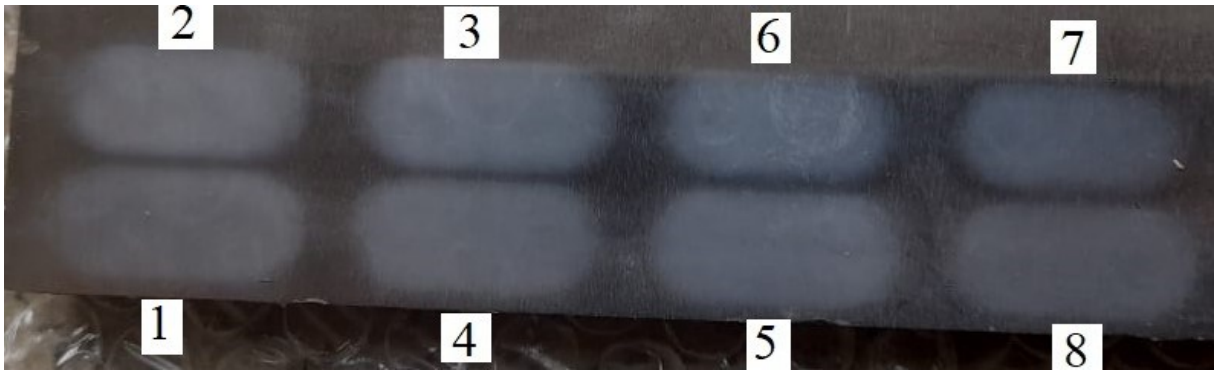

Figure 6.6: AISI H13 workpiece specimen polished with rotary two-nozzle fluid-jet tool with 2 to 16 number of polishing passes.

The total polishing time, T for a particular number of raster passes is proportional to the toolpath length and inversely proportional to the feed rate, as given by Equation (4.3). The polishing toolpath length, polishing time, and the average surface roughness after FJP polishing with rotary two-nozzle tool are shown in Table 6.7 and 6.8. Table 6.7 shows the trend of change in the peaks and valleys on AISI H13 substrate surface with respect to the initial surface roughness of $390nm$ after fluid-jet polishing with different number of polishing passes of rotary two-nozzle tool. It is observed that, as the polishing time increases, the surface roughness value decreases due to the fact that the number of impacting particles per unit time also increases resulting in removal of peak to valley on the substrate surface. The best surface roughness values of $110nm$ have been observed on the substrate surface after 12 passes that took $15min$ of polishing time. The maximum percentage reduction in surface roughness value ($\% \Delta R_a$) of 71.79% is achieved after 12 polishing passes as shown in Table 6.8. After 12 polishing passes, the surface roughness value increases because of over polishing which degraded the polished surface.

Thus, in case of maximum finishing (or maximum ($\% \Delta R_a$) of 71.79% achieved in twelve number of passes of the rotary fluid-jet polishing of AISI H13 steel offers a polishing rate of

$(212.5mm^2/15min) = 14.1666mm^2/min$. This polishing rate is 1.5614 times higher than the polishing rate of $9.0725mm^2/\text{min}$ achieved in case of non-rotary single-nozzle FJP tool for AISI H13 polishing as discussed in Chapter 5.

Table 6.7: Surface roughness profiles of AISI H13 specimen surface after different fluid-jet polishing passes of rotary two-nozzle 3D printed tool.

S. No.	Number of passes	Polishing time (in min)	Surface roughness profiles (in nm)
1.	2	2.5	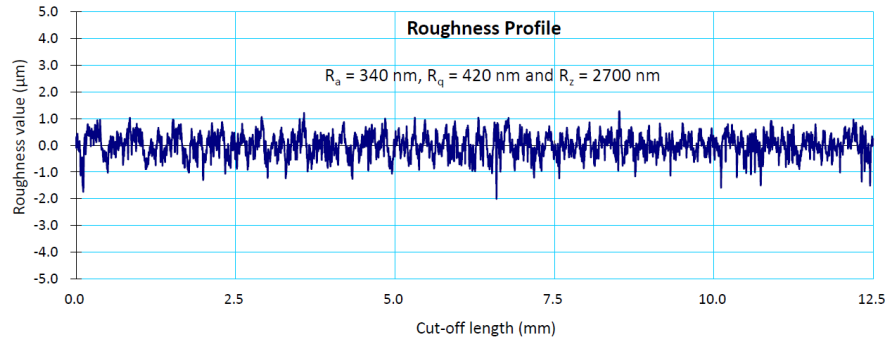
2.	4	5	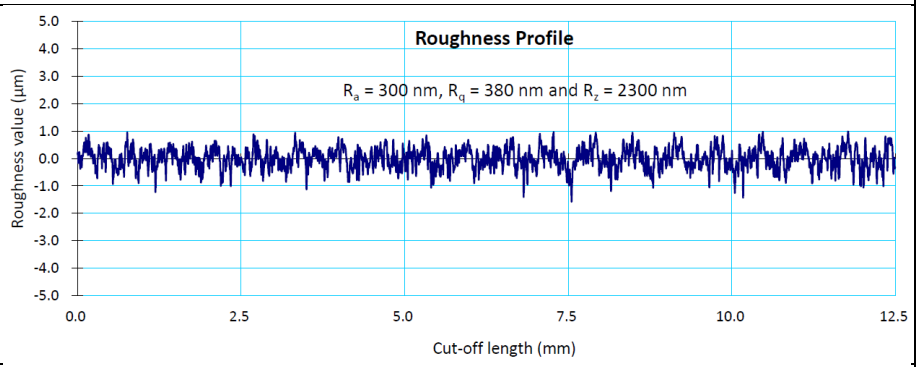
3.	6	7.5	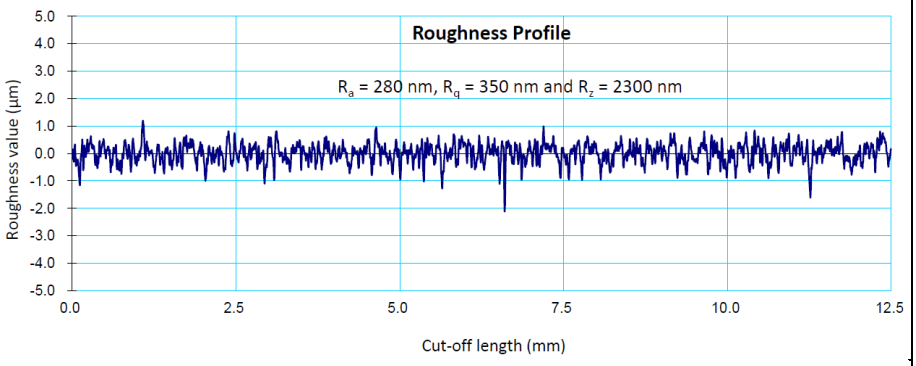
4.	8	10	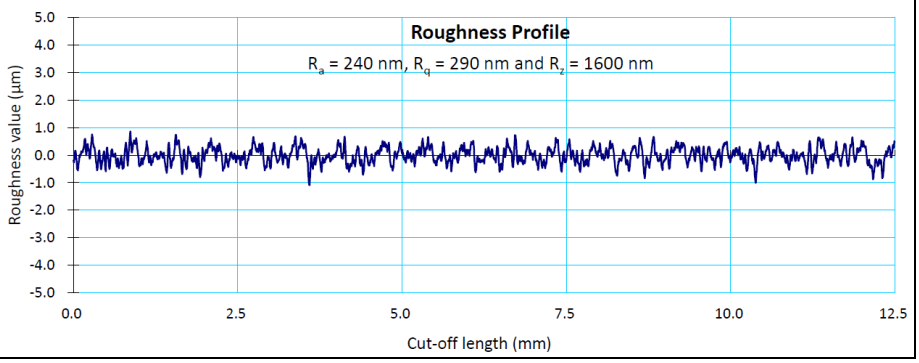

5.	10	12.5	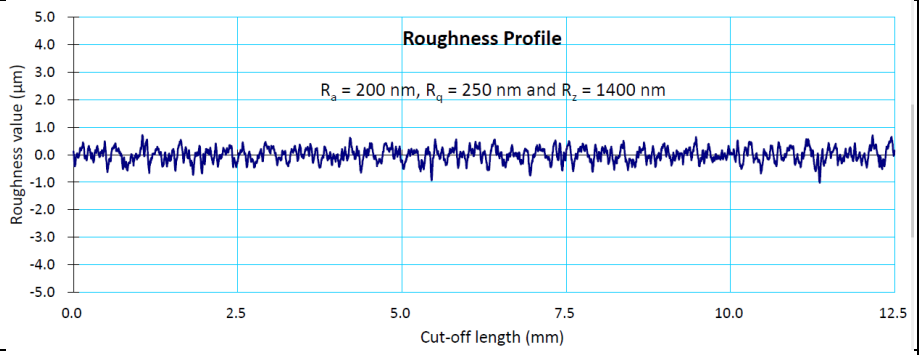
6.	12	15	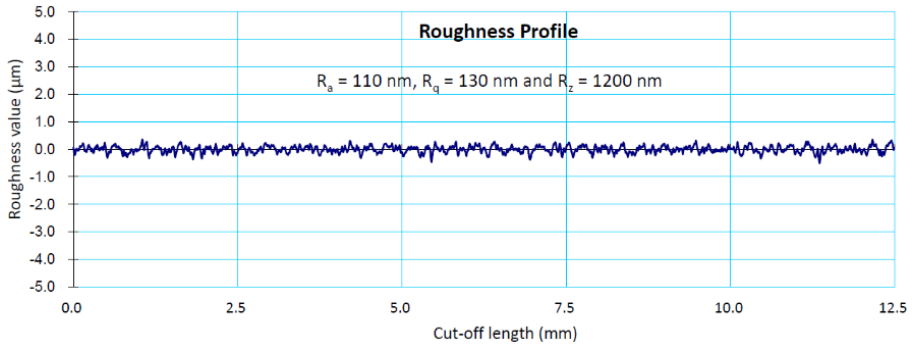
7.	14	17.5	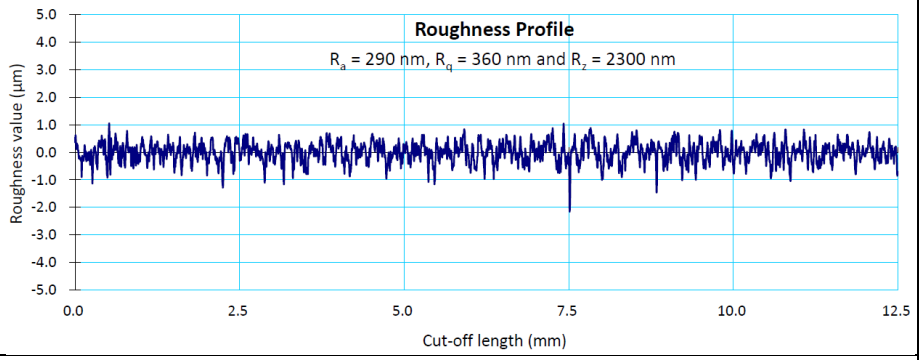
8.	16	20	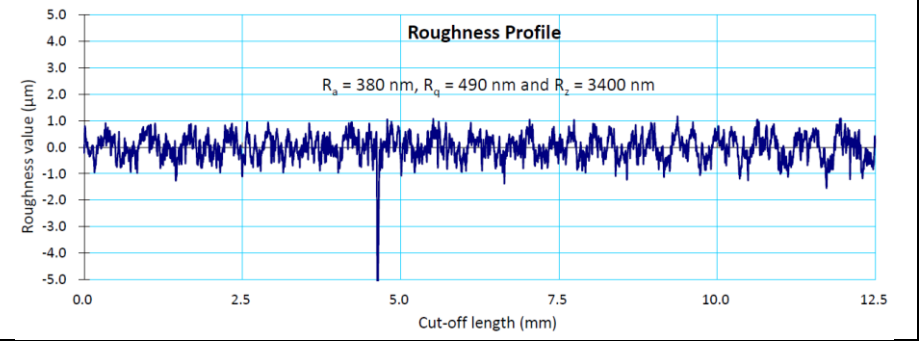

The surface characteristics of the polished zones on the AISI H13 plate with optimum polishing condition of feed rate as $20mm/min$ and spindle rotation as $60rpm$ have been analysed and compared with the initial surface of the AISI H13 specimen surface using the scanning electron microscope (SEM) images as shown in Figure 6.7. The SEM images of the initial and FJP polished surfaces are shown in Figure 6.7(a) and (b), respectively. Figure 6.7(a) shows the presence of the grinding marks and surface irregularities on the initial grinded flat surface of the AISI H13 material.

Table 6.8: Percentage change in surface roughness values ($\% \Delta R_a$) of AISI H13 steel specimen of initial surface roughness of 390nm after fluid-jet polishing with rotary two-nozzle FJP tool with feed rate of $20mm/min$ and spindle rpm of $60mm$.

S. No.	Number of polishing passes	Total Toolpath length of raster polishing pass (in mm)	Polishing Time T (in min)	Surface roughness, R_a after polishing (nm)	Percentage change in surface roughness ($\% \Delta R_a$) Eq. 4.3
1	2	50	2.5	340	12.82
2	4	100	5	300	23.07
3	6	150	7.5	280	28.20
4	8	200	10	240	38.46
5	10	250	12.5	200	48.71
6	12	300	15	110	71.79
7	14	350	17.5	290	25.64
8	16	400	20	380	2.56

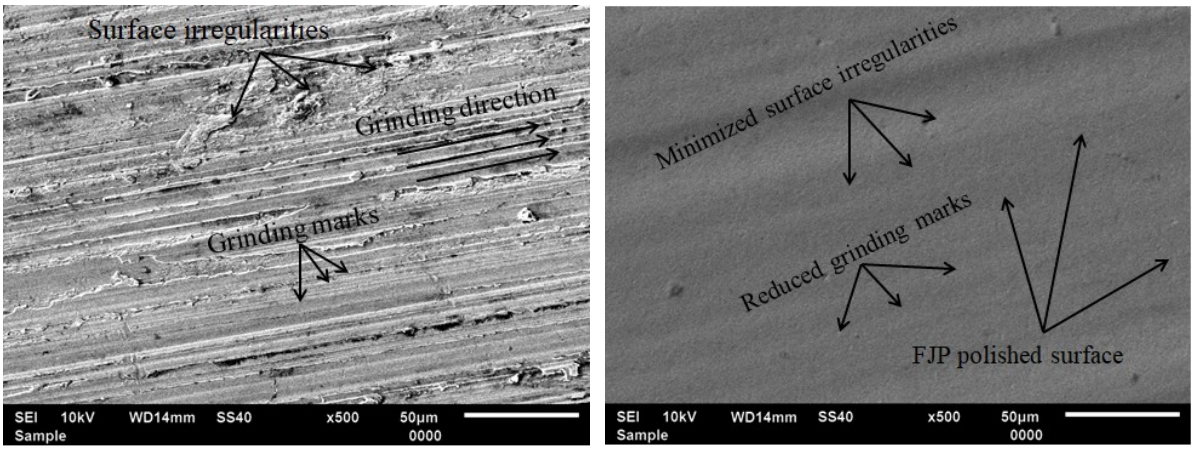

(a) **(b)**

Figure 6.7 Scanning electron microscopy (SEM) images of (a) initial surface and (b) final FJP finished surface with optimized parameters in 12 number of passes.

These defects are the results of the grinding process which inevitably leaves scratch marks on the substrate surface. However, after applying FJP process with the optimum process parameters, the grinding marks and major surface irregularities have been minimized and a smoother surface finish has been achieved as is shown in Figure 6.7(b).

6.5 Performance of 3D printed Ti64 and SS316L nozzles

The study on rotary fluid-jet polishing of AISI H13 steel surface presented in this chapter included a set of experiments for initial FJP trials, the thirteen number of experiments as per DoE plan and the three confirmatory experiments. All these experiments were performed using an axisymmetric rotary two-nozzle 3D printed Ti64 converging nozzle having converging nozzles. A marginal wear of the Ti64 nozzles have been observed during the FJP trials and experiments. The initial weight of the 3D printed Ti64 tool (having $70mm$ length, $16mm$ diameter

and $2mm$ wall thickness) was $40.6361gm$, while the weight of the tool observed after $210min$ of experimentation was found to be $40.5840gm$. The change in weight of $0.0521gm$, indicate the marginal wear loss of 0.128% in the internal walls of body of the converging nozzles. Although, a slight variation in the form of the fluid jet was noticed compared to the first 60mintues of tool use, but the presence of the machining oil in the fluid-jet did not let the scattering of the fluid-jet for the larger stand-off distance of 32mm even during the later use of the two-nozzle Ti64 tool.

Lately, we also used a two-nozzle 3D printed nozzle made from stainless steel SS316L. The visual quality of the fluid-jets emanating from two-nozzle SS316L tool have been found to be equivalent to the Ti64 tool in our work. At the same time, the higher hardness of the SS316L compared to Ti64 has been observed to be advantageous as the SS316L tool has offered better consistency of the fluid-jets even after $300mins$ of use. Thus, relatively, the converging fluid-jet nozzles developed in the 3D printed SS316L tool has better tool-life compared to the Ti64 tool.

6.6 Closure

This chapter presented the percentage reduction in surface roughness on AISI H13 die steel workpiece surface with a rotary two-nozzle fluid-jet polishing tool and that the optimum parameters of feed rate and spindle rotation are found to be $20mm/min$ and $60rpm$ respectively. Further, the optimum process parameters of rotary two-nozzle fluid-jet polishing tool have been used to polish the AISI H13 die steel workpiece specimen for which the average surface roughness has been reduced from initial value of $390nm$ to $110nm$ in $15min$ with 12 number of passes which shows the maximum possible reduction in peaks and valleys with surface improvement of 71.79%. This shows that for FJP polishing of AISI H13 steel, the two-nozzle rotary FJP tool offers a polishing rate of $14.1666mm^2/min$ which is 1.5614 times higher than the polishing rate of $9.0725mm^2/\mathrm{min}$ achieved in case of non-rotary single-nozzle FJP tool.

Thus, as discussed in Chapter 4 about the FJP polishing of Monel-400 or the FJP polishing of AISI H13 die steel discussed in this chapter, a relative comparison shows that the fluid-jet polishing using a rotary two-nozzle tool offers a better polishing efficiency when compared to the polishing performance achieved using a single-nozzle FJP tool.

In the next chapter the conclusions drawn from the present research work on FJP polishing of Monel-400 and AISI H13 steel using custom 3D printed single-nozzle and the two-nozzle tool have been presented along with the recommendations for future scope of work in this area.

Chapter 7
Conclusions and Recommendations for Future Work

7.1 Conclusions

This chapter is mainly oriented on the mainstreams obtained through FJP process. Various process parameters that influence the quality and reliability of FJP process includes fluid pressure (P), stand-off distance (D), polishing time (T), impact angle (α), type of abrasive particles, abrasive particle shape and size, type and quantity of machining oil in abrasive slurry, slurry concentration ratio, nozzle shape, nozzle material, hardness and other mechanical properties of the substrate material. Out of the enlisted process parameters, the jet pressure, stand-off distance and the polishing time are the most critical parameters for transformation of W-shaped sectioned profile (central uncut material) to U-shaped sectional profile (uniform material removal). So, in the present research work parametric studies were conducted on ductile materials i.e., Monel 400 (NiCu alloy) and AISI H13 die steel material. The objective was to find the optimized process parameters and further improving the polishing efficiency using FJP process.

The key observation related to Monel 400 die material are as follows:

- As per the ANOVA analysis, the fluid-jet pressure was the most influencing parameter observed in the FJP study, followed by the stand-off distance and polishing time.
- The best performance of the FJP process in terms of the percentage reduction in surface roughness, $\%\,\Delta R_a$, of 70% was achieved experimentally at optimum parameters of pressure, stand-off distance and polishing time as $9.66bar$, $32.3mm$ and $170sec$, respectively.
- The accuracy of the predicted values of $\%\,\Delta R_a$ from the regression model was also proved by the confirmatory experiments, which gave the results for variation in $\%\,\Delta R_a$ within the error range/limits. It was shown that the developed regression model had a reliability of 91.53%.
- For improving polishing efficiency of the FJP process using a single nozzle polishing tool, it was found that there was 73.33% reduction in surface roughness, $\%\,\Delta R_a$, using optimized parameters with a constant feed and 10 number of multiple passes.

Similarly, parametric investigation on fluid jet polishing of AISI H13 die steel using a single nozzle tool gave the following conclusions:

- The polishing time was the most influencing parameter, followed by the stand-off distance and jet pressure. The best performance of the FJP process in terms of the percentage reduction in surface roughness, $\% \Delta R_a$, of 52% was achieved at pressure of $11.1bar$, stand-off distance of $32mm$ and polishing time of $174.6sec$.
- The accuracy of the predicted values of $\% \Delta R_a$ from the regression model was also predicted using the confirmation experiments, which yielded the results for variation in $\% \Delta R_a$ around 3.36%.
- The reduction in surface roughness values from $500nm$ to $130nm$ at a feed rate of $20mm/min$ revealed the improvement in surface polishing efficiency.
- As the feed rate increases, the surface roughness value increases but there were some intermediate ranges where surface roughness value decreased and reflected a better surface finish.
- At higher feed rate and larger stand-off distance, non-uniform material removal takes place which leads to over polishing of the material.

Further, the work was extended from single nozzle to multi-nozzle 3D printed polishing tool to evaluate the optimum process parameters and to improve the polishing efficiency on AISI H13 die steel material using combined effect of spindle rotation and feet rates. Following were the main observations of the work:

- Feed rate was the most dominant factor which contributed about 51.03% to the predicted value of the percentage change in surface roughness. The contribution of spindle rotation was about 35.26%.
- Feed rate and spindle rotation were optimized at the values of $20mm/min$ and $60rpm$ respectively, with 28.20% reduction in surface roughness.
- The reduction in surface roughness values from $390nm$ to $110nm$ in $15min$ using 12 number of passes using optimized parameters revealed 71.79% improvement in surface polishing efficiency.
- The 3D printed Ti64 nozzle performed well with a marginal wear of only 0.128% and with no noticeable variation in the surface finish.

The FJP polishing of Monel-400 or the FJP polishing of AISI H13 die steel discussed in the chapters, a relative comparison shows that the fluid-jet polishing using a rotary two-nozzle tool offers a better polishing efficiency when compared to the polishing performance achieved using a single-nozzle FJP tool.

7.2 Recommendations for future work

The present work can be extended in the following ways:

- Increasing the number of nozzles holes/orifice to 3-5 which can be manufactured using 3D printing process.
- The higher material removal rate of the targeted surface can be achieved by varying the impingement angle.
- The existing FJP experimental set up can be installed on 5-axis CNC machine to polish sculptured or curved surfaces.

References

[1] Ahn J, Shen, YF, Kim HY, Jeong H, Cho K. Development of a sensor information integrated expert system for optimizing die polishing. Robot Comp Int Manufac. 2001; 17(4): 269-276.

[2] Nagdeve L, Jain VK & Ramkumar J. Nanofinishing of freeform/sculptured surfaces: state-of-the-art. Manufacturing Review. 2018; 5: 6.

[3] Fähnle OW, van Brug H, & Frankena HJ. Fluid jet polishing of optical surfaces. Appl Opt. 1998; 37: 6771.

[4] Beaucamp AT. Micro Fluid Jet Polishing. In: Yan J. (eds) Micro and Nano Fabrication Technology. Micro/Nano Technologies. Springer, Singapore. 2018;1.

[5] Wang CJ, Cheung CF, Ho LT, et al. A novel multi-jet polishing process and tool for high-efficiency polishing. Int J Mach Tools Manuf. 2017; 115: 60–73.

[6] Beaucamp A, Katsuura T. & Kawara Z. A novel ultrasonic cavitation assisted fluid jet polishing system. CIRP Ann - Manuf Technol. 2017; 66: 301–4.

[7] Jain VK. Abrasive-based nanofinishing techniques: an overview. Machining Science and Technology. 2008; 12(3): 257-294.

[8] Zhang S, Tao X, Lu J, et al. Structure Optimization and Numerical Simulation of Nozzle for High Pressure Water Jetting. Adv Mater Sci Eng 2015; 1-8.

[9] Cao ZC & Cheung CF. Theoretical modelling and analysis of the material removal characteristics in fluid jet polishing. International journal of mechanical sciences. 2014; 89: 158-166.

[10] Wang CJ, Cheung CF, Ho LT and Loh YM. An investigation of effect of stand-off distance on the material removal characteristics and surface generation in fluid jet polishing. Nanomanufacturing and Metrology. 2020; 3:112-122.

[11] Tsai FC, Yan BH, Kuan CY, et al. A Taguchi and experimental investigation into the optimal processing conditions for the abrasive jet polishing of SKD61 mold steel. International Journal of Machine Tools and Manufacture. 2008; 48(7-8): 932-945.

[12] Cheung CF, Ho LT, Charlton P, et al. Analysis of surface generation in the ultraprecision polishing of freeform surfaces. Proc Inst Mech Eng Part B J Eng Manuf. 2010; 224: 59–73.

[13] Zhu HT, Huang CZ, Wang J, Li QL, & Che CL. Experimental study on abrasive waterjet polishing for hard–brittle materials. International journal of machine tools and manufacture. 2009; 49(7-8): 569-578.

[14] Beaucamp AT, Freeman RR, Matsumoto A, & Namba Y. Fluid jet and bonnet polishing of optical moulds for application from visible to x-ray. International Society for Optics and Photonics. 2011; 8126.

[15] Beaucamp A, & Namba Y. Super-smooth finishing of diamond turned hard X-ray molding dies by combined fluid jet and bonnet polishing. CIRP Annals-Manufacturing Technology. 2013; 62(1): 315-318.

[16] Yunata EE, Aizawa T, Tamaoki K & Kasugi M. Plasma Polishing and Finishing of CVD-Diamond Coated WC (Co) Dies for Dry Stamping. Procedia Engineering. 2017; 207: 2197-2202.

[17] Young Choi J & do Jeong H. A study on polishing of moulds using hydrophilic fixed abrasive pad. International Journal of Machine Tools and Manufacture. 2011; 44(11): 1163-1169.

[18] Anbarasu KG, Vijayaraghavan L & Arunachalam N. Effect of multi stage abrasive slurry jet polishing on surface generation in glass. J Mater Process Technol. 2019; 267: 384–92.

[19] Cheung CF, Wang C, Ho LT et al. Curvature-adaptive multi-jet polishing of freeform surfaces. CIRP Ann. 2018; 67: 357–60.
[20] Shiou FJ & Asmare A. Parameters optimization on surface roughness improvement of Zerodur optical glass using an innovative rotary abrasive fluid multi-jet polishing process. Precis Eng. 2015; 42: 93–100.
[21] Satake U, Enomoto T, Miyagawa T, Ohsumi T, Nakagawa H, & Funabashi K. Achieving stable removal rate in polishing with small tools. Precision Engineering. 2019; 55: 248-253.
[22] Nagdeve L, Jain VK & Ramkumar J. Nanofinishing of freeform/sculptured surfaces: state-of-the-art. Manufacturing Review. 2018; 5: 6.
[23] Mohammad AK, Hong J, Wang D & Guan Y. Synergistic integrated design of an electrochemical mechanical polishing end-effector for robotic polishing applications. Robotics and Computer-Integrated Manufacturing. 2019; 55: 65-75.
[24] Noh IH. Magnetic polishing of three dimensional die and mold surfaces. The International Journal of Advanced Manufacturing Technology. 2007; 33(1-2): 18-23.
[25] Singh AK, Jha S, Pandey PM. Parametric analysis of an improved ball end magnetorheological finishing process. Proceedings of the Institution of Mechanical Engineers, Part B: Journal of Engineering Manufacture. 2012; 226(9): 1550-1563.
[26] Sarkar M & Jain VK. Nanofinishing of freeform surfaces using abrasive flow finishing process. Proceedings of the Institution of Mechanical Engineers, Part B: Journal of Engineering Manufacture. 2017; 231(9): 1501-1515.
[27] Paswan SK and Singh AK. Theoretical and experimental investigations on nano-finishing of internal cylindrical surfaces with a newly developed rotational magnetorheological honing process Proceedings of the Institution of Mechanical Engineers, Part C: Journal of Mechanical Engineering Science. 2020; 234(2): 363-383.
[28] Srivastava M and Pandey PM. Experimental investigation into polishing of monocrystalline silicon wafer using double-disc chemical assisted magnetorheological finishing process. Proceedings of the Institution of Mechanical Engineers, Part C: Journal of Mechanical Engineering Science. 2021; 235(21): 5467-5486.
[29] Wu X, Kita Y & Ikoku K. New polishing technology of free form surface by GC. Journal of Materials Processing Technology. 2007; 187: 81-84.
[30] Booij SM. Fluid Jet Polishing - possibilities and limitations of a new fabrication technique., Technical University of Delft, 2003.
[31] Hui F, Peiji G & Jingci Y. Research on material removal mechanism of fluid jet polishing. Optical technique. 2004; 1002-1582.
[32] Cao ZC, Cheung CF. & Ren M. Modelling and characterization of surface generation in Fluid Jet Polishing. Precis Eng. 2016; 43: 406–17.
[33] Fang H, Guo P & Yu J. Surface roughness and material removal in fluid jet polishing. Appl Opt. 2006; 45: 4012–9.
[34] Ho LT, Cheung CF, Kong L, et al. Theoretical and experimental investigation of three-dimensional-structured surface generation using fluid jet polishing. Proc Inst Mech Eng Part B J Eng Manuf. 2015; 231: 2317–35.
[35] Liu CH, Chen CC & Huang JS. The polishing of moulds and dies using a compliance tool holder mechanism. Journal of Materials Processing Technology. 2005; 166(2): 230-236.
[36] Tricard M, Kordonski WI, Shorey AB & Evans C. Magnetorheological jet finishing of conformal, freeform and steep concave optics. CIRP annals. 2006; 55(1): 309-312.
[37] Sooraj VS & Radhakrishnan V. Fine finishing of internal surfaces using elastic abrasives. International Journal of machine tools and manufacture. 2014; 78: 30-40.

[38] Shipley H, McDonnell D, Culleton M, Coull R, Lupoi R, O'Donnell G & Trimble D. Optimisation of process parameters to address fundamental challenges during selective laser melting of Ti-6Al-4V: A review. International Journal of Machine Tools and Manufacture. 2018; 128: 1-20.
[39] Leuders S, Thöne M, Riemer A, Niendorf T, Tröster T, Richard HA & Maier HJ. On the mechanical behaviour of titanium alloy TiAl6V4 manufactured by selective laser melting: Fatigue resistance and crack growth performance. International Journal of Fatigue. 2013; 48: 300-307.
[40] Gao JB, Zhao XL, Yue JK, Qi MC & Zhang DL. Microstructure and Mechanical Properties of Ti-6Al-4V Alloy Samples Fabricated by Selective Laser Melting. In Key Engineering Materials. 2018; 770: 179-186.
[41] Ali H, Ghadbeigi H & Mumtaz K. Effect of scanning strategies on residual stress and mechanical properties of Selective Laser Melted Ti6Al4V. Materials Science and Engineering: A. 2018; 712: 175-187.
[42] Li ZZ Study on abrasive jet polishing technology. PhD thesis 2011, National University of Defense Technology, Changsha, China.
[43] Beaucamp A, Namba Y. & Freeman R. Dynamic multiphase modeling and optimization of fluid jet polishing process. CIRP Ann - Manuf Technol. 2012; 61: 315–8.
[44] Cao ZC & Cheung CF. Theoretical modelling and analysis of the material removal characteristics in fluid jet polishing. International journal of mechanical sciences. 2014; 89: 158-166.
[45] Qi H, Wen D, Lu C, Li G. Numerical and experimental study on ultrasonic vibration-assisted micro-channelling of glasses using an abrasive slurry jet. International Journal of Mechanical Sciences.2016; 110: 94-107.
[46] Wang CJ, Cheung CF, Liu MY. Numerical modeling and experimentation of three-dimensional material removal characteristics in fluid jet polishing. Int J Mech Sci. 2017; 133: 568–577.
[47] Singh M and Singh AK. Theoretical investigations into magnetorheological finishing of external cylindrical surfaces for improved performance. Proceedings of the Institution of Mechanical Engineers, Part C: Journal of Mechanical Engineering Science. 2020; 234(24): 4872-4892.
[48] Mazzoleni AP. Design of high pressure waterjet nozzles. Research reports: 1994 NASA, Alabama University, ASEE Summer Faculty Fellowship Program, 1 October, 1994.
[49] Zhang S, Tao X, Lu J, et al. Structure Optimization and Numerical Simulation of Nozzle for High Pressure Water Jetting. Adv Mater Sci Eng 2015; 1-8.
[50] Chen C, Wang Y, Ou, H, He Y, Tang X. A review on remanufacture of dies and moulds. J Clean Prod. 2014; 64: 13-23.
[51] Kazemian ME, Gandjalikhan Nassab SA & Jahanshahi Javaran E. Comparative study of Box–Behnken and central composite designs to investigate the effective parameters of ammonia–water absorption refrigerant system. Proceedings of the Institution of Mechanical Engineers, Part C: Journal of Mechanical Engineering Science. 2021; 235(16): 3095-3108
[52] Zhang Z & Kleinstreuer C. Low-Reynolds-number turbulent flows in locally constricted conduits: a comparison study. AIAA journal. 2003; 41(5): 831-840.
[53] Mansouri A , Arabnejad H , Shirazi SA , McLaury BS . A combined CFD/experimental methodology for erosion prediction. Wear. 2015; 332: 1090–7.
[54] Grant G & Tabakoff W. Erosion prediction in turbomachinery resulting from environmental solid particles. Journal of Aircraft. 1975; 12(5): 471-478.

[55] Oka YI, Okamura K & Yoshida T. Practical estimation of erosion damage caused by solid particle impact: Part 1: Effects of impact parameters on a predictive equation. Wear. 2005; 259(1-6): 95-101.
[56] Oka YI & Yoshida T. Practical estimation of erosion damage caused by solid particle impact: Part 2: Mechanical properties of materials directly associated with erosion damage. Wear. 2005; 259(1-6): 102-109.
[57] Choudhary S, Duvedi RK, & Saini JS. Response surface methodology based parametric study for AISI H13 die steel using customized designed 3D printed Ti64 multi-nozzle polishing tool. Pro I MechE, Part C: J Mechanical Engineering Science. 2022; 236(24): 11479-11492.
[58] Wang CJ, Cheung CF, Ho LT, Loh YM. Development of a fluid line-jet polishing process for rotational axisymmetric surfaces. Journal of Manufacturing Processes. 2021; 61: 15-24.
[59] Choudhary S, Duvedi RK & Saini JS. Investigation on fluid jet polishing of AISI H13 die steel using a single nozzle tool. Proceedings of the Institution of Mechanical Engineers, Part E: Journal of Process Mechanical Engineering. 2022; 09544089221145481.
[60] Sharma P, Pandey PM. Rapid manufacturing of biodegradable pure iron scaffold using amalgamation of three-dimensional printing and pressure less microwave sintering. Proceedings of the Institution of Mechanical Engineers, Part C: Journal of Mechanical Engineering Science. 2019; 233(6): 1876-1895.
[61] Singh AK, Jha S, Pandey PM. Parametric analysis of an improved ball end magnetorheological finishing process. Proceedings of the Institution of Mechanical Engineers, Part B: Journal of Engineering Manufacture. 2012; 226(9): 1550-1563.
[62] Supriya SB, Srinivas C. Machinability Studies on Stainless steel by abrasive water jet -Review, Materials Today: Proceedings. 2018; 5: 2871–2876.

Annexure: A

Chemical composition, physical and mechanical properties of (Ti6Al4V):

Table A.1: Chemical composition of Titanium Alloy (Ti6Al4V)

S. No.	Metals	Chemical Composition (%)
1.	Carbon	<0.08
2.	Iron	<0.25
3.	Nitrogen	<0.05
4.	Oxygen	<0.2
5.	Aluminium	5.5-6.76
6.	Vanadium	3.5-4.5
7.	Hydrogen (sheet)	<0.015
8.	Hydrogen (bar)	<0.0125
9.	Hydrogen (billet)	<0.01
10.	Titanium	Balance

Table A.2: Typical physical properties of Titanium Alloy (Ti6Al4V)

S. No.	Properties	Values
1.	Density	4420 kg/m^3
2.	Melting Range	1634-1664 ˚C
3.	Specific heat	560 J/kg. ˚C
4.	Volume electrical resistivity	1.70 ohm.m
5.	Thermal conductivity	7.2 W/m.K

Table A.3: Typical mechanical properties of Titanium Alloy (Ti6Al4V)

S. No.	Properties	Minimum Values	Typical Value
1.	Tensile strength (MPa)	897	1000
2.	0.2% proof stress (MPa)	828	910
3.	Elongation over 2 inches %	10	18
4.	Elastic Modulus (GPa)	-	114
5.	Hardness Rockwell (C scale)	-	36

Annexure: B

Chemical composition, physical and mechanical properties of SS316L:

Table B.1: Chemical composition of SS316L

S. No.	Metals	Requirement as per specification (%)	Chemical Composition (%)
1.	Carbon	0.030 Max	0.017
2.	Sulphur	0.010 Max	0.008
3.	Copper	0.50 Max	0.031
4.	Manganese	2.0 Max	1.46
5.	Phosphorus	0.025 Max	0.010
6.	Chromium	17-19	17.94
7.	Molybdenum	2.25-3.0	2.81
8.	Nickel	13-15	14.41
9.	silicon	0.75 Max	0.350
10.	Iron	Balance	Balance

Table B.2: Physical properties of SS316L

S. No.	Properties	Values
1.	Density	7.98 g/cm^3
2.	Porosity	<0.01%
3.	Maximum pore size	35 µm

Table B.3: Mechanical properties of SS316L

Properties	Metric
Tensile strength	580 MPa
Yield strength	495MPa
Percentage elongation after fracture	41% (vertical) 32% (horizontal)

Annexure: C

Chemical composition, physical and mechanical properties of NiCu alloy (Monel-400) and H13 steel:

Table C.1: Chemical composition of NiCu alloy (MONEL-400)

S. No.	Metals	Chemical Composition (%)	Reference Composition (%)
1.	Carbon	0.055	0.300
2.	Sulphur	0.011	0.024
3.	Copper	30.546	28 – 34
4.	Manganese	1.015	2
5.	Chromium	0.291	-
6.	Molybdenum	0.018	-
7.	Iron	2.326	2.5
8.	Titanium	0.033	-
9.	Aluminium	0.298	-
10.	Nickel	65.309	63 minimum
11.	silicon	0.078	0.5

Table C.2: Physical properties of NiCu alloy (MONEL-400)

S. No.	Properties	Values
1.	Density	8800 kg/m^3
2.	Melting Range	1300 – 1350 ˚C
3.	Poisson Ratio	0.32
4.	Curie Temperature	21 – 49 ˚C
5.	**Modulus of Elasticity (GPa)** (a) Tension (b) Compression (c) Torsion	 179 179 65.5

Table C.3: Mechanical properties of NiCu alloy (MONEL-400)

S. No.	Form and Condition	Tensile Strength (MPa)	Yield Strength at 0.2 % offset (MPa)	Elongation (%age)	Hardness	
	Plate				Brinell (3000Kg – 10mm ball)	Rockwell (B scale)
1.	Hot-Rolled, As Rolled	517-655	276-517	45-30	125-215	70-96
2.	Hot-Rolled, Annealed	482-586	193-345	50-35	110-140	60-76

Table C.4: Nomenclature and chemical composition of H13 tool steel material in different standards

Composition	C		Mn		P	S	Si		Cr		V		Mo	
H13 (**ASTM A681**	0.32	0.45	0.2	0.6	0.03	0.03	0.8	1.25	4.75	5.5	0.8	1.2	1.1	1.75
1.2344 /X40CrMoV5-1 (**DIN ISO 4957)**	0.35	0.42	0.25	0.5	0.03	0.02	0.8	1.2	4.8	5.5	0.85	1.15	1.1	1.5
SKD61 (**JIS G4404)**	0.35	0.42	0.25	0.5	0.03	0.02	0.8	1.2	4.8	5.5	0.8	1.15	1.0	1.5

Table C.5: Mechanical properties of H13 Tool Steel

Properties	Metric
Ultimate tensile strength, (at 20°C, varies with heat treatment) (MPa)	1200 – 1590
Yield tensile strength, (at 20°C, varies with heat treatment) (MPa)	1000 – 1380
Reduction of area (at 20°C)	50.00%
Modulus of elasticity (at 20°C)	215 GPa
Poisson's ratio	0.27-0.30

Table C.6: Application of H13 tool steel as tool material for extrusion dies

Part	Aluminium-magnesium alloys (HRC)	Copper alloys (HRC)	Stainless steel (HRC)
Dies, Backers, Die-holders, Liners, Dummy blocks, Stems	44-50	43-47	45-50
	41-50	40-48	40-48
Austenitizing temperature	1020-1030°C	1040-1050°C	

Table C.7: Application of H13 tool steel for plastic moulding dies

Part	Austenitizing Temperature	HRC
Injection moulds Compression/ transfer moulds	1020-1030°C	50-52
	Tempering 250°C	

List of Publications

Publications from present work in peer reviewed (SCI) journals

1. **Shubham Choudhary**, R. K. Duvedi, and J. S. Saini. "Effect of process parameters on surface roughness of NiCu alloy in fluid jet polishing." *Proceedings of the Institution of Mechanical Engineers, Part E: Journal of Process Mechanical Engineering* (2023). **IF- 1.822** & **DOI:** 10.1177/09544089231166651
2. **Shubham Choudhary**, R. K. Duvedi, and J. S. Saini**.** "Investigation on fluid jet polishing of AISI H13 die steel using a single nozzle tool. " *Proceedings of the Institution of Mechanical Engineers, Part E: Journal of Process Mechanical Engineering* (2022*), pp.0954408922114548*. **IF- 1.822** & **DOI:** 10.1177/09544089221145481
3. **Shubham Choudhary**, R. K. Duvedi, and J. S. Saini**.** "Response surface methodology based parametric study for AISI H13 die steel using customized designed 3D printed Ti64 multi-nozzle polishing tool." *Proceedings of the Institution of Mechanical Engineers, Part C: Journal of Mechanical Engineering Science* (2022)*, 236(24), pp.11479-11492*. **IF- 1.758** & **DOI:** 10.1177/09544062221115291

Published in International conference

1. **Shubham Choudhary**, R. K. Duvedi, and J. S. Saini. "Effect of material removal characteristics with varying incident angle in fluid jet polishing process." *Materials Today: Proceedings* (2022), *62*, 215-219.